

Aus dem Institut für Molekular- und Zellbiologie der TH Mannheim

Leiter: Prof. Dr. rer. nat. Mathias Hafner

On the influence of the physicochemical properties of novel multimodal  
ligands on protein chromatography.

Inauguraldissertation

zur Erlangung des Doctor scientiarum humanarum (Dr. sc. hum.)

der

Medizinischen Fakultät Mannheim

der Ruprecht-Karls-Universität

zu

Heidelberg

vorgelegt von

Jan Anselm Hedrich

aus

Heilbronn

2025

Dekan: Prof. Dr. med. Sergij Goerd  
Referent(in): Prof. Dr. rer. nat. Mathias Hafner

# TABLE OF CONTENT

LIST OF ABBREVIATIONS.....	1
LIST OF SYMBOLS .....	3
1 INTRODUCTION .....	6
1.1 Biopharmaceuticals.....	6
1.1.1 Definition, Significance, and Therapeutic Impact .....	6
1.1.2 Classes of Biopharmaceuticals .....	7
1.1.3 Manufacturing Challenges and Product Heterogeneity.....	8
1.1.4 Toward Advanced Separation Strategies.....	9
1.2 Chromatography .....	9
1.2.1 General introduction .....	9
1.2.2 Common types of liquid chromatography materials .....	10
1.2.2.1 Resin-based Chromatography.....	10
1.2.2.2 Membrane Chromatography.....	11
1.2.2.3 Monolith Chromatography .....	12
1.2.3 Analytical vs. Preparative Chromatography .....	12
1.2.3.1 Analytical Chromatography.....	12
1.2.3.2 Preparative Chromatography.....	13
1.2.4 Chromatographic modalities.....	14
1.2.4.1 Affinity Chromatography .....	14
1.2.4.2 Ion exchange chromatography .....	15
1.2.4.3 Hydrophobic interaction chromatography .....	15

1.2.4.4	Size exclusion chromatography.....	16
1.2.4.5	Mixed-mode chromatography.....	16
1.3	Chromatographic modelling.....	17
1.3.1	Modelling Software.....	18
1.3.1.1	MATLAB.....	18
1.3.1.2	CADET (Chromatography Analysis and Design Toolkit).....	19
1.3.1.3	Berkeley Madonna.....	19
1.4	Theoretical considerations.....	20
1.4.1	Transport Phenomena.....	20
1.4.2	Adsorption Isotherms.....	22
1.4.3	The SMA Model.....	24
1.4.3.1	Ion Exchange Isotherm.....	24
1.4.3.2	Mixed-Mode Isotherm.....	25
1.4.3.3	Asymmetry Coefficients.....	26
1.4.4	Linear gradient elution experiments.....	27
1.5	Aim of the work.....	29
<b>2</b>	<b>MATERIALS AND METHODS.....</b>	<b>30</b>
2.1	Materials.....	30
2.1.1	Chemicals.....	30
2.1.2	Devices and Hardware.....	31
2.1.3	Software.....	32
2.1.4	Protein.....	32
2.1.5	Chromatographic material.....	33
2.1.5.1	Columns.....	33

2.1.5.2	Membranes.....	34
2.2	Methods .....	36
2.2.1	Preparations.....	36
2.2.1.1	Purification of mAb02 using protein A chromatography.....	36
2.2.1.2	CEX analysis .....	36
2.2.1.3	SEC analysis .....	36
2.2.1.4	Preparative isolation of charge variants.....	37
2.2.2	Modelling of liquid chromatography.....	37
2.2.2.1	Chromatographic Systems .....	37
2.2.2.2	Linear salt and pH gradient calculation.....	37
2.2.2.3	Column chromatography (Eshmuno® CMX) .....	39
2.2.2.4	Membrane Chromatography (Natrix® CH) .....	40
2.2.2.5	Determination of model parameters .....	41
2.2.2.6	Simulation and prediction of elution profiles .....	43
3	RESULTS .....	44
3.1	Modelling and simulation of mAb charge variant separation on mixed-mode resin Eshmuno CMX®.....	44
3.1.1	Linear gradient elution experiments .....	44
3.1.1.1	Comparison of mixed-mode to traditional ion exchanger .....	44
3.1.1.2	Additional separation on Eshmuno CMX® at medium high salt concentration .....	45
3.1.1.3	U-shaped retention behaviour .....	46
3.1.2	Mechanistic modelling of Eshmuno® CMX elution.....	48
3.1.2.1	Mechanistic modelling using a stoichiometric displacement (SD) model	48

3.1.2.2	Mechanistic modelling using a mixed-mode model including different activity coefficients.....	50
3.1.3	Understanding differences in activity coefficients.....	55
3.1.3.1	Simple activity coefficient.....	55
3.1.3.2	pH and salt dependent activity coefficient .....	56
3.1.3.3	Complex activity coefficient .....	58
3.1.4	Validation and simulation .....	59
3.1.4.1	Prediction of pH gradient experiment from calibration data.....	59
3.1.4.2	Prediction of reverse gradient elution .....	60
3.1.4.3	Prediction of dual anti-parallel pH and salt gradient .....	61
3.2	Modelling, simulation and scale up of Natrix® CH mixed-mode membrane adsorber .....	62
3.2.1	Comparison of ion exchange membrane with mixed-mode Natrix® CH 62	
3.2.2	Modelling of charge variant separation on Natrix® CH.....	65
3.2.3	Validation of model calibration by optimization of separation.....	68
3.2.4	Scale up of mAb charge variant separation .....	69
3.2.4.1	Binding capacity.....	69
3.2.4.2	Estimation of shielding factors .....	70
3.2.4.3	Scale up of charge variant separation using mechanistic modelling 74	
4	DISCUSSION .....	78
4.1	Modelling and simulation of mAb charge variant separation on mixed-mode resin Eshmuno CMX®.....	78
4.1.1	Comparison of mixed-mode to traditional ion exchanger.....	78

4.1.2	Additional separation on Eshmuno® CMX at medium high salt concentration.....	78
4.1.3	U-shaped retention behaviour.....	79
4.1.4	Mechanistic modelling of Eshmuno® CMX elution.....	80
4.1.4.1	Mechanistic modelling using a standard stoichiometric displacement model	80
4.1.4.2	Mechanistic modelling using a mixed-mode model including different activity coefficients.....	81
4.1.4.3	Calculated activity coefficients in detail .....	88
4.1.5	Model validation .....	91
4.1.6	Model validation with reverse salt gradient elution.....	92
4.1.7	Validation using dual gradient elution.....	93
4.1.8	Concluding the modelling and simulation of charge variant separation on Eshmuno® CMX.....	95
4.2	Modelling, simulation and scale up of Natrix® CH mixed-mode membrane adsorber .....	95
4.2.1	Comparison of ion exchange membrane with mixed-mode Natrix® CH	95
4.2.2	Modelling with SD model.....	97
4.2.3	Charge profile.....	98
4.2.4	Model validation .....	99
4.2.5	DBC measurements .....	100
4.2.6	High load experiments.....	102
4.2.7	Shielding fits .....	102
4.2.8	Simulation validation .....	103
4.2.9	Scale up .....	104
4.3	Conclusion .....	106

5 SUMMARY .....	108
6 REFERENCES .....	110
7 CURRICULUM VITAE.....	131
8 ACKNOLEGEMENT.....	134

## LIST OF ABBREVIATIONS

AU	Absorbance Unit
BSA	Bovine Serum Albumin
CADET	Chromatography Analysis and Design Toolkit
CEX	Cation Exchange Chromatography
CIP	Cleaning-In-Place
CMX	Mixed-mode cation exchange resin (Eshmuno® CMX, Merck KGaA)
CPX	Strong cation exchange resin (Eshmuno® CPX, Merck KGaA)
CV	Column Volume
DBC	Dynamic Binding Capacity
DBC <sub>10 %</sub>	Dynamic Binding Capacity at 10% Breakthrough
DBC <sub>95 %</sub>	Dynamic Binding Capacity at 95% Breakthrough
DNA	Deoxyribonucleic acid
EMG	Exponentially modified gaussian
FDA	Food and Drug Administration
HCP	Host cell protein
HIC	Hydrophobic Interaction Chromatography
HPLC	High-Performance Liquid Chromatography
IEX	Ion Exchange Chromatography
LC	Liquid Chromatography
LGE	Linear gradient elution
mAb	Monoclonal Antibody
MMC	Mixed-mode chromatography
mRNA	messenger ribonucleic acid
MV	Membrane Volume

## List of abbreviations

---

NaCl	Sodium chloride
NaOH	Sodium Hydroxide
Na <sub>2</sub> SO <sub>4</sub>	Sodium Sulphate
ODE	Ordinary differential equation
PBS	Phosphate-Buffered Saline
PDE	Partial differential equation
pI	Isoelectric Point
pKa	Acid dissociation constant
pH	Potentia Hydrogenii
QbD	Quality by Design
RNA	Ribonucleic acid
SDM	Stoichiometric displacement model
SMA	Steric mass action
SEC	Size Exclusion Chromatography
SMA	Steric Mass Action
UV	Ultraviolet

## LIST OF SYMBOLS

Latin Letters

$A_i$	Distribution coefficient of component $i$
$D_{ax}$	Axial dispersion coefficient
$F$	Faraday constant
$GH_M$	Normalized gradient slope
$GH_{pH}$	Normalized pH gradient slope
$GH_{salt}$	Normalized salt gradient slope
$i$	Subscript index denoting protein species $i$
$K_{eq,i}$	Thermodynamic equilibrium constant for protein $i$
$K_s$	Interaction parameter describing the salt-induced interaction
$L$	Functional group on stationary phase
$N_{+i}$	Number of basic amino acids
$N_{-i}$	Number of acidic amino acids
$N_A$	Avogadro's number
$P_i^{z_i}$	Charged protein species $i$ with charge $z_i$
$R$	Universal gas constant
$S^{z_s}$	Salt counterion with charge $z_s$
$T$	Absolute temperature
$V_C$	Column volume
$V_g$	Gradient volume
$a_i$	Activity of a component $i$ in solution
$\hat{a}_i$	Activity of an adsorbed component $i$
$a_s$	Activity the counterion in solution
$\hat{a}_s$	Activity of the adsorbed counterion
$a_w$	Activity of water
$c$	molar concentration of pure water
$c_i$	Concentration of component $i$ in the mobile phase
$c_s$	Concentration of the counterion in the mobile phase
$c_{M,init}$	Initial modifier concentration
$c_{M_i,elu}$	Elution modifier concentration of component $i$

$c_W$	Molar concentration of hydrated hydrophobic ligands
$d_p$	Particle diameter of the resin particles
$g_{pH}$	pH gradient slope
$g_{salt}$	Salt gradient slope
$k_{d,i}$	Pore exclusion factor of component i
$k_{eff,i}$	Effective mass transfer coefficient of component i
$n$	Number of hydrophobic interactions
$q_{eq,i}^*$	Equilibrium concentration of adsorbed component i
$q_{max,IEC,i}$	Max protein capacity on ionic binding sites
$q_{max,MMC,i}$	Max protein capacity on hydrophobic binding sites
$q_i$	Adsorbed concentration of protein i
$q_i^*$	Averaged concentration of adsorbed component i
$\bar{q}_s$	Concentration of bound counterions
$v$	Interstitial velocity of the mobile phase
$x_i$	Mole fraction of component i in solution
$\hat{x}_i$	Mole fraction of adsorbed component i
$x_s$	Mole fraction of counterion in solution
$\hat{x}_s$	Mole fraction of adsorbed counterion
$z_i$	Net charge of the protein
$z_s$	Charge of the salt ion

### Greek Letters

$\alpha$	Pre-exponential coefficient in pH dependent activity coefficient
$\beta$	Exponential factor in pH dependent activity coefficient
$\delta$	Steric hindrance factor of hydrophobic interaction
$\varepsilon$	Interstitial porosity
$\varepsilon_D$	Permittivity of the solvent
$\varepsilon_p$	Particle porosity
$\gamma_i$	Activity coefficient of component i in solution
$\hat{\gamma}_i$	Activity coefficient of adsorbed component i
$\gamma_s$	Activity coefficient of counterion in solution
$\hat{\gamma}_s$	Activity coefficient of adsorbed counterion
$\tilde{\gamma}_{Protein}$	Modified activity coefficient of protein

$\kappa$	Inverse Debye length
$\mu$	Chemical potential
$\eta_P$	Viscosity-related parameter in Kirkwood model
$\theta_P$	Hydrodynamic radius parameter
$\phi$	Volume fraction parameter in Kirkwood model
$\xi$	Number of displaced solvent molecules
$\Lambda$	Ionic capacity of the stationary phase
$\Lambda_{HIC}$	Hydrophobic ligand density
$\Lambda_{IEC}$	Ionic ligand density
$\nu_i$	Characteristic charge of protein i

# 1 INTRODUCTION

## 1.1 Biopharmaceuticals

### 1.1.1 Definition, Significance, and Therapeutic Impact

Biopharmaceuticals, also referred to as biologics, are a class of therapeutic agents derived from living systems through advanced biotechnological methods.<sup>1, 2</sup> These macromolecules, ranging from monoclonal antibodies (mAbs) and recombinant proteins to nucleic acid-based treatments, are structurally complex and inherently heterogeneous, in contrast to chemically synthesized small-molecule drugs, which are relatively simple and uniform.<sup>1, 2</sup>

The development of biopharmaceuticals has been driven by breakthroughs in recombinant DNA technology, mammalian cell expression systems, and protein purification strategies.<sup>3-6</sup> These innovations have enabled the precise targeting of disease mechanisms at the molecular level, often yielding superior efficacy and safety profiles.<sup>3-6</sup> Biopharmaceuticals are now central to the treatment of a wide range of diseases, including cancer, autoimmune disorders, genetic conditions, and infectious diseases.<sup>3-6</sup>

The following are only some of many successful biopharmaceuticals showing their clinical relevance:

- Recombinant human insulin revolutionizing diabetes management.<sup>7, 8</sup>
- Tissue plasminogen activator (tPA) becoming beneficial in acute stroke intervention.<sup>9</sup>
- Monoclonal antibodies like rituximab (anti-CD20) for lymphoma<sup>10</sup>, trastuzumab (anti-HER2) and successors for breast cancer<sup>11</sup>, and adalimumab (anti-TNF) for rheumatoid arthritis<sup>12</sup> changing outcomes in their respective indications.

These biopharmaceuticals not only deliver high clinical value through targeted modulation of biological pathways but also represent significant economic assets. Biologics dominate pharmaceutical pipelines and account for many of the top revenue-

generating drugs globally. Their design and engineering continue to evolve, incorporating bispecific formats, antibody-drug conjugates, and mRNA-based therapeutics, further expanding their role in precision and personalized medicine<sup>3, 13, 14</sup>.

### 1.1.2 Classes of Biopharmaceuticals

Biopharmaceuticals encompass a broad range of therapeutic modalities, each with distinct molecular features and clinical roles:

Monoclonal antibodies (mAbs) are the most widely used biologics in clinical practice.<sup>15-17</sup> These proteins are designed to bind specific antigens with high affinity, enabling applications in oncology, immunology, and infectious diseases.<sup>15-17</sup> Their formats have evolved from chimeric to fully human, improving tolerability and reducing immunogenicity.<sup>15-17</sup>

Recombinant hormones such as insulin analogues, erythropoietin (EPO), and human growth hormone (hGH) are used in endocrine and hematologic disorders.<sup>18-20</sup> Modern manufacturing processes ensure high purity and consistent potency, replacing older animal-derived products.<sup>18-20</sup>

Cytokines and growth factors, including interferons, interleukins, and colony-stimulating factors (e.g., G-CSF), modulate immune responses or support hematopoiesis.<sup>21</sup> They are commonly used in oncology, viral infections, and autoimmune diseases.<sup>21</sup>

Enzyme replacement therapies (ERTs) are used to treat lysosomal storage disorders such as Gaucher and Pompe disease.<sup>22-24</sup> Recombinant enzymes, engineered to reach affected tissues, address the underlying enzyme deficiencies and significantly improve patient outcomes.<sup>22-24</sup>

Vaccines have evolved through recombinant protein and nucleic acid technologies.<sup>25, 26</sup> Recent successes of mRNA vaccines (e.g., BNT162b2, mRNA-1273) highlight their rapid scalability and clinical impact, particularly in infectious disease control.<sup>25, 26</sup>

Antibody-drug conjugates (ADCs) couple mAbs with cytotoxic agents, allowing targeted chemotherapy.<sup>27</sup> Brentuximab vedotin and trastuzumab emtansine are successful examples in lymphoma and breast cancer.<sup>27</sup>

Each class presents unique development, manufacturing, and regulatory challenges, reinforcing the need for tailored purification and quality control strategies, especially as therapies become more structurally complex and personalized.<sup>28, 29</sup>

### 1.1.3 Manufacturing Challenges and Product Heterogeneity

Given their complex structure, extensive post-translational modifications, and sensitivity to manufacturing conditions, biopharmaceuticals, particularly monoclonal antibodies (mAbs), require tightly controlled production processes and sophisticated analytical and purification strategies.<sup>30-32</sup> These demands are becoming even more pronounced with the emergence of next-generation biologics, reinforcing the need for innovative approaches to maintain product quality, consistency.<sup>33-35</sup> Among the various biologic modalities, mAbs stand out not only for their therapeutic relevance but also for their structural intricacy.<sup>36</sup> Produced in mammalian expression systems, mAbs inherently exist as heterogeneous populations due to variable post-translational modifications, resulting in multiple isoforms, collectively referred to as charge variants or structural variants.<sup>37</sup> These include alterations such as glycosylation differences, C-terminal lysine truncation, deamidation, oxidation, N-terminal processing, and aggregation, all of which can impact the molecule's stability, efficacy, and immunogenicity.<sup>38, 39</sup>

These modifications can arise during cell culture, purification, or storage, and they significantly influence the antibody's stability, binding affinity, immunogenicity, and pharmacokinetics.<sup>40</sup> Regulatory agencies require robust characterization and control of such heterogeneities, as even minor variant shifts can affect product quality and therapeutic performance.<sup>40, 41</sup>

Downstream processing, therefore, plays a pivotal role in ensuring consistent product profiles. Chromatographic separation techniques, particularly ion exchange chromatography, have traditionally been used to resolve charge variants.<sup>42, 43</sup> However, as product complexity increases and regulatory demands tighten, classical approaches often fall short in achieving the required resolution, yield, or throughput.<sup>44</sup>

### 1.1.4 Toward Advanced Separation Strategies

The growing need to resolve subtle molecular variants has spurred the development of new chromatographic materials with enhanced selectivity.<sup>29, 45-49</sup> Mixed-mode chromatography media, which integrate multiple interaction modalities (e.g., ionic and hydrophobic), offer promising advantages in resolving closely related isoforms.<sup>29, 45-49</sup> These materials can improve separation performance and robustness, especially under challenging feed conditions or for difficult-to-resolve species.<sup>29, 45-49</sup>

These new technologies are being paired with mechanistic models to optimize processes.<sup>50-52</sup> Mechanistic modelling, for example, has been used to predict the behaviour of multimodal cation exchange systems, allowing precise control of charge variant separation.<sup>50-52</sup>

## 1.2 Chromatography

### 1.2.1 General introduction

The origins of chromatography trace back to the 20th century, but the technique has evolved significantly, particularly in the context of protein purification and downstream bioprocessing.<sup>29</sup> Today, chromatography is not only a tool for achieving high purity but also a regulatory expectation for ensuring the critical quality and performance attributes of biopharmaceuticals, including identity, potency, purity, and safety.<sup>53, 54</sup>

Chromatography or liquid chromatography is a fundamental separation technique widely used in both analytical and preparative biopharmaceutical applications.<sup>55</sup> It operates on the principle of differential distribution of molecules between a stationary phase and a mobile phase, allowing the resolution of complex mixtures into individual components.<sup>56, 57</sup> Its adaptability, scalability, and resolution power make chromatography indispensable in the purification, characterization, and quality control of biologics such as monoclonal antibodies, vaccines, and recombinant proteins.<sup>58, 59</sup>

Key components of a liquid chromatographic system are: <sup>60, 61</sup>

- Stationary phase: The medium (e.g., resin, membrane, monolith) through which the mobile phase passes.

- Mobile phase: A liquid buffer that carries the analyte through the stationary phase.
- Analyte: The substance of interest, such as a monoclonal antibody or charge variant, being separated from other components.

The interaction between the analyte and the stationary phase determines the retention time and resolution.<sup>61</sup> Factors like ionic strength<sup>62</sup>, pH<sup>50</sup>, and temperature<sup>63</sup> are manipulated to control separation.

Stationary phases can be very different, and a wide variety is used in combination with or without a functionalized ligand for a desired mode of application. These modes of chromatographic separation include: <sup>64</sup>

- Adsorption: Based on interaction with the stationary phase
- Molecular exclusion: Based on molecular size and weight
- Partitioning: Based on different solubility between mobile and stationary phase

Stationary phases can be of many materials and shapes. Common materials are resin beads, membrane sheets, and monolithic columns, each with distinct structural characteristics and operational profiles that make them suitable for different solutes or stages of bioprocessing.<sup>49, 64</sup>

## 1.2.2 Common types of liquid chromatography materials

### 1.2.2.1 Resin-based Chromatography

Resin-based chromatography is the most established technique in preparative bioprocessing, employed across capture, intermediate, and polishing steps. It utilizes porous polymer beads, commonly agarose, polymethacrylate, or polystyrene-divinylbenzene, as the stationary phase, functionalized with ion exchange, hydrophobic, or mixed-mode ligands.<sup>61, 65</sup> The beads' internal porosity provides high surface area for binding, but mass transport is primarily diffusion-limited, particularly for large biomolecules.<sup>60, 66</sup>

A key advantage is the high dynamic binding capacity (DBC) under low-to-moderate flow conditions, enabling efficient use of column volume.<sup>65</sup> Resins also offer excellent

scalability, maintaining linear pressure-flow relationships across column sizes and formats.<sup>61</sup> Additionally, a broad range of ligand chemistries supports selective removal of impurities, aggregates, and charge variants.<sup>51, 60</sup>

However, slow intraparticle diffusion can limit throughput, especially at high flow rates or under continuous processing demands.<sup>65, 66</sup> Alternative formats like membrane adsorbers or monoliths mitigate these limitations by relying on convective transport but often sacrifice binding capacity.<sup>67-69</sup>

### 1.2.2.2 Membrane Chromatography

Membrane chromatography has emerged as a complementary and increasingly popular alternative to traditional resin-based systems, especially in flow-through polishing steps and high-throughput applications.<sup>70, 71</sup> Unlike porous resins that rely on diffusive mass transport, membrane adsorbers utilize convective flow through functionalized pores to facilitate rapid solute-ligand interactions.<sup>71</sup> This design results in significantly reduced residence times and higher process throughput, particularly for large biomolecules such as monoclonal antibodies and viruses.<sup>61, 70</sup>

Membrane devices are typically based on modified cellulose or synthetic polymers and functionalized with ion exchange or multimodal ligands<sup>67, 72</sup> One of the main advantages of membrane chromatography is its high throughput and short cycle time, making it especially useful in downstream processing where speed and buffer consumption are critical factors. Membranes are also well suited for single-use applications, reducing validation requirements and the risk of cross-contamination.<sup>68, 73</sup> Moreover, their open pore structures are advantageous for purifying large biological entities such as viruses, plasmids, and aggregates that would otherwise suffer from slow diffusion in resins.<sup>70, 74</sup>

However, membrane adsorbers typically exhibit lower dynamic binding capacities (DBC) compared to traditional packed-bed columns, particularly under high-load conditions. This trade-off is especially relevant for capture steps where resin-based systems still dominate.<sup>69</sup>

Despite these limitations, the use of membrane chromatography is expanding rapidly, particularly in polishing steps where trace impurities such as DNA, endotoxins, or host cell proteins must be removed efficiently.<sup>75</sup> Current developments include engineered ligand chemistries, electrospun nanofiber matrices, and laterally fed devices that

enhance binding uniformity and scalability.<sup>72, 76, 77</sup> These innovations position membrane adsorbers as a key enabling technology in intensified, continuous, and single-use biomanufacturing.

### 1.2.2.3 Monolith Chromatography

Monolith chromatography employs continuous, porous stationary phases that differ fundamentally from traditional packed-bed resins.<sup>78, 79</sup> Rather than being composed of discrete particles, monoliths are synthesized as single, rigid blocks, typically from methacrylate or silica precursors, with highly interconnected macropores.<sup>78-80</sup> This structure permits convective flow through the matrix, minimizing mass transfer resistance and enabling high-throughput processing of large biomolecules such as plasmids, viruses, and virus-like particles.<sup>78, 81</sup>

The macroporous network is central to the performance of monoliths.<sup>78</sup> It provides exceptionally low pressure drops and allows analytes to reach binding sites directly without relying on slow intraparticle diffusion.<sup>78, 81</sup> This makes monoliths especially effective for fast separations and applications involving large entities that are often excluded from conventional resin pores.<sup>78</sup> Ligands such as ion exchangers or affinity tags can be introduced via surface functionalization, making monoliths adaptable to various chromatographic modes including IEX, HIC, and affinity.<sup>80</sup>

Compared to resin or membrane adsorbers, monoliths offer higher permeability and faster mass transfer, enabling rapid separations at low backpressure.<sup>80, 81</sup> They eliminate particle packing and frits.<sup>80, 81</sup> However, organic monoliths may swell with solvent changes, and silica-based types are pH-sensitive.<sup>80</sup> Binding capacity remains lower than that of resins or membranes, and their scalability is limited.<sup>60, 80, 81</sup>

### 1.2.3 Analytical vs. Preparative Chromatography

Chromatography in bioprocessing is broadly categorized into preparative and analytical chromatography, distinguished by their scale, purpose, and methodological requirements.<sup>82</sup>

#### 1.2.3.1 Analytical Chromatography

Analytical chromatography serves as a cornerstone of biopharmaceutical characterization, offering high-resolution, high-precision insights into the structural

integrity, purity, and variability of complex biologics.<sup>65, 83</sup> In contrast to preparative chromatography, which focuses on the large-scale isolation and purification of product streams, analytical chromatography is designed for detailed quantitative and qualitative assessment, typically in the milligrams to picograms range.<sup>64</sup> It is routinely employed in combination with high-performance liquid chromatography (HPLC) or ultra-high-performance liquid chromatography (UHPLC) systems, both of which operate at elevated pressures to facilitate rapid and efficient separation.<sup>64</sup>

These systems are engineered to provide exceptional resolution and sensitivity, enabling the detection of subtle structural differences, degradation products, or post-translational modifications.<sup>64</sup> Analytical chromatographic methods are typically integrated with advanced detection technologies, such as ultraviolet (UV) absorbance, fluorescence, or mass spectrometry (MS), to deliver both qualitative and quantitative data with high reproducibility.<sup>61, 64</sup>

Techniques such as ion exchange chromatography (IEX), size-exclusion chromatography (SEC), and reversed-phase chromatography (RP-HPLC) are central to analytical workflows, each exploiting different physicochemical properties of the analyte, such as charge, hydrodynamic radius, or hydrophobicity.<sup>64</sup>

### 1.2.3.2 Preparative Chromatography

Following the precise analytical characterization of biologics, preparative chromatography plays a central role in the manufacturing and purification of therapeutic proteins at laboratory and pilot scales.<sup>64</sup> While analytical chromatography is concerned with detailed molecular profiling, preparative chromatography is designed for bulk separation and recovery of target biomolecules from complex mixtures containing host cell proteins, DNA, aggregates, and other impurities.<sup>84, 85</sup>

Preparative chromatography is performed using systems and columns engineered for high throughput and scalability, capable of processing large sample volumes ranging from a few millilitres in research settings to thousands of litres in biomanufacturing environments.<sup>86, 87</sup> Its goal is to boost product yield and purity with high recovery rates by utilizing the target protein's molecular properties, like charge, hydrophobicity, and size, to selectively bind, retain, and elute it from the chromatographic medium.<sup>56, 60, 64</sup>

Operationally, preparative chromatography is structured into three key phases: loading, washing, and elution.<sup>88, 89</sup> During the loading phase, the feedstock is applied

under conditions that favour binding of the target molecule to the stationary phase.<sup>90</sup> Washing removes unbound contaminants, and elution is performed under altered conditions, such as increased salt concentration or pH change, to release the bound protein. Optimization of these steps is critical to achieving consistent performance and regulatory compliance.<sup>90</sup>

As biologics grow in molecular complexity and regulatory standards become more stringent, preparative chromatography remains a central unit operation in downstream processing.<sup>91, 92</sup> It bridges the gap between fermentation or cell culture harvest and the final drug substance, ensuring that biopharmaceuticals meet quality, safety, and efficacy expectations.<sup>92</sup>

#### 1.2.4 Chromatographic modalities

Key separation techniques in preparative chromatography include several well-established modalities that are directly associated with the stationary phase materials previously introduced, such as resins, membrane adsorbers, and monoliths, each of which can be functionalized with specific chemistries to perform affinity, ion exchange, hydrophobic interaction, size exclusion, or mixed-mode separations.<sup>65</sup>

##### 1.2.4.1 Affinity Chromatography

One of the most widely used modalities is affinity chromatography, which typically serves as the primary capture step, especially in monoclonal antibody production.<sup>93</sup> This technique often employs Protein A ligands immobilized on resin beads, which selectively bind the Fc region of immunoglobulin G (IgG).<sup>94</sup> The resulting capture is highly efficient and selective, capable of producing purities exceeding 90% directly from clarified cell culture.<sup>95</sup> While the elution can be carried out by adding a mimicking agent, elution in affinity chromatography is typically performed under low pH.<sup>96</sup> While this is a fast and efficient method, the pH sensitive mAb might form aggregates if incubated for too long in these harsh conditions.<sup>96</sup> Low pH also leads to Protein A leaching and degradation of the column over time.<sup>96</sup> While resin formats dominate this step, membrane and monolith-based Protein A platforms are emerging for high-throughput, low-pressure alternatives.<sup>69, 80</sup>

#### 1.2.4.2 Ion exchange chromatography

Ion exchange chromatography (IEC) is a widely used separation technique in biotechnology, especially crucial for purifying monoclonal antibodies (mAbs) during downstream processing.<sup>5, 97, 98</sup> It serves as a critical polishing step after Protein A affinity capture to remove product- and process-related impurities such as host cell proteins (HCP), DNA, leached Protein A, and mAb variants, including charge and size heterogeneities.<sup>5, 97, 98</sup>

IEC operates on the principle that proteins exhibit different net charges depending on the pH of the mobile phase.<sup>99</sup> By modulating pH and ionic strength, proteins can be differentially retained and eluted based on their charge profiles.<sup>99, 100</sup> Salt gradients at constant pH are traditionally used for elution, providing effective separation for aggregates but often proving insufficient for resolving closely related charge variants due to minimal differences in their effective charges.<sup>99, 101</sup>

To enhance resolution, pH gradients<sup>6, 50, 101</sup>, created internally using buffered media or externally by mixing buffer streams, and even dual gradient<sup>98, 102</sup> approaches have been developed and applied for improved separation of charge variants in both analytical and preparative IEC systems.

#### 1.2.4.3 Hydrophobic interaction chromatography

Hydrophobic interaction chromatography (HIC) is a widely used method for protein separation that exploits the reversible association between hydrophobic patches on the protein surface and hydrophobic ligands on the stationary phase.<sup>103-105</sup> Unlike ion exchange chromatography (IEX), where protein binding decreases at high ionic strength, retention in HIC is enhanced at high salt concentrations and decreases as the salt concentration is reduced.<sup>103-105</sup> As the salt concentration is decreased, typically in a controlled gradient, the hydrophobic interactions are weakened, and proteins elute in order of decreasing hydrophobicity. HIC is thus ideally suited for intermediate purification steps, especially following high-salt procedures like ammonium sulphate precipitation or IEX, as the conditions are already compatible with the high ionic strength required for initial binding.<sup>99, 105</sup>

#### 1.2.4.4 Size exclusion chromatography

Size Exclusion Chromatography (SEC) is a separation technique that discriminates molecules based on differences in their hydrodynamic volume relative to the pore size of the stationary phase.<sup>106</sup> The stationary phase contains pores of defined size, which allow smaller molecules to penetrate more deeply into the matrix, causing them to elute later than larger molecules that are excluded from the pores and thus pass through more quickly.<sup>99</sup>

This technique is particularly useful for the fractionation of proteins and polymers, as well as for sample cleanup by removing small molecules from complex matrices.<sup>106</sup> In bioprocessing, SEC is commonly used as an intermediate or polishing step due to its low selectivity, often following salt precipitation or other chromatography steps, and is typically coupled with a concentration procedure.<sup>99</sup>

#### 1.2.4.5 Mixed-mode chromatography

Mixed-mode chromatography (MMC) refers to chromatographic systems that combine two or more distinct interaction mechanisms, typically hydrophobic, ionic, and polar interactions, within a single stationary phase.<sup>107</sup> This multimodal approach has gained increasing popularity due to its enhanced selectivity, capacity, and separation efficiency for complex sample matrices, including those containing peptides or macromolecules.<sup>107</sup>

Unlike conventional single-mode stationary phases, which rely on a dominant interaction mechanism such as hydrophobicity (in reversed-phase chromatography, RPC) or polarity (in hydrophilic interaction chromatography, HILIC), MMC stationary phases integrate multiple retention modes.<sup>108</sup> This enables more nuanced separations and greater flexibility in method development.<sup>108</sup> The most common combinations include reversed-phase/ion-exchange (RP/IEC), reversed-phase/HILIC, and even tri-modal systems with additional functionalities.<sup>108</sup>

The multimodal behaviour arises from chemically modifying the stationary phase with ligands bearing multiple functional groups. These include ionic liquids, peptides, calixarenes, or imidazole derivatives, often tethered onto silica or polymeric supports. Such modifications allow MMC media to retain both polar and nonpolar analytes

simultaneously or sequentially, depending on mobile phase conditions such as pH or salt content.<sup>107, 108</sup>

Recent advancements in the field have led to the development of novel MMC materials with improved salt tolerance, selectivity, and stability.<sup>108</sup> These have proven especially valuable for biomolecule purification, such as monoclonal antibodies and serum proteins, where MMC resins can reduce the number of steps and offer better control over process selectivity.<sup>108</sup>

### 1.3 Chromatographic modelling

The complexity of modern biopharmaceuticals, particularly monoclonal antibodies and their variants, demands highly sophisticated downstream processes to ensure purity, efficacy, and consistency.<sup>109</sup> As outlined in the preceding chapter, preparative chromatography provides the backbone of these purification workflows, employing multiple modalities across resin-, membrane-, and monolith-based platforms. However, the increasing structural heterogeneity of biologics, coupled with stringent regulatory expectations and economic pressures, has pushed the field toward more predictive, knowledge-driven process development.<sup>110-112</sup> It is in this context that mechanistic modelling and simulation have emerged as indispensable tools.<sup>113-116</sup>

Traditionally, chromatographic process design relied heavily on empirical approaches involving extensive experimentation<sup>117</sup>. While effective, this method is resource-intensive and often yields limited process understanding.<sup>118</sup> In contrast, mechanistic models enable a quantitative description of chromatographic behaviour, grounded in physical principles such as mass transfer.<sup>112, 118, 119</sup> These models provide a powerful framework for simulating and optimizing operating conditions, and even predicting outcomes for untested scenarios.<sup>119, 120</sup>

Further, the modelling of chromatography allows for deeper insight into critical factors such as the influence of ligand density<sup>121</sup>, pore diffusion<sup>122</sup> and protein binding kinetics<sup>123</sup>, all of which are essential when separating closely related product variants like charge variants<sup>124</sup>. Moreover, with the growing demand for continuous bioprocessing and process intensification, robust modelling frameworks are crucial for successful scale-up and to reduce development timelines through *in silico* experimentation.<sup>120, 125, 126</sup>

This chapter introduces the theoretical and computational foundations of chromatography modelling.

### 1.3.1 Modelling Software

The complexity of modern chromatographic processes, especially in the purification of monoclonal antibodies and their charge variants, requires the use of reliable and adaptable modelling software. These tools enable researchers to simulate column behaviour under various operating conditions, performing sensitivity analyses<sup>112</sup>, estimating parameters<sup>51, 113, 114</sup>, and optimizing process designs<sup>114, 118</sup> without relying solely on costly and time-consuming experimental trials. In this context, modelling software serves as a practical bridge between theory and application, translating transport equations and adsorption isotherms into actionable predictions.

A variety of modelling platforms are available, each offering distinct strengths in terms of flexibility, computational speed, and ease of use. The choice of software often depends on the specific goals of the modelling effort, ranging from rapid prototyping and teaching to high-resolution simulation and deep learning-based model inference.

#### 1.3.1.1 MATLAB

MATLAB is one of the most widely used platforms in chromatography modelling due to its versatility, strong numerical solvers, and extensive visualization capabilities.<sup>127-129</sup> It provides an accessible environment for implementing lumped or general rate models, solving partial differential equations (PDEs), and fitting model parameters using optimization routines such as `lsqnonlin` or `fmincon`.<sup>127-129</sup> MATLAB is utilized in both academic and industrial environments to develop custom simulation frameworks, providing full control over model structure and discretization schemes, such as finite difference and orthogonal collocation methods.<sup>130</sup> Its toolboxes support symbolic computation, and automated parameter estimation<sup>130</sup>, making it a go-to solution for developing tailored chromatography models. Due to its flexibility and powerful solver toolkits, MATLAB is used in the context of this thesis as a tool for isotherm parameter estimation.

### 1.3.1.2 CADET (Chromatography Analysis and Design Toolkit)

CADET (Chromatography Analysis and Design Toolkit) is an open-source simulation framework for modelling preparative chromatography with a strong emphasis on mechanistic accuracy and numerical efficiency.<sup>131, 132</sup> Originally developed at Forschungszentrum Jülich, CADET is built around a high-performance C++ solver capable of handling stiff partial differential-algebraic equations with support for multi-component transport and advanced adsorption models such as Steric Mass Action and competitive Langmuir.<sup>131, 132</sup>

Its modular structure enables the flexible composition of unit operations, such as columns, tanks, and valves, into complex process networks.<sup>131, 132</sup> CADET supports gradient-based optimization, sensitivity analysis, and uncertainty quantification, making it a powerful tool for model calibration, process development, and digital twin applications.<sup>131, 132</sup> Through its Python interface (CADET-Process), the platform is accessible to both modelers and process engineers.<sup>131, 132</sup>

CADET's open architecture and strong performance make it a transparent and extensible alternative to commercial tools, widely used in academia and industry for simulation, scale-up, and *in silico* optimization of chromatographic processes.<sup>131, 132</sup>

### 1.3.1.3 Berkeley Madonna

Berkeley Madonna is a user-friendly, equation-based modelling environment designed for rapidly building and solving ordinary differential equation (ODE) systems.<sup>133</sup> It excels in intuitive model construction and real-time simulation, making it particularly suitable for educational contexts and quick conceptual prototyping in life sciences and engineering.<sup>133</sup> Its graphical user interface allows users to construct models either by entering equations directly in mathematical notation or by using a flowchart-style graphical interface, where dynamic systems are visually assembled from components such as reservoirs, flows, and formulas.<sup>133</sup> Although not as specialized as platforms like CADET or MATLAB, Berkeley Madonna has proven highly valuable for early-stage modelling of biochemical systems and compartment-based pharmacokinetics due to its simplicity and speed. In chromatography modelling, it can effectively describe lumped kinetic models when spatial resolution is not critical, enabling the simulation of dynamic mass balances and kinetic behaviour with minimal programming effort.

## 1.4 Theoretical considerations

### 1.4.1 Transport Phenomena

Chromatographic separation processes can be described by a combination of thermodynamic and kinetic principles that determine how solutes migrate, interact, and are retained within the chromatographic system.<sup>123, 134</sup> At the core of this behaviour lies the concept of transport phenomena, which describes how mass moves through the mobile and stationary phases. Accurate representation of these mechanisms is essential for predicting column performance, optimizing process conditions, and developing mechanistic models.<sup>61</sup>

During a chromatographic process, the movement of solutes through a packed column or membrane is impacted by many different phenomena, which define the retention time, peak shape, and resolution observed during chromatographic separations. A complete model must account for both the rate at which solutes move and the equilibrium they attain with the stationary phase. Therefore, a model should include the following:

- Axial convection: The primary mechanism by which the solute is transported along the column, driven by the bulk flow of the mobile phase.<sup>60, 118, 135</sup>
- Axial dispersion: A secondary effect caused by non-uniform velocity profiles, eddy diffusion, and molecular diffusion, leading to band broadening.<sup>60, 118, 135</sup>
- Film diffusion (external mass transfer): The transfer of solute from the bulk mobile phase to the surface of the stationary phase particles.<sup>60, 118, 135</sup>
- Intraparticle diffusion (internal mass transfer): The diffusion of solutes within the porous structure of the particle to the active binding sites.<sup>60, 118</sup>
- Adsorption and desorption kinetics: The reversible interaction of the solute with functional groups on the stationary phase.<sup>60, 118</sup>

This thesis employs a lumped rate model (LRM) to describe transport dynamics. The lumped rate model (LRM) is a simplification of the general rate model that strikes a

balance between physical accuracy and computational efficiency. It assumes that transport within the column can be represented using averaged, or "lumped," parameters for mass transfer, rather than resolving detailed internal particle diffusion explicitly.<sup>61</sup> It is given by:

$$\frac{\partial c_i}{\partial t} + v \frac{\partial c_i}{\partial x} + \frac{(1 - \varepsilon)}{\varepsilon} \varepsilon_p k_{d,i} \frac{\partial q_i^*}{\partial t} = D_{ax} \frac{\partial^2 c_i}{\partial x^2} \quad (1)$$

Where  $c_i$  is the concentration of component  $i$  in the mobile phase,  $\varepsilon$  denotes the interstitial porosity and  $\varepsilon_p$  is the particle porosity.  $k_{d,i}$  is the pore exclusion factor of component  $i$ , describing the accessibility of said component into the pore structure of the stationary phase. It ranges between values of 0 and 1, which correspond to no accessibility and full accessibility respectively. For example, ions are modelled using a  $k_d$  value of 1. Further, the averaged concentration of an adsorbed component  $i$  is given by  $q_i^*$  and the axial dispersion is denoted by  $D_{ax}$ .

To describe mass transfer throughout the column, a linear driving force approximation is utilised as shown in:<sup>61, 136</sup>

$$\frac{\partial q_i^*}{\partial t} = k_{eff,i} \cdot \frac{6}{d_p} \cdot (q_{eq,i}^* - q_i^*) \quad (2)$$

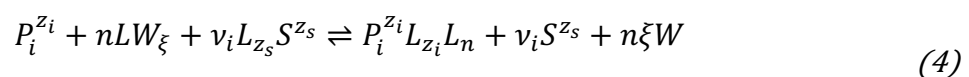
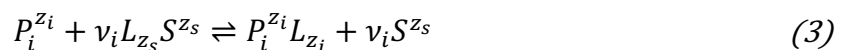
Where  $k_{eff,i}$  is the effective mass transfer coefficient, a lumped parameter, including film and mass transfer resistances.<sup>61</sup>  $d_p$  is the particle diameter of the resin particles. The full term  $\frac{6}{d_p}$  denotes the specific surface area, available for mass transfer. For membranes, this term is not applicable due to the geometry not being particulate. Therefore, in this thesis, the term is omitted, leading to a special mass transfer coefficient  $k_{eff,i}^{mem}$ . The averaged concentration of adsorbed component  $i$  in the accessible pore volume, which is in equilibrium with its mobile phase concentration is given by  $q_{eq,i}^*$ .<sup>6</sup>

### 1.4.2 Adsorption Isotherms

An essential component of any mechanistic chromatography model is the adsorption isotherm, which describes the equilibrium relationship between the solute concentration in the mobile phase and its bound concentration in the stationary phase. While transport phenomena govern the kinetics of how fast a solute moves and binds within the column, adsorption isotherms define how much solute can be retained under given conditions. Together, these elements form the dynamic backbone of predictive chromatographic simulations.

Adsorption isotherms capture the thermodynamic driving force for solute retention and separation and are particularly critical when modelling systems involving nonlinear binding behaviour or competitive interactions. They directly influence the shape of elution profiles, column loading capacity, and peak asymmetry, making them indispensable for both process design and scale-up.

The following stoichiometric expressions are used to describe and obtain the isotherm formalisms for the model with the simplest being an ion exchange model<sup>137, 138</sup> and a second describing additional hydrophobic interactions for a mixed-mode isotherm<sup>52, 139</sup>:



The ion exchange mechanism (3) is governed by a competitive interaction between the charged protein species  $P_i^{z_i}$  and salt counterions  $S^{z_s}$ , both of which compete for binding to the oppositely charged functional groups  $L$  present on the stationary phase. This interaction can be represented as a stoichiometric exchange, where proteins with a characteristic charge  $v$  are displaced or exchanged with salt ions bearing the charge number  $z_i$ . The mixed-mode interactions are very similar; however, the protein  $P_i^{z_i}$  additionally interacts with  $n$  hydrophobic binding sites on the ligand, forming a protein-ligand complex, releasing  $\xi$  numbers of solvent molecule  $W$ .

The thermodynamic equilibrium constant  $K_{eq}$  for the ion exchange mechanism this exchange reaction is given by:<sup>113, 137</sup>

$$K_{eq,i} = \frac{\hat{a}_i a_s^{v_i}}{a_i \hat{a}_s^{v_i}} = \frac{\hat{x}_i x_s^{v_i} \hat{\gamma}_i \gamma_s^{v_i}}{x_i \hat{x}_s^{v_i} \gamma_i \hat{\gamma}_s^{v_i}} = \frac{q_i}{c_i} \left( \frac{c_s}{\bar{q}_s} \right)^v \frac{\hat{\gamma}_i \gamma_s^{v_i}}{\gamma_i \hat{\gamma}_s^{v_i}} \quad (5)$$

The protein and the salt are represented by their activity  $a$ , their mole fraction  $x$ , and their activity coefficient  $\gamma$ . Adsorbed species are indicated by circumflex. Subscripts denote whether the parameter refers to the protein ( $i$ ) or the salt ( $s$ ). The molar concentrations of the adsorbed protein  $q_i$  and salt  $q_s$  are obtained by multiplying the mole fraction by the molar density  $c$  within the pore volume. Likewise, the molar concentrations in the liquid phase are represented as  $c_i$  for the protein and  $c_s$  for the salt. It is important to note that the bar above  $q_s$  highlights that only counterions bound and available for exchange with the protein are factored into the equilibrium.

The thermodynamic equilibrium constant  $K_{eq}$  for equation 4 can be modelled using the activities as analogue to equation 5:<sup>52</sup>

$$K_{eq,i} = \frac{\hat{a}_i a_s^{v_i} a_W^{n_\xi}}{a_i \hat{a}_s^{v_i} \hat{a}_W^n} = \frac{\hat{x}_i x_s^{v_i} x_W^{n_\xi} \hat{\gamma}_i \gamma_s^{v_i}}{x_i \hat{x}_s^{v_i} \hat{x}_W^n \gamma_i \hat{\gamma}_s^{v_i} \hat{\gamma}_W^n} \frac{1}{a_W^{n_\xi}} = \frac{q_i}{c_i} \left( \frac{c_s}{\bar{q}_s} \right)^v \left( \frac{c}{c_W} \right)^n \left( \frac{1}{\gamma_i} \right) a_W^{n_\xi} \quad (6)$$

The equilibrium constant is directly associated with the change in free Gibbs energy ( $\Delta G_{IEC,i}^0$ ), which, for the exchange reaction in can be expressed as follows:<sup>140, 141</sup>

$$-RT \ln K_{eq,i} = \Delta G_{IEC,i}^0 = \Delta G_{MMC,i}^0 \quad (7)$$

with

$$\Delta G_{IEC,i}^0 = \hat{\mu}_i^0 + v_i \mu_s^0 - \mu_i^0 - v_i \hat{\mu}_s^0 = \Delta G_{IEC,i}^0 - v_i \Delta G_s^0 \quad (8)$$

$$\Delta G_{MMC,i}^0 = \hat{\mu}_i^0 + v_i \mu_s^0 - \mu_i^0 - v_i \hat{\mu}_s^0 - RT \ln \gamma_i^{\infty,W} = \Delta G_{MMC,i}^0 - v_i \Delta G_s^0 \quad (9)$$

With  $R$  and  $T$  denoting the universal gas constant and the absolute temperature, respectively. While  $\mu_i^0$  and  $\mu_s^0$  represent the reference state chemical potentials of the protein ( $i$ ) and the counterion ( $s$ ),  $\hat{\mu}_i^0$  and  $\hat{\mu}_s^0$  denote analogous parameters for the adsorbed species. The change of Gibbs energy of adsorption of component  $i$  is given by  $\Delta G_i^0$  while the change of Gibbs energy of association with the counterion is represented by  $\Delta G_s^0$ .

### 1.4.3 The SMA Model

#### 1.4.3.1 Ion Exchange Isotherm

The protein adsorption equilibrium in ion-exchange chromatography is described by the steric mass action (SMA) model.<sup>142</sup> One of its key features is the inclusion of the steric shielding factor  $\sigma_i$ , which accounts for the number of adjacent binding sites blocked on the stationary phase due to the steric hindrance caused by protein binding.<sup>142</sup> In the SMA model, this leads to a reduction of bound counterions available for exchange, which is given by the following expression:<sup>142</sup>

$$\bar{q}_s = \Lambda - (\sigma_i + \nu_i)q_i \quad (10)$$

with  $\Lambda$  the ionic capacity (mol L<sup>-1</sup><sub>pore Volume</sub>). Rearranging after combining Eq. (10) and Eq. (5) leads to the expression for a single-component SMA isotherm<sup>141, 142</sup>:

$$\frac{q_i}{c_i} = K_{eq,i} \frac{\gamma_i \hat{\gamma}_s^{\nu_i}}{\hat{\gamma}_i \gamma_s^{\nu_i}} \left( \frac{\Lambda - (\sigma_i + \nu_i)q_i}{c_s} \right)^{\nu_i} = K_{eq,i} \frac{\gamma_i \hat{\gamma}_s^{\nu_i}}{\hat{\gamma}_i \gamma_s^{\nu_i}} \left( \frac{\Lambda}{c_s} \right)^{\nu_i} \left( 1 - \frac{q_i}{q_{max,i}} \right)^{\nu_i} \quad (11)$$

Where  $q_{max,i}$  is the theoretical maximal binding capacity. At very low protein concentrations ( $q_i \rightarrow 0$ ), the initial slope of the adsorption isotherm, expressed by the distribution coefficient  $A_i$  is given by<sup>143</sup>:

$$A_i = \frac{q_i}{c_i} = K_{eq} \left( \frac{\Lambda}{c_s} \right)^{\nu} \tilde{\gamma}_i \quad (12)$$

Due to the dependence of  $K_{eq}$  on  $\nu_i$ , and the further dependence of  $\nu_i$  on pH, this model exhibits a general pH dependency through these parameters. The pH dependency of  $\nu_i$  is given by its description using a protein net charge model, where the characteristic charge  $\nu_i = z_i/z_s$  can be calculated from: <sup>6, 101, 144</sup>

$$z_i = \sum_i \frac{-N_{-i}}{1 + 10^{pK_{a,i} - pH}} + \sum_i \frac{N_{+i}}{1 + 10^{pH - pK_{a,i}}} \quad (13)$$

where  $N_{-i}$  and  $N_{+i}$  are the number of contributing acidic amino acids and basic amino acids respectively. <sup>6, 101, 144</sup> Since  $z_s$  is 1 in the case of NaCl as modifier,  $\nu$  equals  $z_i$ .

#### 1.4.3.2 Mixed-Mode Isotherm

For a mixed-mode isotherm, the concentration of bound counterions is given by:

$$\bar{q}_s = \Lambda_{IEC} - (\sigma_i + \nu_i)q_i \quad (14)$$

Where  $\Lambda_{IEC}$  is the ligand density of the ionic part of the mixed-mode ligands. Further, the molar concentration of hydrated hydrophobic ligands is given by<sup>52</sup>:

$$c_w = \Lambda_{HIC} - (n + \delta)q_i \quad (15)$$

Where  $\Lambda_{HIC}$  is the hydrophobic ligand density of the mixed-mode media and  $\delta$  denotes steric hindrance factor of the hydrophobic interaction. Inserting (14) and (15) into (6) and rearranging, the single component mixed-mode isotherm can be described as:

$$\frac{q_i}{c_i} = K_{eq,i} \frac{\gamma_i \hat{\gamma}_s^{v_i}}{\hat{\gamma}_i \gamma_s^{v_i}} \left( \frac{\Lambda_{IEC} - (\sigma_i + v_i) q_i}{c_s} \right)^{v_i} \left( \frac{\Lambda_{HIC} - (n + \delta) q_i}{c} \right)^n \left( \frac{1}{a_W^{n\xi}} \right) \quad (16)$$

Which can be expressed in terms of maximal protein binding capacity:

$$\frac{q_i}{c_i} = K_{eq,i} \left( \frac{\Lambda_{IEC}}{c_s} \right)^{v_i} \left( \frac{\Lambda_{HIC}}{c} \right)^n \left( 1 - \frac{q_i}{q_{max,IEC,i}} \right)^{v_i} \left( 1 - \frac{q_i}{q_{max,MMC,i}} \right)^n \left( \frac{1}{a_W^{n\xi}} \right) \tilde{\gamma}_i \quad (17)$$

Where  $q_{max,IEC,i} = \Lambda_{IEC}/(\sigma_i + v_i)$  and  $q_{max,MMC,i} = \Lambda_{HIC}/(n + \delta)$  according to Lee et al.<sup>52</sup> For very low protein concentrations ( $q_i \rightarrow 0$ ), the initial slope of the mixed-mode adsorption isotherm, expressed by the distribution coefficient  $A_i$  is given by:<sup>52</sup>

$$A_i = K_{eq,i} \left( \frac{\Lambda_{IEC}}{c_s} \right)^{v_i} \left( \frac{\Lambda_{HIC}}{c} \right)^n \left( \frac{1}{a_W^{n\xi}} \right) \tilde{\gamma}_i \quad (18)$$

#### 1.4.3.3 Asymmetry Coefficients

Three different activity coefficients are going to be compared to each other. The first one is given by:<sup>52, 145</sup>

$$\tilde{\gamma}_{Protein} = \exp(K_S c_s) \quad (19)$$

With  $K_S$  being an interaction parameter describing the salt-induced interaction in mixed-mode chromatography. A second activity coefficient is given by:<sup>51</sup>

$$\tilde{\gamma}_{Protein} = \exp(c_s K_S(pH)), \quad \text{with } K_S(pH) = \alpha \exp(pH \beta) \quad (20)$$

Further, an activity coefficient based on Kirkwood's theories on salting-in and salting-out is used to describe the proteins behaviour in low and high salt environment <sup>146, 147</sup>:

$$\tilde{\gamma}_{Protein} = \exp\left(-\frac{3N_A\eta_P\tau_P}{32\pi\varepsilon_D RT}\left(1 - \frac{\ln(1 + \tau_P\kappa^2)}{\tau_P\kappa^2}\right) + \frac{3}{2}\tau_P\phi\kappa^2\right) \quad (21)$$

where  $N_A$  is Avogadro's number and  $\varepsilon_D$  is the permittivity of the solvent. A concentration dependence of  $\varepsilon_D$  is not included since the influence is neglectable in this case.  $\eta_P$ ,  $\tau_P$  and  $\phi$  are parameters from Kirkwood's salting-in and salting-out models. For more information on their physical meaning, please refer to <sup>147</sup>.  $\kappa$  is the inverse of the Debye length:

$$\kappa^2 = \frac{2F^2\xi C_s}{\varepsilon_D RT} \quad (22)$$

with  $F$  being the Faradays constant. Equation 6 is slightly modified to allow the usage of molar concentrations instead of ionic strength. Therefore,  $\xi$  is introduced as a factor to account for the differences in ionic strength when using multivalent modifiers. Table 1 shows values for the factor for various ion pairings. Since this work uses sodium sulphate, a factor  $\xi = 3$  was used. This method can only be used if one considers the salt as only and main contributor to ionic strength.

Table 1: Factors for different ion pairings

Electrolyte	1:1	1:2	1:3	2:2
Factor $\xi$	1	3	6	4

#### 1.4.4 Linear gradient elution experiments

Linear salt and pH gradient elution was performed. For the evaluation of linear gradient elution experiments, a method based on Yamamoto et al. <sup>148</sup> and adapted by Pedersen

et al.<sup>143</sup> was used. The relationship between eluting modifier concentration and normalized gradient slope is as follows:

$$GH_M = \int_{c_{M,init}}^{c_{M_i,elu}} \frac{1}{(k_{d,i}A_i(c_s) + k_{d,i} - 1)} dc_s \quad (23)$$

with the normalized gradient slope  $GH_M$ , the initial modifier concentration  $c_{M,init}$ , the modifier concentration at which the protein  $i$  elutes  $c_{M_i,elu}$ , the exclusion factor of protein  $i$   $k_{d,i}$ , and the distribution coefficient  $A_i$ . Differentiation with respect to the salt concentration or pH value<sup>50, 101, 144</sup> leads to:

$$\frac{dGH_{salt}}{dc_{s,elu}} = \frac{1}{k_{d,i} \left( A_i + 1 - \frac{1}{k_{d,i}} \right)} = \frac{dGH_{pH}}{dpH_{elu}} \quad (24)$$

The normalized gradient slope for a pH or salt gradient can be calculated based on Pederson et al.:<sup>143</sup>

$$\begin{aligned} GH_{salt} &= g_{salt}(V_C(1 - \varepsilon)\varepsilon_p) = \frac{c_{salt,final} - c_{salt,init}}{V_g} (V_C(1 - \varepsilon)\varepsilon_p) \\ GH_{pH} &= g_{pH}(V_C(1 - \varepsilon)\varepsilon_p) = \frac{c_{pH,final} - c_{pH,init}}{V_g} (V_C(1 - \varepsilon)\varepsilon_p) \end{aligned} \quad (25)$$

where  $g$  refers to the gradient slope,  $V_g$  is the gradient volume, and  $V_C$  is the total column volume. Further,  $\varepsilon$  denotes the interstitial bed porosity and  $\varepsilon_p$  the intra-particle porosity. *Init* and *final* represent the initial and final mobile phase modifier concentration respectively.

## 1.5 Aim of the work

This dissertation investigates how the physicochemical properties of novel multimodal ligands influence protein chromatography, with a particular focus on the separation of monoclonal antibody (mAb) charge variants. In light of the increasing structural complexity of biopharmaceuticals and the inherent limitations of conventional chromatographic methods, the work seeks to develop a mechanistic understanding of protein-ligand interactions in multimodal systems and to establish predictive modelling frameworks that support advanced purification strategies.

Using mixed-mode cation exchange resin (Eshmuno® CMX) and mixed-mode membrane systems (Natrix® CH), the study systematically explores the retention and separation behaviour of charge variants of a model mAb under varying pH and salt gradient conditions. By applying linear gradient elution protocols and dual-gradient strategies, the work aims to investigate how ionic strength, pH, and hydrophobicity modulate protein binding and elution profiles. Particular attention is given to analysing and optimizing the separation of closely related isoforms.

To describe and simulate the observed behaviour, mechanistic models shall be based on the Steric Mass Action (SMA) isotherm and its multimodal extensions are developed. These models are implemented in MATLAB® and validated through extensive experimental data. Different types of activity coefficients, including empirical, pH-dependent, and Kirkwood-based formulations, are evaluated for their ability to improve the thermodynamic accuracy of the simulations.

Through this integrated experimental and computational approach, the thesis aims to support the development of robust, scalable, and high-resolution purification processes for complex biopharmaceuticals. It contributes to advancing Quality by Design (QbD) principles in downstream processing and provides tools for reducing reliance on trial-and-error in bioprocess development.

## 2 MATERIALS AND METHODS

### 2.1 Materials

#### 2.1.1 Chemicals

Table 2: List of chemicals

<b>Chemical</b>	<b>Grade / Purity</b>	<b>Manufacturer</b>
<b>Acetic acid</b>	100%	Merck KGaA
<b>Blue Dextran</b>	-	Sigma-Aldrich
<b>CAPS</b>	≥ 99%	AppliChem GmbH
<b>CAPSO</b>	≥ 99%	AppliChem GmbH
<b>CHES</b>	≥ 99%	Merck KGaA
<b>Ethanol</b>	≥ 99.2%	Berkel AHK
<b>HEPES</b>	≥ 99.5%	Merck KGaA
<b>Hydrochloric acid (HCl)</b>	Titripur®	Merck KGaA
<b>L-Arginine Hydrochloride</b>	98.5–101%	AppliChem GmbH
<b>MES·H<sub>2</sub>O</b>	≥ 99%	AppliChem GmbH
<b>MOPSO</b>	≥ 99%	Merck KGaA
<b>Sodium azide (NaN<sub>3</sub>)</b>	≥ 99%	AppliChem GmbH
<b>Sodium chloride (NaCl)</b>	≥ 99.5%	Honeywell Int.
<b>Sodium hydroxide (NaOH)</b>	≥ 98%	Carl Roth GmbH & Co. KG
<b>Sodium sulphate</b>	≥ 99%	Merck KGaA
<b>Succinic acid</b>	≥ 99%	abcr GmbH
<b>TAPS</b>	≥ 99.5%	Merck KGaA

## 2.1.2 Devices and Hardware

Table 3: List of devices

<b>Apparatus</b>	<b>Technique / Description</b>	<b>Manufacturer</b>
<b>Agilent 8453</b>	UV-VIS spectrophotometer	Agilent
<b>Centrifuge 5415 R</b>	Benchtop centrifuge	Eppendorf
<b>ED4202S-CW</b>	Precision balance	Sartorius
<b>IKA® TER 2</b>	Tempered water bath	IKA®-Werke
<b>LF 537</b>	Conductivity meter	WTW
<b>Milli-Q® Gradient</b>	Water purification system	EMD Millipore
<b>R160P-*D1</b>	Analytical balance	Sartorius
<b>SenTix® 940</b>	pH electrode	Xylem Analytics Germany
<b>Sonorex Super 10 P</b>	Ultrasonic bath	BANDELIN electronic
<b>inoLab® Multi 9420 IDS</b>	pH meter	Xylem Analytics Germany
<b>ÄKTA micro</b>	HPLC system	GE Healthcare
<b>ÄKTA purifier 100</b>	FPLC system	GE Healthcare

## 2.1.3 Software

Table 4: List of software

<b>Name</b>	<b>Description / Application</b>	<b>Vendor</b>
<b>Berkeley Madonna</b>	Used to solve ordinary differential equation in rapid prototyping and isotherm development. Buffer calculation	R. Macey and G. Oster, University of California (Berkeley, USA)
<b>PeakFit</b>	Deconvolution of UV peak signals. Estimating peak centroids for LGE evaluation.	Grafiti LLC (California, USA)
<b>MATLAB</b>	Automated parameter estimation for modelling.	The MathWorks, Inc. (Massachusetts, USA)
<b>Python</b>	Data evaluation	Python Software Foundation
<b>TableCurve3D</b>	Empirical modelling	Grafiti LLC (California, USA)

## 2.1.4 Protein

The monoclonal antibody mAb02, used as the model protein in this study, was kindly provided by Merck KGaA (Darmstadt, Germany). The antibody, in its purified form, consists of mainly monomeric species with very little high molecular weights as confirmed by analytical size exclusion chromatography. Previous analytical cation exchange chromatography revealed a distinct charge variant profile. Prior to charge variant analysis, mAb02 was subjected to a capture purification step using Protein A affinity chromatography to isolate the IgG from clarified cell culture supernatant. Its extinction coefficient at a wavelength of 280 nm is  $1.41 \text{ mg mL}^{-1} \text{ cm}^{-1}$ .

## 2.1.5 Chromatographic material

### 2.1.5.1 Columns

Mechanistic modelling experiments were conducted using the mixed-mode chromatography resin Eshmuno® CMX (Merck KGaA, Darmstadt, Germany). This resin is based on a rigid, hydrophilic polyvinylether polymer matrix functionalized with both weak cation exchange groups ( $\text{COO}^-$ ) and hydrophobic alkyl ligands, enabling multimodal retention behaviour through simultaneous electrostatic and hydrophobic interactions with protein analytes. Further, a strong cation exchange resin Eshmuno® CPX was used for initial comparison studies.

For all experiments, the resins were supplied pre-packed by the manufacturer in standardized 1 mL plastic columns (0.5 cm inner diameter, 5 cm length), ensuring uniform packing quality and reproducibility. Further physicochemical properties of the Eshmuno® CMX resin, including particle size, ligand density, ionic capacity, pH and pressure stability, are reported as specified by the manufacturer and summarized in Table 5.

Table 5: Eshmuno® CMX resin and column specific parameters

Parameter	Symbol	Value	Unit
Total column volume	$V_c$	1.0	mL
Column length	$L_c$	5.0	cm
Column inner diameter	$ID$	0.5	cm
Particle diameter	$d_p$	0.005	cm
Interstitial porosity	$\varepsilon$	0.413	-
Intraparticle porosity	$\varepsilon_p$	0.755	-
Total porosity	$\varepsilon_t$	0.856	-
Exclusion factor	$k_{d,V1}$	0.6	-
	$k_{d,V2}$	0.6	-
	$k_{d,V3}$	0.6	-

---

Axial dispersion	$D_{ax}$	1.18E-03	cm <sup>2</sup> /s
Ionic capacity	$\Lambda$	0.218	mol L <sup>-1</sup>

---

For Protein A affinity purification of mAb02, a ProSep Ultra Plus resin column from Merck KGaA (26 mm inner diameter × 25.2 cm length, 133.8 mL column volume) was used. Analytical cation exchange chromatography (CEX) was performed using a YMC-BioPro SP-F column from YMC Europe GmbH (50 mm × 4.6 mm, 5 μm particle size, 0.83 mL column volume). For analytical size exclusion chromatography (SEC), a BioSep-SEC S3000 column from Phenomenex (300 mm × 7.8 mm, 5 μm particle size) was employed.

#### 2.1.5.2 Membranes

The Natrix® CH membrane (MilliporeSigma/Merck KGaA) used in this study is a mixed-mode chromatography membrane combining strong cation exchange and hydrophobic interaction functionalities. It features sulfonate groups for cation exchange and t-butyl ligands for hydrophobic interactions. The membrane is fabricated from a polyacrylamide hydrogel reinforced with polybutylene terephthalate (PBT), offering high permeability and mechanical stability for rapid chromatographic processing.

According to manufacturer specifications, the membrane supports flow rates up to 10 membrane volumes per minute and a maximum operating pressure of 5 bar. Under typical binding conditions (pH 7, 0.02 M sodium phosphate), the membrane exhibits a dynamic binding capacity exceeding 90 mg mL<sup>-1</sup> membrane volume (MV) for lysozyme and over 80 mg mL<sup>-1</sup><sub>MV</sub> for monoclonal antibodies.

Two membrane formats were used in this study. Both employed a flat-sheet configuration. The lab-scale device had a membrane volume of 1.06 mL and was housed in a syringe filter-style polypropylene casing. For scale-up experiments, a bench-scale membrane cassette with a volume of 8.8 mL was used. To ensure comparability between experimental scales, both modules contain membrane adsorber material from the same manufacturing batch.

Table 6: *Natrix® CH membrane specific parameters*

<b>Parameter</b>	<b>Symbol</b>	<b>Value</b>	<b>Unit</b>
<b>Ionic capacity</b>	$\lambda$	0.265 (lab-scale)	$\text{mol L}^{-1}_{\text{MV}}$
		0.258 (bench-scale)	
<b>Interstitial porosity</b>	$\varepsilon$	0.517	-
<b>Total porosity</b>	$\varepsilon_t$	0.89	-
<b>Exclusion factor</b>	$k_{d,v1}$	0.9	-
	$k_{d,v2}$	0.9	-
	$k_{d,v3}$	0.9	-
<b>Cross sectional area</b>	$A_c$	7.07 (lab-scale)	$\text{cm}^2$
		33.8 (bench-scale)	

## 2.2 Methods

### 2.2.1 Preparations

#### 2.2.1.1 Purification of mAb02 using protein A chromatography

For the Protein A purification, a ProSep Ultra Plus resin column (133.8 mL, 26 mm ID × 25.2 cm) was operated on an ÄKTA Purifier system (GE Healthcare) using UNICORN software. The column was equilibrated with binding buffer A (20 mM NaH<sub>2</sub>PO<sub>4</sub>, 150 mM NaCl, pH 7.4), and roughly 2 L of prefiltered, clarified cell culture supernatant ( $c = 1.3 \text{ mg mL}^{-1}$ ) was loaded at  $4.5 \text{ mL min}^{-1}$ . Following a wash with 10 CV of binding buffer at  $10 \text{ mL min}^{-1}$ , mAb02 was eluted within a 100% step to buffer B (25 mM citric acid, pH 2.8). The eluate was fractionated then neutralized to pH 5 with 1 M TRIS, filtered ( $0.2 \text{ }\mu\text{m}$ ), aliquoted, and stored frozen. This procedure was performed several times with differing batches of supernatant.

#### 2.2.1.2 CEX analysis

Charge variant analysis of purified mAb02 was performed using an analytical CEX method on an ÄKTA Micro system with an A-905 autosampler (GE Healthcare). A YMC-BioPro SP-F column ( $50 \times 4.6 \text{ mm}$ ,  $5 \text{ }\mu\text{m}$ ,  $0.83 \text{ mL CV}$ ) was used with a pH gradient elution from pH 5.0 to 9.5 over 27 CV, starting at 35% and ending at 80% buffer B at a flow rate of  $0.8 \text{ mL min}^{-1}$ . Buffer A (pH 5.0,  $30 \text{ mM Na}^+$ ) contained 8.8 mM acetic acid, 10 mM MES, 15.5 mM MOPSO, and 22.5 mM NaCl. Buffer B (pH 9.5,  $30 \text{ mM Na}^+$ ) contained 18.4 mM HEPES, 7.2 mM TAPS, 7.7 mM CHES, and NaOH for pH adjustment.

#### 2.2.1.3 SEC analysis

Size-exclusion chromatography (SEC) was used to assess the concentration, purity, and aggregate content of the protein A-purified mAb02. The analysis, performed by Rita Steigmiller<sup>149</sup>, was conducted on an HPLC system (Agilent Technologies) using a BioSep-SEC-S 3000 column. Samples ( $20 \text{ }\mu\text{L}$ , diluted to  $1 \text{ mg mL}^{-1}$  if necessary) were injected at a flow rate of  $1 \text{ mL min}^{-1}$ . The column was equilibrated with SEC buffer (100 mM NaH<sub>2</sub>PO<sub>4</sub>, 100 mM NaCl, pH 7.0).

#### 2.2.1.4 Preparative isolation of charge variants

To isolate the individual charge variants from the pre-purified mAb02, preparative cation exchange chromatography was performed using Eshmuno® CPX resin (Merck Life Science KGaA). The resin was packed into a column (1 cm ID × 20 cm length, 15.7 mL bed volume). The separation was achieved by applying a dual-gradient elution strategy, in which the sodium chloride concentration was decreased from 0.0684 mol L<sup>-1</sup> to 0.057 mol L<sup>-1</sup> while the pH was simultaneously increased from 5.5 to 8.8 over 50 column volumes. This antiparallel gradient was designed to maximize resolution between closely eluting isoforms by leveraging both ionic strength and pH modulation.

Both Buffer A (pH 5.5) and Buffer B (pH 8.8) contained identical buffering components. These are 16 mM acetic acid, 12 mM MES, 4 mM MOPSO, 9 mM HEPES, 8 mM TAPS, and 13 mM CHES. The two buffers differed in salt composition. Buffer A included 0.0518 M NaCl and 0.0166 M NaOH, while Buffer B contained 0.0074 M NaCl and 0.0496 M NaOH. Final pH adjustments were made with HCl.

The elution profile exhibited three main peaks corresponding to the acidic (pI ≈ 8.15), neutral (pI ≈ 8.30), and basic (pI ≈ 8.45) variants, as previously identified by analytical cation exchange chromatography. Fractions from the apex of each peak were collected separately to ensure minimal cross-contamination.

### 2.2.2 Modelling of liquid chromatography

#### 2.2.2.1 Chromatographic Systems

Preparative chromatographic separations employing linear gradient elution were conducted using an ÄKTApurifier™ 100 system (GE Healthcare, Chicago, IL, USA). For analytical-scale protein assessments, including concentration and purity checks, an ÄKTAmicro™ system (GE Healthcare) was utilized.

#### 2.2.2.2 Linear salt and pH gradient calculation

To achieve high-resolution separation of mAb02 charge variants by pH and salt gradient elution, the gradients were constructed to approximate a linear increase across a defined pH or salt range. For pH gradients, this was accomplished by selecting and combining buffering substances with overlapping pKa values in appropriate concentrations to maintain a near-constant buffer capacity throughout the

gradient. A consistent buffer capacity ensures a linear titration curve, which translates into a linear pH profile when buffer A and buffer B are mixed in varying proportions.

To support this process, custom software tools were developed in both Berkeley Madonna™ and Python. These tools computed the required concentrations of each buffer component based on the formal definition of buffer capacity, expressed as the derivative of the amount of strong base added with respect to pH ( $\beta = \frac{dC_b}{dpH}$ ), using the equations and concepts outlined by Urbansky and Schock (2000).<sup>150</sup> The software calculated the combined buffer capacity of the multi-component system and iteratively refined the composition to maintain a uniform capacity across the targeted pH range.

Initially, buffer design was based on homogeneous systems, where buffer A and buffer B contained the same buffering substances at identical concentrations but at different pH values. To increase flexibility and allow finer control, the approach was expanded to include heterogeneous buffer systems, in which buffer A and buffer B differ in both composition and concentration of buffer substances.

The buffer compositions were optimized across different salt conditions. Since pKa values are dependent on ionic strength, buffer recipes were recalculated for higher or lower salt concentrations to maintain linearity. However, these variations were minor, and therefore, the composition for medium salt concentration will be presented for each modelling LGE setup, consisting out of a combination of the following buffer substances: Acetic acid, succinic acid, citric acid MES, MOPSO, HEPES, TAPS, CHES, CAPSO. Mixing these buffers in defined proportions generated a smooth and reproducible linear pH gradient.

In addition to linear pH gradients, salt gradients at constant pH were also implemented for certain experiments. To construct these, the same buffer system used for the pH gradient was adapted. Specifically, the ratio of buffer A (e.g., pH 4.5) and buffer B (e.g., pH 9.0) that would yield the target constant pH was calculated in advance. Based on this ratio, the absolute concentrations of buffering species were determined to prepare new buffer solutions with the same pH but differing salt concentrations. These were then used to generate a linear salt gradient by mixing the solutions across a defined volume range on the chromatography system. This allowed for modulation of ionic strength while maintaining a stable pH environment and comparable gradient composition throughout the elution process.

Following buffer calculation, each solution was prepared with strict adherence to cleanliness and precision to ensure reproducibility and chemical stability. All equipment, including beakers, spatulas, and volumetric flasks, was thoroughly rinsed with Milli-Q® water prior to use to prevent contamination. For each buffer, e.g. one litre was prepared using the calculated amounts of all components.

Solids were weighed to three decimal places using analytical balances. Substances were transferred quantitatively into 1 L beakers using Milli-Q® water. In the case of NaOH, which was available only as pellets and thus difficult to weigh precisely, a deliberate slight overweighing was performed. The excess sodium ions introduced by the additional NaOH were calculated and subsequently compensated by subtracting the equivalent amount of Na<sup>+</sup> from the NaCl or Na<sub>2</sub>SO<sub>4</sub> portion, ensuring accurate ionic strength. After weighing, the buffer components were dissolved in approximately 800 mL of Milli-Q® water under gentle stirring. Once fully dissolved, the pH was adjusted using HCl, and the solution was transferred to a volumetric flask and brought to exactly 1 L total volume. The final buffer was filtered to remove any particulate matter, transferred to pre-cleaned Schott bottles, and degassed for 20 minutes before use.

#### 2.2.2.3 Column chromatography (Eshmuno® CMX)

In the assessment of the physicochemical properties of the mixed-mode resin Eshmuno® CMX, sodium sulphate (Na<sub>2</sub>SO<sub>4</sub>) was utilized as a kosmotropic salt. Sodium ions served as counterions, while sulphate ions acted as co-ions. This salt enhanced the hydrophobic interactions between the stationary phase ligands and protein analytes, thereby influencing the resolution attained in mixed-mode separations.

##### 2.2.2.3.1 Linear gradient elution experiments

Linear gradient elution experiments were conducted individually for each of the three charge variant pools. A series of pH gradients ranging from pH 4.5 to 9.5 was applied at constant sodium ion concentrations between 0.1 mol L<sup>-1</sup> and 1.7 mol L<sup>-1</sup>. Additionally, salt gradients were performed over a concentration range of 0.066 mol L<sup>-1</sup> to 1.7 mol L<sup>-1</sup> Na<sup>+</sup> at fixed pH values between 5.2 and 7.2. Where applicable, both increasing and decreasing gradient slopes were investigated to evaluate retention characteristics under reversed conditions.

Gradient lengths of 40, 60, 80, and 120 column volumes (CV) were applied to study the influence of gradient slope on separation performance. A constant volumetric flow rate of  $0.65 \text{ mL min}^{-1}$  was used, corresponding to a linear velocity of approximately  $198 \text{ cm/h}$ . Protein loading was standardized at  $1 \text{ mg mL}^{-1}$  resin for all gradient experiments.

#### 2.2.2.4 Membrane Chromatography (Natrix® CH)

##### 2.2.2.4.1 Initial comparative binding and elution study

A dual-gradient from pH 4.5 to pH 9.0 and sodium chloride concentration from  $0.10 \text{ mol L}^{-1}$  to  $0.08 \text{ mol L}^{-1}$  was applied. A protein load of  $5 \text{ mg mL}^{-1}_{\text{MV}}$  was used, and elution profiles were compared to a conventional pure cation exchange membrane under identical conditions. Elution was monitored by UV, pH, and conductivity.

##### 2.2.2.4.2 Linear gradient elution experiments

Linear gradient elution studies were performed individually for each isolated charge variant (see 2.2.1.4) to evaluate retention behaviour under varying chromatographic conditions. These experiments comprised a series of pH gradients ranging from pH 4.5 to 9.0, conducted at constant sodium chloride concentrations between  $0.06 \text{ mol L}^{-1}$  and  $0.2 \text{ mol L}^{-1}$ . In addition, salt gradient experiments were conducted by increasing the NaCl concentration from  $0.03 \text{ mol L}^{-1}$  to  $0.8 \text{ mol L}^{-1}$  at fixed pH values of 4.5 and 5.0, allowing for decoupled analysis of ionic strength effects.

Gradient lengths were varied between 65 and 140 membrane volumes (MV) to assess the impact of gradient slope. All experiments were carried out at a fixed flow rate of  $10 \text{ mL min}^{-1}$ . The standard protein loading for these studies was  $0.6 \text{ mg per mL}$  of membrane volume ( $\text{mg mL}^{-1}_{\text{MV}}$ ).

##### 2.2.2.4.3 Dynamic binding capacity (DBC) determination

Dynamic binding capacity experiments were conducted using both the  $1.06 \text{ mL}$  lab-scale and  $8.8 \text{ mL}$  bench-scale Natrix® CH membrane devices. The experiments were performed at pH 5 in the presence of  $0.03 \text{ mol L}^{-1}$  sodium chloride, using a flow rate of  $1 \text{ MV min}^{-1}$ . Both membranes were assessed for their DBC at 10 % breakthrough ( $\text{DBC}_{10\%}$ ) and their DBC at 95 % breakthrough ( $\text{DBC}_{95\%}$ ).

Additional experiments with the 1.06 mL membrane at an elevated flow rate of 10 MV min<sup>-1</sup> (residence time 0.3 min) were conducted.

#### 2.2.2.4.4 High load experiments

A series of salt gradient elution experiments were conducted under increasing sample loads (5.75, 11.5, 23 and 35 mg mL<sup>-1</sup><sub>MV</sub>) and pH values (4.5, 5.0, 5.5 and 6.0), with NaCl gradients from 0.03 mol L<sup>-1</sup> to 0.8 mol L<sup>-1</sup>. Flow rate was 10 mL min<sup>-1</sup> and gradient volume 85 MV.

#### 2.2.2.5 Determination of model parameters

To support parameter estimation, data from the linear gradient elution experiments were first evaluated by determining the elution peak centroid using exponentially modified Gaussian (EMG) fits of the UV absorbance signal. This analysis was automated and performed in Python 3 using the *lmfit* module. The pH and sodium ion concentration at the centroid were extracted and paired with the corresponding normalized gradient slope, as defined by equation (25), providing the reference data for subsequent model fitting.

A MATLAB® software was developed to estimate model parameters based on experimental elution data. Within the MATLAB® environment, applicable equations were solved simultaneously using the classical fourth-order Runge-Kutta method. Parameter estimation involved minimizing the sum of squared errors (SSE) between simulated and experimental elution points. This optimization process utilized a combination of global and local algorithms, including Surrogate-Based Optimization (SBO), Genetic Algorithms (GA), and Simulated Annealing (SA), to comprehensively explore the parameter space. Multiple optimization runs from diverse initial guesses were conducted to ensure convergence toward a global minimum and enhance the robustness and reliability of the obtained parameter sets.

##### 2.2.2.5.1 Modelling of Eshmuno® CMX

Equation (24), (25) with (12) and (13) in combination with either (19), (20) or (21) were computationally resolved in unison within the MATLAB® based software. The unknown parameters of the model, including the standard Gibbs free energy  $\Delta G_s^0$ ,  $\Delta \widehat{G}_i^0$ , the hydrophobic binding sites  $n$ , as well as the number of amino acids partaking in the binding process ( $N_{\text{carb}}$ ,  $N_{\text{his}}$ ,  $N_{\text{tyr}}$ ,  $N_{\text{amine}}$  and  $N_{\text{n-term}}$ ), were discerned.

In addition, parameters related to the activity coefficient, i.e.  $K_s$ , along with  $\alpha$  and  $\beta$ , as well as  $\eta_p$ ,  $\tau_p$  and  $\phi$  were estimated. The acid dissociation constants ( $pK_a$ ) of the various amino acids and additional constants are itemized in Table 7.

Table 7: Constants used in the modelling process

Constant	Value
$pK_{a_{carb}}$	4.5
$pK_{a_{his}}$	6.5
$pK_{a_{tyr}}$	9.6
$pK_{a_{amine}}$	10.4
$pK_{a_{n-term}}$	7.5
$F$	96485 C/mol
$N_A$	6.02E+23
$R$	8.3145 J/(mol K)
$T$	298.15 K
$\epsilon_D$	6.73E-12 C <sup>2</sup> /(m J)

## 2.2.2.5.2 Modelling of Natrrix® CH

### 2.2.2.5.2.1 Calibration of the linear range of the adsorption isotherm

Analogous to the modelling performed in chapter 2.2.2.5.1, equation (24), (25) with (12) and (13) were simultaneously solved within the MATLAB® based software. The unknown parameters of the model were estimated by fitting the model to the acquired data including the standard Gibbs free energy  $\Delta G_s^0$ ,  $\Delta \widehat{G}_i^0$  as well as the number of amino acids contributing in the binding process ( $N_{carb}$ ,  $N_{his}$ ,  $N_{tyr}$ ,  $N_{amine}$  and  $N_{n-term}$ ).

### 2.2.2.5.2.2 Estimation of shielding factors

To estimate shielding factors, a Transport Dispersive Model (Eq. (1)) combined with the Steric Mass Action (Eq. (11)) model was implemented in Berkeley Madonna. High loading experimental data from chapter 2.2.2.4.4 served as the foundation for this

reverse fitting approach. Using Berkeley Madonna's built-in Nelder-Mead simplex algorithm, model simulations were iteratively optimized to minimize the root mean square deviation between simulated and experimental chromatograms over the specified time domain.

By systematically adjusting the shielding factor, simulated chromatograms were aligned with the experimental elution profiles. This procedure enabled the extraction of variant-specific shielding coefficients.

#### 2.2.2.6 Simulation and prediction of elution profiles

To enable accurate simulation and prediction of chromatographic elution behaviour, a mechanistic lumped rate model based on the Transport Dispersive Model (TDM) was implemented in Berkeley Madonna. The model was used to simulate the propagation of solutes through the membrane or resin bed under gradient elution conditions, considering axial dispersion, convection, mass transfer kinetics, and nonlinear adsorption.

Since the TDM is governed by coupled partial differential equations (PDEs), the model was discretized spatially using finite difference methods to convert the PDEs into a system of ordinary differential equations (ODEs). These ODEs were further combined with a linear driving force (LDF) approximation to describe mass transfer between the mobile and stationary phases. Adsorption phenomena were captured using an appropriate isotherm model, i.e. a Steric Mass Action (SMA) model in combination with or without activity coefficients. Model parameters, including axial dispersion coefficients, mass transfer coefficients, adsorption kinetics, and isotherm-specific parameters, were estimated as described in chapter 2.2.2.5.

The resulting stiff system of ODEs was solved using Berkeley Madonna's Rosenbrock solver, which is particularly suited for stiff systems arising from discretized transport-reaction models. The simulation was performed under predefined conditions, such as applied salt or pH gradients, flow rates, and sample loading. Time-dependent elution profiles were generated and compared with experimental chromatograms for validation. The model was used to simulate various experimental scenarios, including changes in gradient slope, loading conditions, and flow rates, to assess and predict retention behaviour and separation efficiency.

### 3 RESULTS

#### 3.1 Modelling and simulation of mAb charge variant separation on mixed-mode resin Eshmuno CMX®

##### 3.1.1 Linear gradient elution experiments

##### 3.1.1.1 Comparison of mixed-mode to traditional ion exchanger

Linear gradient elution experiments were conducted using three distinct monoclonal antibody charge variants, each previously isolated from a mAb02 stock sample via strong cation exchange chromatography (Eshmuno® CPX). This pre-purification step led to the preparation of highly enriched charge variant pools. These enriched pools were then subjected to further separation on the mixed-mode material Eshmuno® CMX using different gradients and conditions. The experimental part on the Eshmuno® CMX was performed by Nadine Kern<sup>151</sup>.

A resulting chromatographic profile is shown in Figure 1, where the left-hand graph shows the elution profile on the strong cation exchange resin Eshmuno® CPX and the right-hand graph displays the elution profile with the same conditions on Eshmuno® CMX.

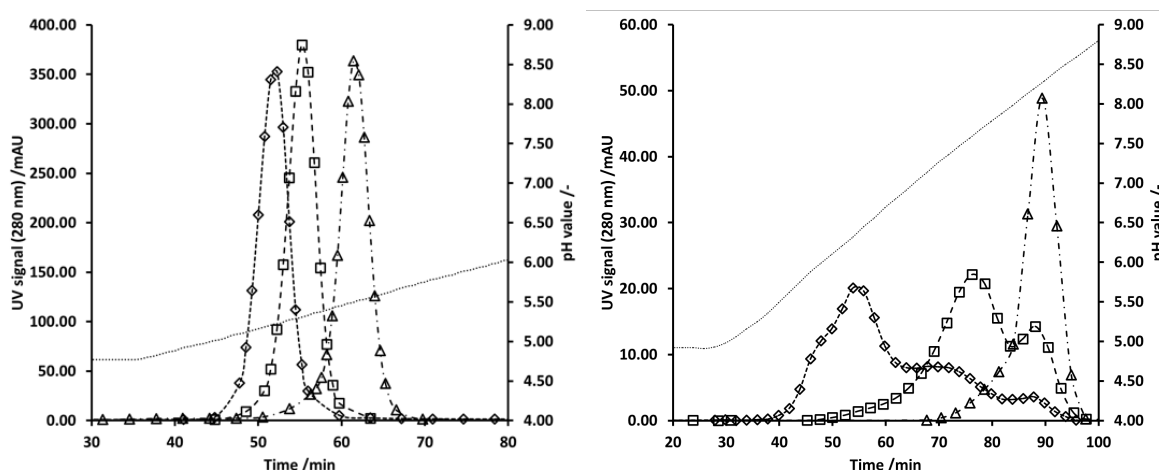


Figure 1: Comparison of elution profiles of mAb charge variants on strong cation exchange chromatography resin Eshmuno® CPX (left) and mixed-mode chromatography resin Eshmuno® CMX (right) using a pH gradient from pH 5 to pH 9 with Na<sup>+</sup> concentration of 0.2 mol L<sup>-1</sup>. The acidic variant is represented as rhombi, the neutral variant as squares and the basic variant as triangles.

Each graph displays the profiles of three distinct charge variants, where the acidic variant elutes first at a lower pH value, followed by the neutral variant and lastly the basic variant. The order of elution is the same in both results. However, the direct comparison reveals a noticeable shift in elution behaviour. While the elution order remained consistent, all variants eluted at later time points on Eshmuno® CMX compared to Eshmuno® CPX (Figure 1). The acidic, neutral and basic variant elute around pH 5.25, pH 5.37 and pH 5.54 on the cation exchange resin Eshmuno® CPX, respectively. Meanwhile they elute at pH 6.4 (acidic), pH 7.47 (neutral) and pH 8.3 (basic) on the Eshmuno® CMX mixed-mode resin.

#### 3.1.1.2 Additional separation on Eshmuno CMX® at medium high salt concentration

In Figure 1 in the right-hand graph, showing the elution on Eshmuno® CMX, further insights into the separation behaviour were gained at intermediate salt concentrations, particularly for the acidic and neutral variants. At these conditions, additional peaks within the main elution zones of these variants were revealed.

Under medium salt conditions, the acidic variant demonstrated up to four distinct peaks. The elution profile of the acidic variant spans the entire elution range observed for the other two variants. It begins with the highest peak, likely representing the main acidic variant, which also includes a pre-peak. This is followed by a third peak at approximately half the height of the main peak, and subsequently, a fourth peak that is roughly a quarter of the height of the main peak.

The neutral variant exhibited two distinct peaks, which differed in shape from the peaks observed in the acidic variants. Specifically, rather than showing a step-like pattern, the neutral variant displayed a primary peak on the left and a secondary peak of another sub-variant to its right.

The basic variant, which elutes latest in the linear gradient only exhibits a slight fronting.

These additional separations were mostly observed when elution conditions corresponded to the inflection point of the so-called “U-shaped” elution profiles. In the case of the example given in Figure 1, the conditions with 0.2 M sodium chloride led to the most pronounced observed separation.

### 3.1.1.3 U-shaped retention behaviour

To further investigate the previously mentioned separation behaviour, all pH gradient elution experiments at fixed salt concentrations and 120 CV were compared. Experimental data taken from Nadine Kern<sup>151</sup> and Pierre Braun<sup>152</sup>. The resulting chromatograms for all three variants (acidic, neutral, basic) exhibited a distinct trend: initial increases in salt concentration led to earlier elution of the main species (weaker retention), followed by a reversal where higher salt levels promoted stronger retention (Figure 2).

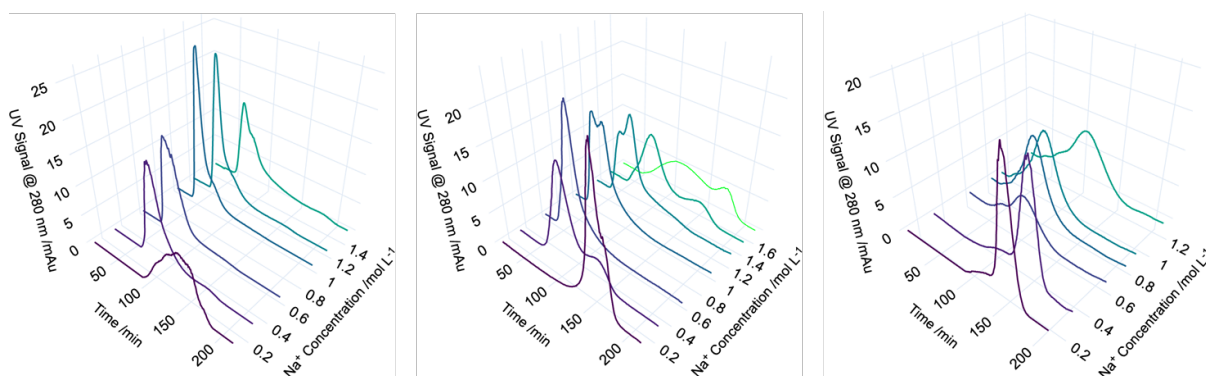


Figure 2: Resulting chromatograms of pH gradient elution experiments (pH 4.5 - 9.5) at various salt concentrations and constant gradient length (120 CV) for mAb02 acidic (left), neutral (middle) and basic (right) variant.

For the acidic variant, a visually stronger additional separation can be observed at 0.1 M and 1.5 M sodium chloride. For the neutral variant, additional separation is seen at 0.1 M, 0.3 M, 1.0 M, 1.3 M, 1.5 M, and 1.7 M sodium concentration. In comparison to the additional separation behaviour in form of split main peaks or peaks following the main peaks as seen for the acidic and neutral variant, the basic variant only shows fronting for salt concentrations of 0.2 M, 0.3 M, 0.8 M, 0.9 M and 1.2 M.

When taking all the data including linear pH and salt gradient elution experiments and plotting their respective elution pH versus elution Na<sup>+</sup> concentration (Figure 3), the data revealed characteristic U-shaped retention behaviour for all three variants.

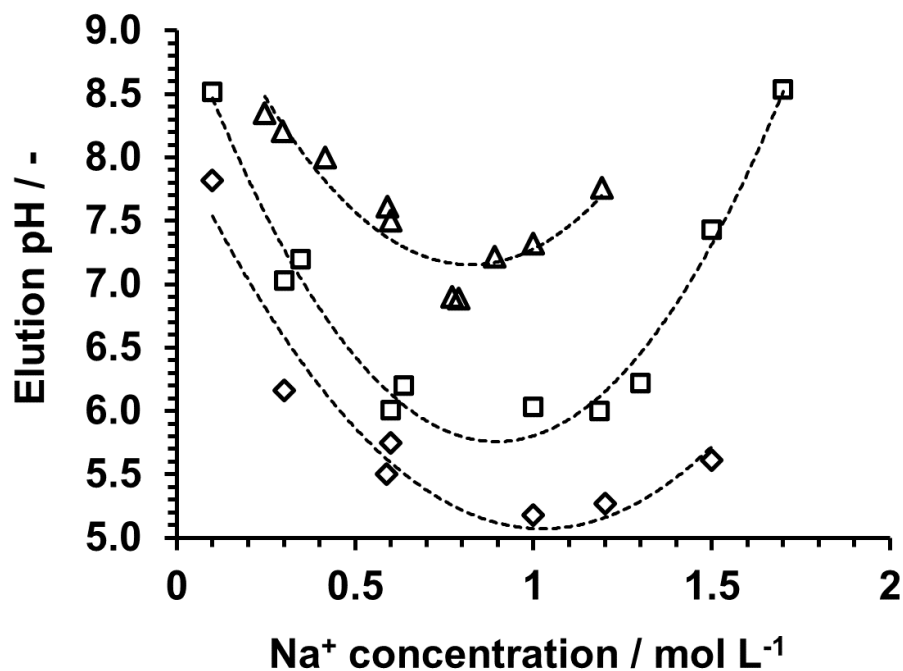


Figure 3: Elution pH and elution Na<sup>+</sup> concentration of the salt and pH gradient elution experiments for the acidic (rhombus), neutral (squares) and basic (triangles) variant. The dashed lines depict the trend of the individual data. All three charge variants show signs of “U-shaped” elution behaviour, i.e. a first decline of elution pH by increase of Na<sup>+</sup> concentration followed by an increase of the elution pH by further increase in Na<sup>+</sup> concentration.

The datapoints are represented by rhombuses (acidic variant), squares (neutral variant) and triangles (basic variant), while the dashed lines show the distinct course of the data with increasing salt concentration. As further depicted in Figure 3, the inflection points of the characteristic “U-shaped” elution curve shifted systematically depending on the variant. For the acidic variant, the U-curve was positioned lowest in terms of elution pH values, and the inflection point possesses the highest elution salt concentration, being about pH 5 and 1.0 M salt. The neutral variant's inflection point appeared above that of the acidic variant, showing a shift approximately 1 pH unit higher and 0.1 M lower in salt concentration. In turn, the basic variant's curve was observed still further above, marked by an additional shift of about 1.5 pH units upwards and 0.1 M to the left in salt, when compared to the neutral variant.

### 3.1.2 Mechanistic modelling of Eshmuno® CMX elution

In the following chapters, the results of the mechanistic modelling efforts aimed at describing protein retention behaviour during mixed-mode chromatography under varying pH and salt conditions are presented. The modelling work is divided into two main parts: the application of a steric mass action (SMA) model without activity coefficients and hydrophobic description, and the extension of this model to incorporate mixed-mode interactions as per Nfor et al.<sup>139</sup> and using different forms of activity coefficients. Since the experiments are in the linear range of the isotherm, the steric mass action model simplifies to a stoichiometric displacement model (SDM).

The goal was to assess the performance and limitations of these models in capturing the complex retention trends observed in both standard and reverse gradient experiments. Through systematic curve fitting procedures and extensive parameter estimation using automated MATLAB® scripts, critical behaviours such as the "U-shaped" elution trends and the interplay between ionic and hydrophobic interactions were identified. As for the data, which was used for fitting within MATLAB®, it was generated by evaluating all linear gradient elution experiments and condense them to just their elution conditions and normalized gradient slopes according to equation (24) and (25).

#### 3.1.2.1 Mechanistic modelling using a stoichiometric displacement (SD) model

Figure 4 presents the results of the curve fitting procedure using the SD model without additional activity coefficient, i.e. setting it to unity. The graphs illustrate the data points derived from the linear gradient elution experiments. These data can be categorized into subsets, each representing a specific condition, such as a pH gradient at a constant salt concentration or a salt gradient at a constant pH value. Each subset comprises four individual points, corresponding to experiments conducted under the specified conditions at four different gradient slopes.

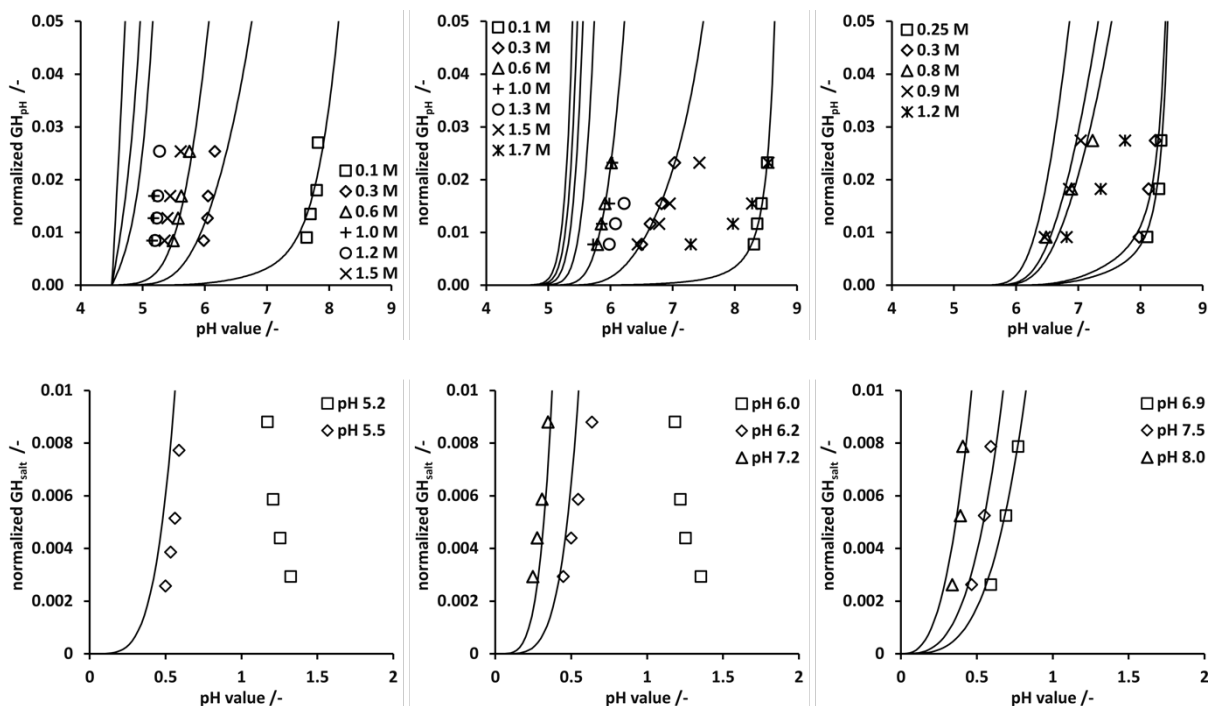


Figure 4: Result of curve fitting the standard SD model to the datapoints acquired from mixed-mode chromatography. pH gradients (top panels) and salt gradients (bottom panels) are shown for the acidic variant, neutral variant and basic variant from left to right respectively. pH gradient data can be modelled fairly, up to elevated salt concentrations. Salt gradient data is also described well, except for negative salt gradients starting at high salt conditions.

Analysis of the pH gradient data indicates that, for all variants, the elution pH value decreases with increasing salt concentration up to a certain point. Beyond this point, the retention and consequently the elution pH increase with further increases in salt concentration. This accurately reflects the U-shaped curve behaviour described earlier, but the data is viewed from a different dimension. Specifically, the U-shaped curves lay flat in an additional plane and are to be observed laterally. Their inflection points are located at the leftmost data points of the respective variant data. As for the salt gradient data, the datapoints can be categorized equally. No inflection in the retention is seen with increase or decrease in the tested pH range. It is important to note that the inverse salt gradient elution data points for GH values are presented as their negative values multiplied by -1, ensuring they appear on the positive scale. The calculated  $GH_{pH}$  and  $GH_{salt}$  curves are displayed in solid black lines. The curves shown in Figure 4 are calculated from the best modelling fit. When comparing the pH gradient datapoints to the modelled curves, the model accurately represents trends up to moderate salt concentration, which corresponds to the inflection point on the “U-shaped” curve for each variant. However, the classic SD model fails to account for the increase in retention observed with further increases in ionic strength. Regarding the

salt gradient data, the SD model effectively predicts trends up to moderately high salt concentrations and elevated pH values. Nevertheless, it falls short in scenarios involving high salt concentrations during reverse salt gradient elution experiments, where it is not able to describe anything.

### 3.1.2.2 Mechanistic modelling using a mixed-mode model including different activity coefficients

#### 3.1.2.2.1 Mixed-mode model with simple activity coefficient

Figure 5 presents the fitting results obtained using the mixed-mode model with the simplest activity coefficient formulation (Eq. 19). The final fitted model parameters are summarized in Table 8.

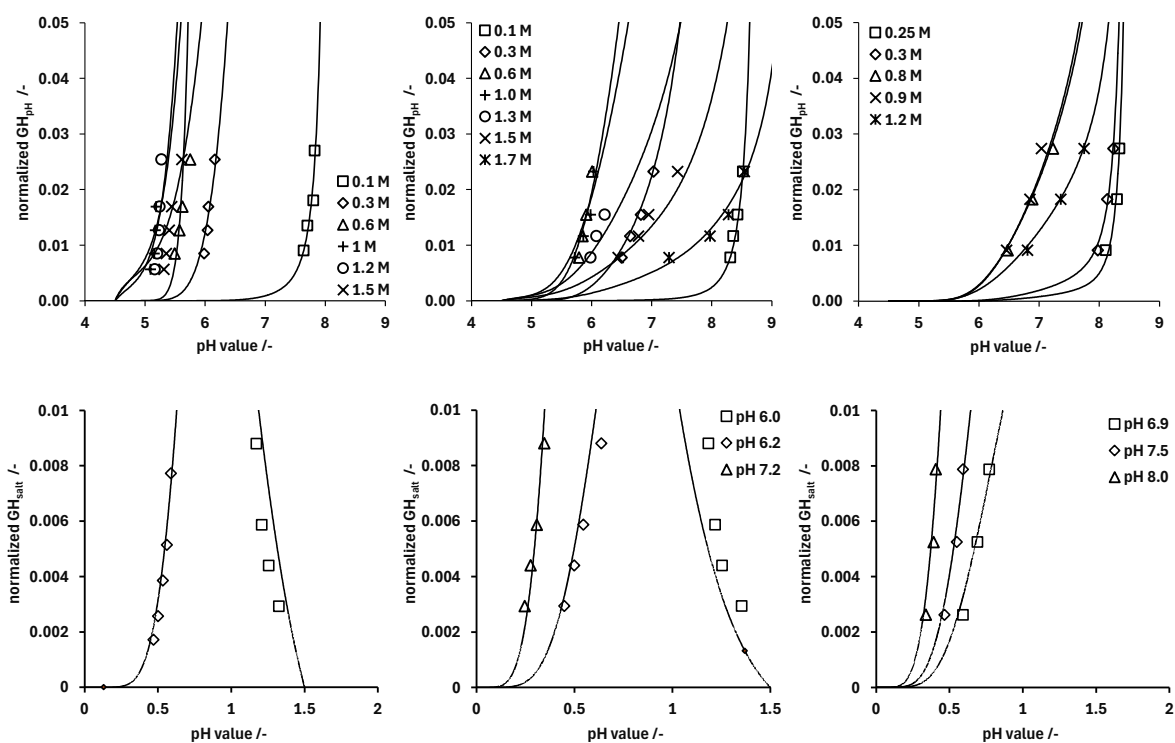


Figure 5: Result of curve fitting the mixed-mode model incorporating a simple activity coefficient to the acquired datapoints. pH gradients (top panels) and salt gradients (bottom panels) are shown for the acidic variant, neutral variant and basic variant from left to right respectively. pH gradient data as well as salt gradient data can be described exceptionally well up to high salt concentrations as well as increasing and decreasing salt gradients.

While the overall agreement between the model and experimental data is significantly improved compared to the classic SD model, which lacks any representation of hydrophobic interactions, certain discrepancies remain. The calculated GH curves

generally follow the trends of the experimental data, but noticeable deviations are observed, particularly for the acidic and neutral variants. In contrast, the basic variant is described with high accuracy across the entire range of conditions.

The acidic variant, especially under high salt conditions in the pH gradient experiments, exhibits an unusual initial curve shape that deviates from the expected exponential trend. For the neutral variant, the fit is visually solid at low and high salt concentrations, yet discrepancies emerge around the inflection point of the U-shaped retention profile. Further, although the reverse salt gradient data of the neutral and acidic variant are not poorly aligned as seen in Figure 5, the model does not describe them well either. Both reverse gradients display a displacement in their respective calculated GH curves, with the acidic variant exhibiting a modest rightward shift, while the neutral variant shows a slight leftward shift. The quality of fit is assessed by the sum of squared errors, which for the best fit in this setup was  $9.65 \times 10^{-4}$  in total.

Table 8: Estimated model parameters from simple activity coefficient model

$\Delta G_s$	$\Delta G_p$	$N_{carb}$	$N_{His}$	$N_{Amine}$	$N_{Tyr}$	$N_{n-term}$	$K_s$
	24.90	12.19	0.76	18.69	47.30	0.02	9.42
3.47	18.80	9.85	0.00	14.95	7.09	0.86	8.63
	19.19	16.31	0.00	22.88	22.94	0.13	8.45

### 3.1.2.2.2 Insights into model parameter dynamics

During data modelling, hundreds to thousands of fits were executed using an automated MATLAB® script, leading to a significant variation and accumulation of fit parameters. Many fits, beginning at different initial positions, consistently reached the same local minima concerning their sum of least squares, displaying identical fitted parameters with the exception of  $\Delta \hat{G}_p^0$  and  $n$ . Closer observations revealed a constant product of these two parameters. A graphical correlation of  $\Delta \hat{G}_p^0$  and  $n$  across different fits at the same local minima revealed a clear linear relationship between these parameters, as illustrated in the Figure 6:

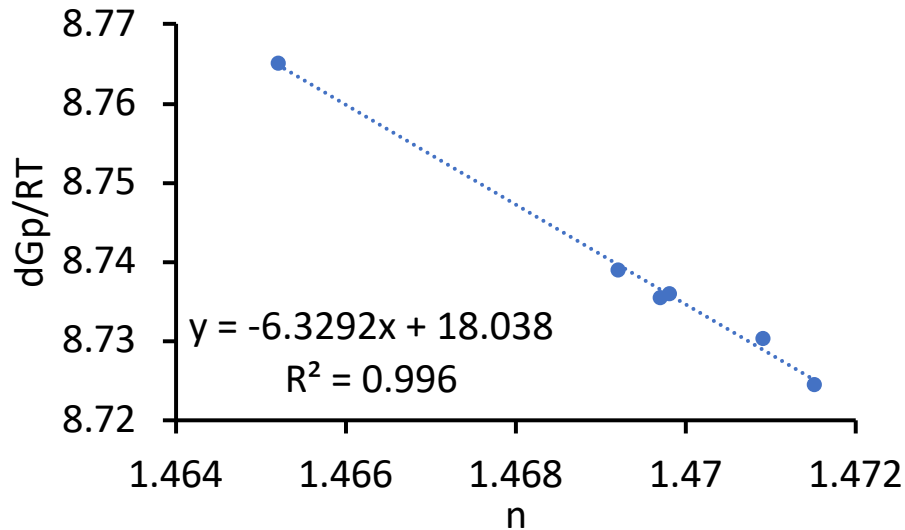


Figure 6: Correlation between the standard free Gibbs energy change on protein binding and the model parameter for the numbers of hydrophobic interactions at binding.

Upon further examination of the relevant equations, it became apparent that both  $\Delta\hat{G}_p^0$  and  $n$  should be constants under certain conditions. Notably, if no pH dependency for  $n$  is assumed and the mobile phase remains primarily aqueous without any polarity change, it is feasible to set  $n$  to zero. This adjustment effectively simplifies the hydrophobic interaction chromatography (HIC) component to unity. Implementing this change eliminates  $n$  from the equation, thereby reducing the number of fitting parameters. Consequently, any potential error arising from the removal of the HIC term will be compensated for by adjusting  $\Delta\hat{G}_p^0$ , the only other constant that is independent of both pH and salt concentration as shown in Eq. 26:

$$A_{MMC,i} = \left(\frac{\Lambda_{IEC}}{c_s z_s}\right)^{v_i(pH)} \exp\left(v(pH) \frac{\Delta G_s^0}{RT} - \frac{\Delta\hat{G}_i^{0*}}{RT}\right) \tilde{y}_i \quad (26)$$

With  $\Delta\hat{G}_i^{0*}$  being the lumped change of free Gibbs energy of the protein species  $i$ . This approach streamlines the model and enhances its applicability under the specified conditions.

### 3.1.2.2.3 Mixed-mode modelling using activity coefficient with both salt and pH dependency

Figure 7 presents the curve fitting results obtained using the mixed-mode model with a salt and pH-dependent activity coefficient, following the approach proposed by Lee et al.<sup>51</sup> The fitted model parameters are shown in Table 9.

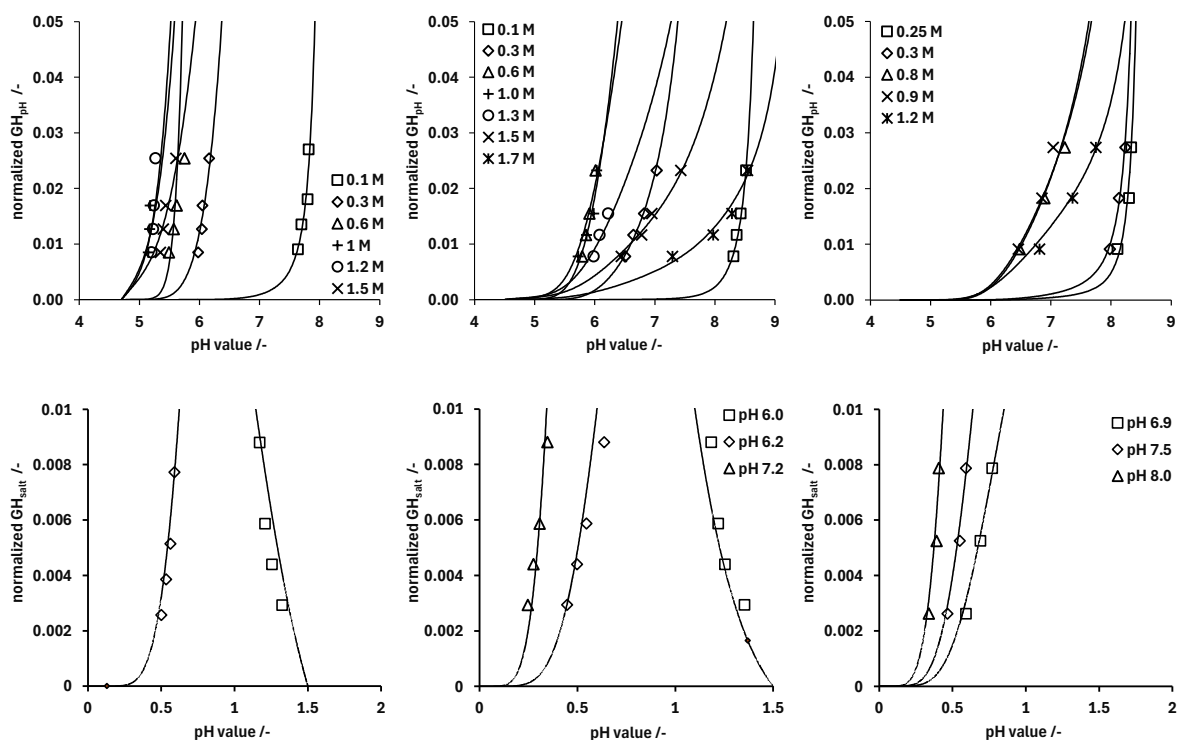


Figure 7: Result of curve fitting the mixed-mode model incorporating an activity coefficient proposed by Lee et al.<sup>51</sup> to the acquired datapoints. pH gradients (top panels) and salt gradients (bottom panels) are shown for the acidic variant, neutral variant and basic variant from left to right respectively. pH gradient data as well as salt gradient data can be described exceptionally well up to high salt concentrations as well as increasing and decreasing salt gradients.

Compared to the simpler formulation, this model shows a clear improvement in describing the experimental data, with a noticeably better overall fit and lower error values, where the total sum of squared errors is at  $5.60 \times 10^{-4}$ . In particular, the fit for the acidic and neutral variants is significantly enhanced, both in standard and reverse gradient modes. The GH curves now capture the transition region around the inflection point of the U-shaped profiles for the neutral variant and show improved agreement of data and modelled curves for the acidic variant. Even the reverse salt gradient data, which were previously insufficiently described, are now accurately reproduced.

Table 9: Estimated model parameters from salt and pH-dependent activity coefficient model

$\Delta G_s$	$\Delta G_p$	$N_{carb}$	$N_{His}$	$N_{Amine}$	$N_{Tyr}$	$N_{n-term}$	$\alpha$	$\beta$
	25.00	11.99	0.84	18.46	45.35	0.00	8.88	0.01
3.47	22.20	13.34	0.00	19.04	4.84	1.17	8.48	0.02
	22.65	20.23	0.00	27.41	17.88	0.66	6.88	0.05

### 3.1.2.2.4 Mixed-mode modelling using a complex activity coefficient

Figure 8 shows the curve fitting results using the mixed-mode model with a more complex activity coefficient that incorporates both salting-in and salting-out effects. The corresponding model parameters are listed in Table 10.

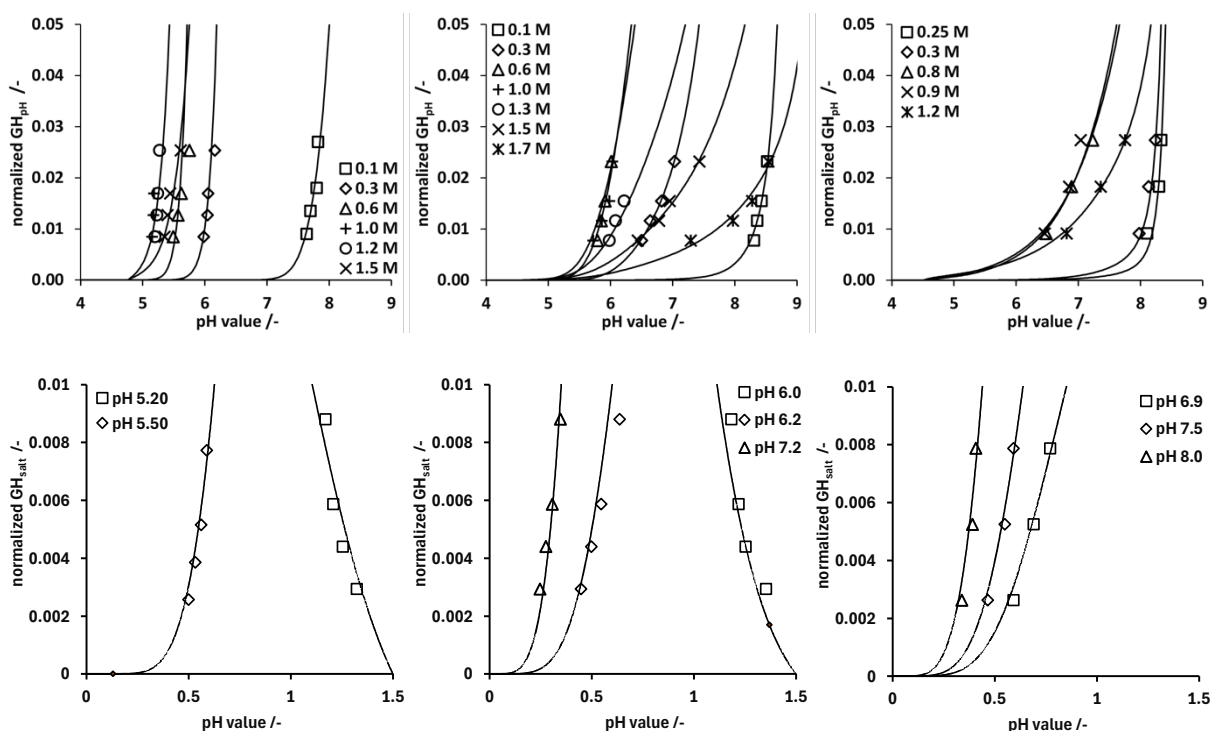


Figure 8: Result of curve fitting the extended mixed-mode model to the datapoints acquired from mixed-mode chromatography. pH gradient data can be modelled excellently up to very high salt concentrations for each variant. For salt gradient data, both gradients starting at low or high salt concentrations can be modelled very well.

The modelled GH curves provide an excellent match to the experimental data, with only minor deviations remaining. Compared to the previous models, the fit quality is further improved, as reflected by a lower overall error of  $5.33 \times 10^{-4}$ , compared to

$9.65 \times 10^{-4}$  and  $5.60 \times 10^{-4}$  for previous activity coefficient formulations. While the gain in accuracy is marginal, the curves visually describe the data better.

Table 10: Estimated model parameters from complex activity coefficient model

$\Delta G_s$	$\Delta G_p$	$N_{carb}$	$N_{His}$	$N_{Amine}$	$N_{Tyr}$	$N_{n-term}$	$\tau$	$\phi$	$\eta$
	14.39	12.30	0.21	16.96	56.57	0.00	3.64E-17	10.54	7.55E-11
<b>3.41</b>	10.02	12.07	0.00	15.46	6.43	0.74	3.44E-17	10.55	6.96E-11
	10.55	13.91	0.00	18.52	21.02	0.48	3.10E-17	11.38	7.53E-11

### 3.1.3 Understanding differences in activity coefficients

During the mechanistic modelling of protein retention on Eshmuno® CMX, three different formulations of the activity coefficient were introduced. Each of these extended the baseline model in order to better account for non-ideal solution behaviour and the interplay of electrostatic and hydrophobic interactions. To gain deeper insight, the activity coefficients were calculated using the model parameters determined in the previous chapters.

#### 3.1.3.1 Simple activity coefficient

Figure 9 illustrates the calculated activity coefficients for the three charge variants of mAb02 as a function of sodium ion concentration. Figure 9 (A) covers the full range from 0 to 1.5 mol L<sup>-1</sup> Na<sup>+</sup>, while Figure 9 (B) provides a zoomed-in view of the lower to medium concentration region, allowing subtle differences between the acidic, neutral, and basic variants to be distinguished more clearly.

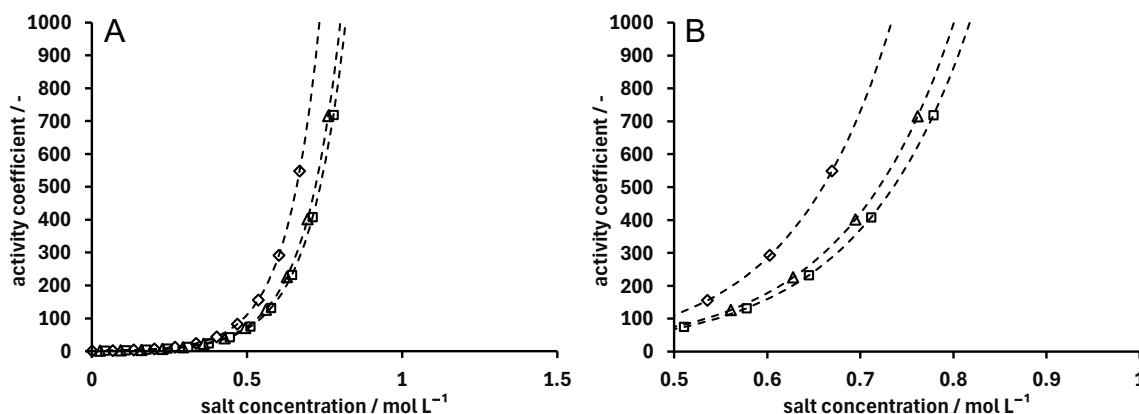


Figure 9: Activity coefficient as function of the salt concentration. Calculated from the simple activity coefficient as per Eq. 19. The acidic variant is represented by rhombi, the neutral variant by triangles and the basic variant by squares.

In all cases, the activity coefficients exhibit an exponential increase with rising salt concentration. All variants express highly similar activity coefficients. At low ionic strength, the coefficients remain close to unity, indicating only minor deviations from ideal behaviour. However, beyond approximately  $0.5 \text{ mol L}^{-1} \text{ Na}^+$  the values rise rapidly, and above  $0.8 \text{ mol L}^{-1}$  they exceed  $10^3$ .

The acidic, neutral, and basic variants exhibit minor differences at low to intermediate salt concentrations. Panel (B) indicates a slight deviation in their curves, with the activity coefficient of the acidic variant increasing earlier than those of the neutral and basic variants, which remain close even within the detailed range. The overall trend remains consistent among all three species.

### 3.1.3.2 pH and salt dependent activity coefficient

The second formulation of the activity coefficient builds directly on the simple exponential salt-dependent term by introducing an additional dependence on pH. This extension renders the model more flexible and better able to account for the dual influence of ionic strength and protein charge state on retention behavior. Importantly, the added pH dependency is empirical in nature and therefore primarily intended to improve the numerical fit, rather than to provide a direct mechanistic interpretation.

To visualize the combined effect of salt and pH, the calculated activity coefficients for the three charge variants were plotted in three dimensions, with salt concentration and pH on the x- and y-axes, respectively, and the activity coefficient ( $\gamma$ ) on the z-axis (Figure 10). This representation enables simultaneous assessment of both influences.

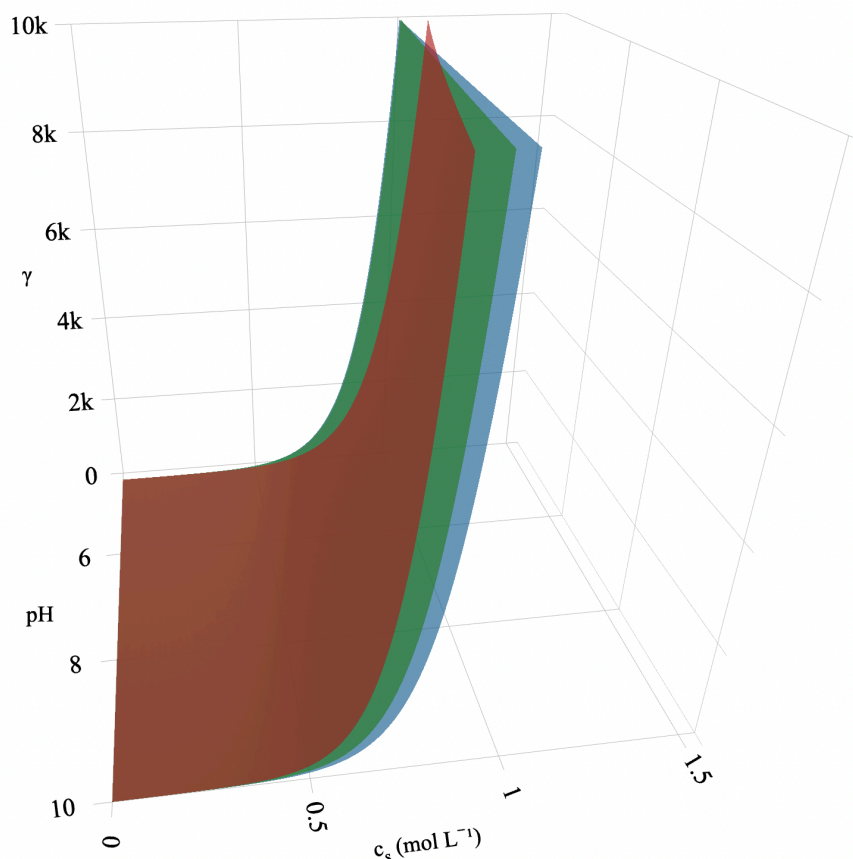


Figure 10: Activity coefficient as function of the salt concentration. Calculated from the pH and salt dependent activity coefficient as per Eq. 20. The acidic variant is represented by a red surface, the neutral variant by a green surface and the basic variant by a blue surface.

At very low salt concentrations, the activity coefficients remain close to unity, in line with the behavior already observed for the simple activity coefficient (exponential course). In this range, the effect of pH is minimal, and the surfaces for all three variants largely overlap. As the salt concentration increases, however, the activity coefficients rise exponentially, and the influence of pH becomes progressively more pronounced. Analogously to the simple activity coefficient, the values exceed  $10^3$  above  $0.8 \text{ mol L}^{-1} \text{ Na}^+$ .

In these higher ionic strength conditions, the surfaces corresponding to the acidic, neutral, and basic variants begin to diverge and partially overlap, creating an intertwined appearance in the 3D plot. Notably, the basic variant, which shows relatively lower activity coefficients at low pH values, overtakes the other two at higher pH, exhibiting the largest coefficients under these conditions. In contrast, the acidic

and neutral variants display broadly similar trends, particularly at lower pH values, but their behavior begins to differ at elevated pH. Here, the neutral variant shows an increase in activity coefficients that exceeds those of the basic variant, highlighting variant-specific differences that were not captured in the simpler model.

### 3.1.3.3 Complex activity coefficient

The third and most advanced formulation of the activity coefficient is based solely on salt concentration but incorporates both salting-in and salting-out effects. Unlike the simple exponential function, this description allows for a more nuanced representation of how increasing ionic strength influences protein-ligand interactions.

Figure 11 shows the calculated activity coefficients for the acidic, neutral, and basic variants across the tested salt concentration range.

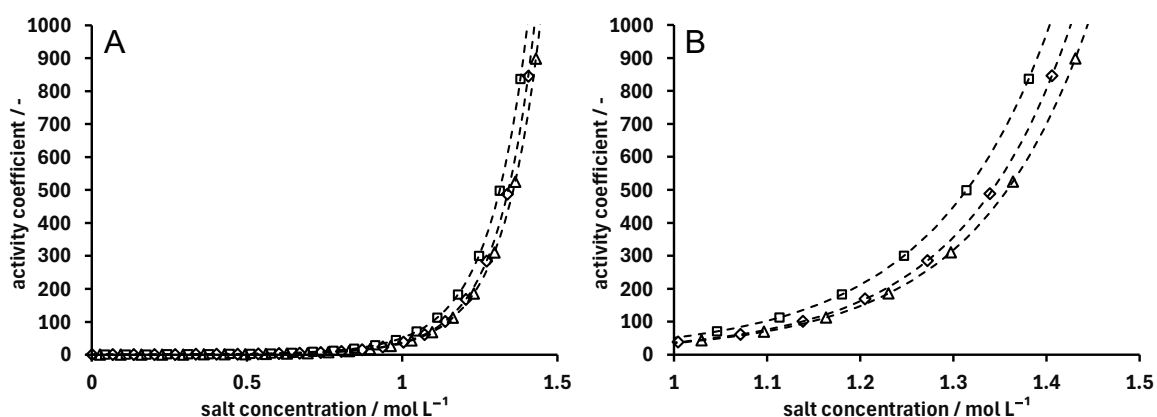


Figure 11: Activity coefficient as function of the salt concentration. Calculated from the complex activity coefficient as per Eq. 21. The acidic variant is represented by rhombi, the neutral variant by triangles and the basic variant by squares.

In contrast to both the simple salt-dependent model and the salt- and pH-dependent formulation described previously, the increase is not purely exponential across the entire range. Instead, the coefficients remain relatively modest at lower salt concentrations, with values below 100 up to approximately 1.1 mol L<sup>-1</sup> Na<sup>+</sup>. Beyond this point, the activity coefficients rise more steeply, exhibiting an exponential-like increase as the system enters the hydrophobic interaction regime. For high salt concentrations above 1.4 mol L<sup>-1</sup> Na<sup>+</sup>, the values rise above 10<sup>3</sup> as seen with the previous activity coefficients.

Another distinguishing feature of this formulation is the limited variation between the three charge variants. The corresponding curves are closely aligned, with only minimal differences across the entire salt concentration range.

### 3.1.4 Validation and simulation

Estimated model parameters were employed to conduct *in silico* chromatogram simulations using a lumped rate model, aiming to predict the elution profiles of proteins under various chromatographic conditions. For the simulations, the mixed-mode model using the complex activity coefficient was used.

#### 3.1.4.1 Prediction of pH gradient experiment from calibration data

The first simulation (Figure 12) serves as a validation of the model's correct calibration.

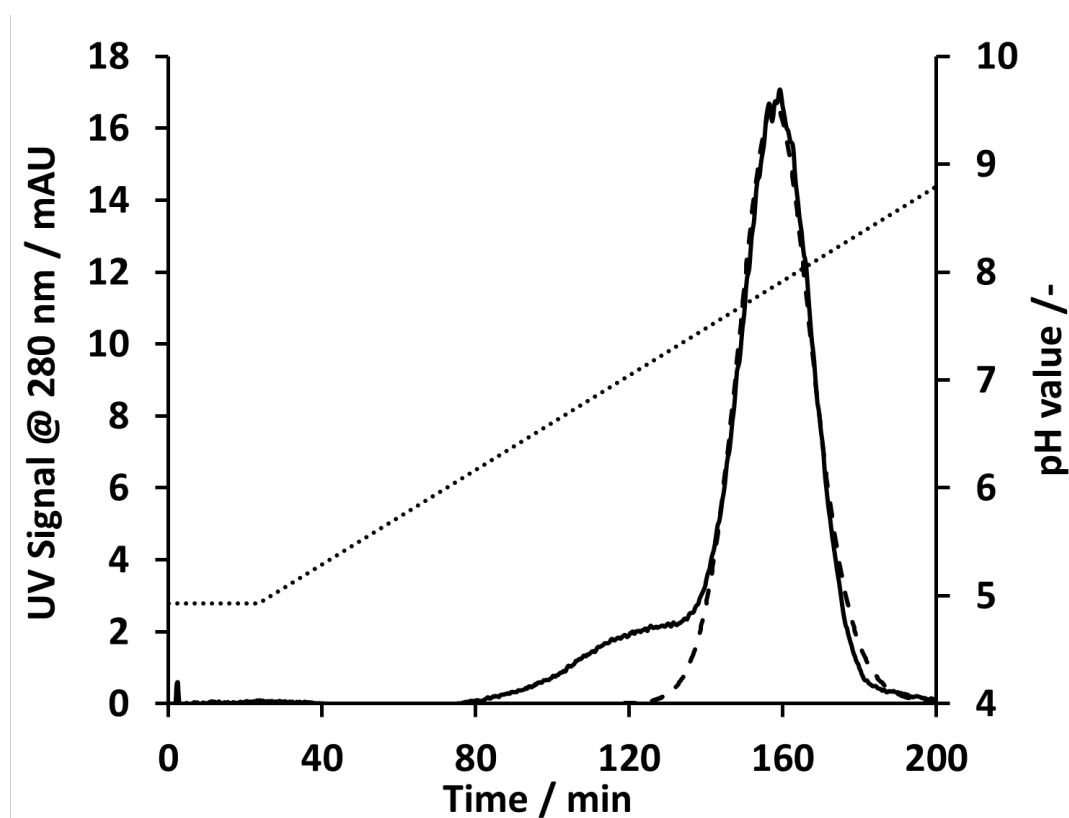


Figure 12: Comparison of simulated and experimental elution profile of a pH gradient elution experiment from pH 5 to pH 9 at  $0.15 \text{ mol L}^{-1} \text{ Na}_2\text{SO}_4$ . Gradient slope is 80 CV, flowrate set to  $0.65 \text{ mL min}^{-1}$  and sample load is  $1 \text{ mg mL}^{-1}$  neutral variant.

In this comparison of simulated and experimental elution profiles for a pH gradient elution experiment, the gradient ranged from pH 5 to pH 9 at a constant  $0.15 \text{ mol L}^{-1}$

sodium sulphate. The gradient slope was set to 80 column volumes, with a flowrate of  $0.65 \text{ mL min}^{-1}$  and a sample load of  $1 \text{ mg mL}^{-1}$  neutral variant. Experimental data used for model calibration was directly compared to the predicted chromatogram produced by the simulation. The alignment between the main peak in the experimental chromatogram and the simulated profile is remarkably close, with both peak position and retention time accurately predicted by the model. Nevertheless, a minor shoulder appears on the left side of the main peak in the experimental data, which is not reproduced by the simulation.

### 3.1.4.2 Prediction of reverse gradient elution

In the next experiment (Figure 13), a reverse salt gradient was applied.

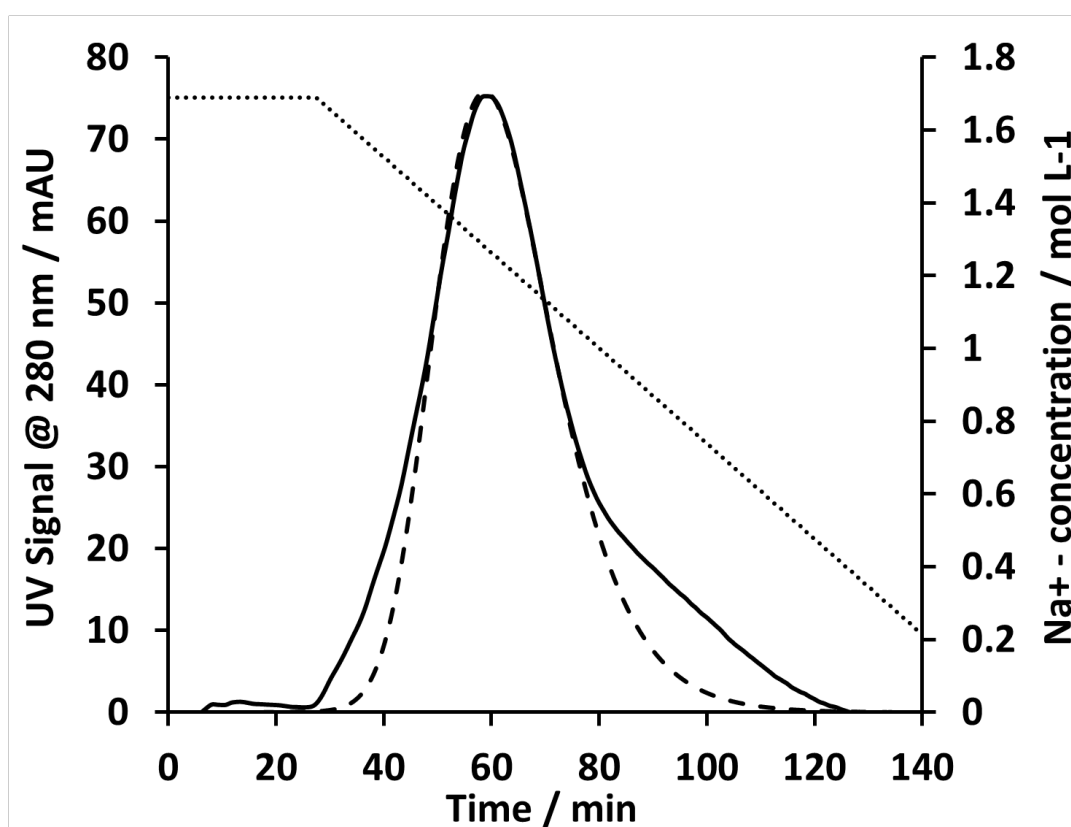


Figure 13: Comparison of simulated and experimental elution profile of a salt gradient elution experiment from  $0.85 \text{ mol L}^{-1} \text{ Na}_2\text{SO}_4$  to  $0.05 \text{ mol L}^{-1} \text{ Na}_2\text{SO}_4$  at pH 6. Gradient slope was 80 CV, flowrate was set to  $0.65 \text{ mL min}^{-1}$  and sample load was  $1 \text{ mg mL}^{-1}$  neutral variant.

The gradient transitioned from 0.85 M to 0.05 M sodium sulphate over 80 column volumes at pH 6. The flowrate was set to  $0.65 \text{ mL min}^{-1}$ , and the sample load was  $1 \text{ mg mL}^{-1}$  neutral variant. This example makes use of the hydrophobic part of the mixed-

mode material and binds the solute at remarkably high salt concentration. The experimental chromatogram, depicted as a solid black line and utilized for model calibration, was directly compared to the simulated profile, represented by a dashed black line.

The results demonstrated remarkable agreement between the simulation and the experimental data, particularly in the alignment of the main elution peak and its retention time. Notably, however, the simulation did not reproduce minor shoulders observed on the sides of the main peak in the experimental chromatogram. Nevertheless, the overall prediction quality remains high, showing the models applicability for reverse gradient elution.

### 3.1.4.3 Prediction of dual anti-parallel pH and salt gradient

A dual anti-parallel gradient elution experiment was simulated using the previously calibrated model and compared to experimental data (Figure 14).

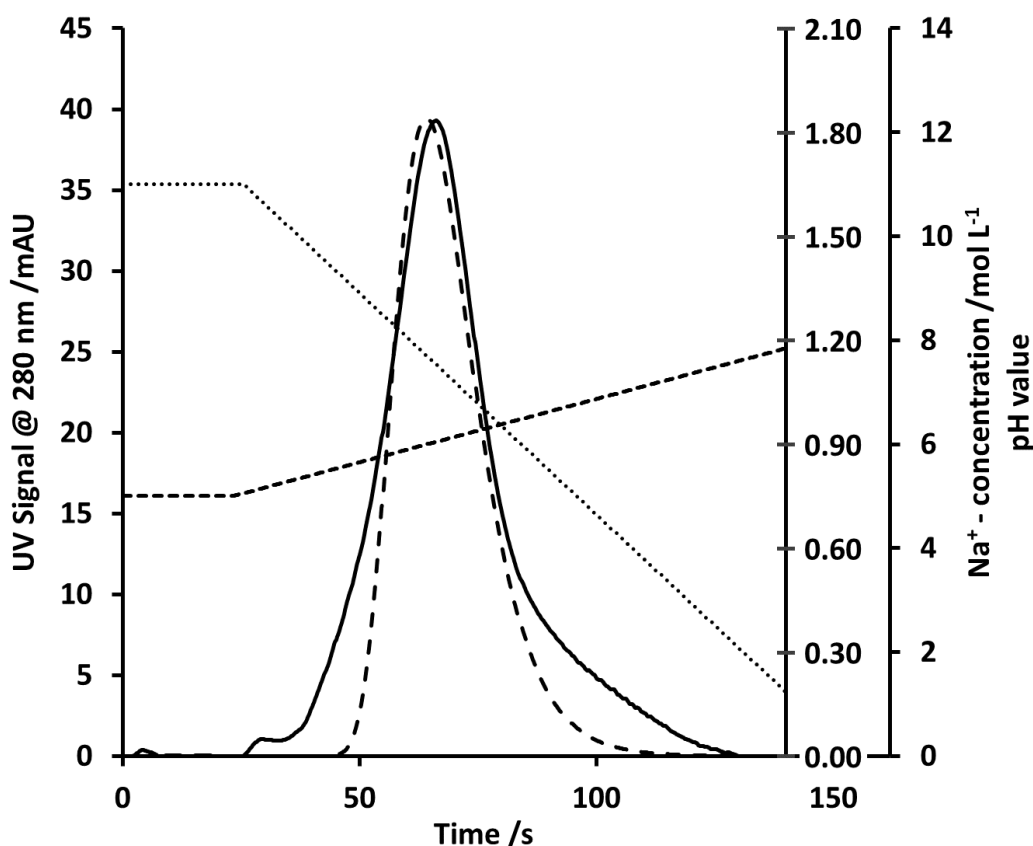


Figure 14: Comparison of simulated and experimental elution profile of a dual gradient elution experiment from  $0.85 \text{ mol L}^{-1} \text{ Na}_2\text{SO}_4$  to  $0.035 \text{ mol L}^{-1} \text{ Na}_2\text{SO}_4$  and from pH 5-8. Gradient slope was 50 CV, flowrate was set to  $0.65 \text{ mL min}^{-1}$  and sample load was  $1 \text{ mg mL}^{-1}$  neutral variant.

The gradient simultaneously ranged from 0.85 mol L<sup>-1</sup> to 0.035 mol L<sup>-1</sup> sodium sulphate and from pH 5 to pH 8 over 50 column volumes. A flowrate of 0.65 mL min<sup>-1</sup> and a sample load of 1 mg mL<sup>-1</sup> neutral variant were applied. The simulated elution profile is shown as a dashed black line, while the experimental chromatogram is represented by the solid black line.

The prediction aligns well with the experimental data, successfully capturing the overall retention behaviour and peak shape. A slight shift in retention volume is observed, with the simulated peak maximum appearing marginally earlier than its experimental counterpart. Further, this experimental data also exhibits shoulder as mentioned before. Notably, this simulation was performed without any dual-gradient experiments being used for model calibration, demonstrating the model's strong predictive power and robustness, even under complex, previously untested gradient conditions.

### 3.2 Modelling, simulation and scale up of Natrinx® CH mixed-mode membrane adsorber

Sections of this chapter have been published in Hedrich et al.<sup>153</sup>

#### 3.2.1 Comparison of ion exchange membrane with mixed-mode Natrinx® CH

Prior to initiating modelling work, the hydrophobic properties of the membrane were thoroughly assessed to ensure suitable performance in subsequent experiments. Consequently, preliminary binding and elution studies were carried out using the Natrinx® CH membrane in conjunction with a monoclonal antibody. Experimental work was carried out by Experiments were performed by Viktor Simaev (student research assistant). These initial experiments confirmed the membrane's efficacy in separating charge variants by employing a pH gradient at elevated salt concentrations, as illustrated in Figure 15.

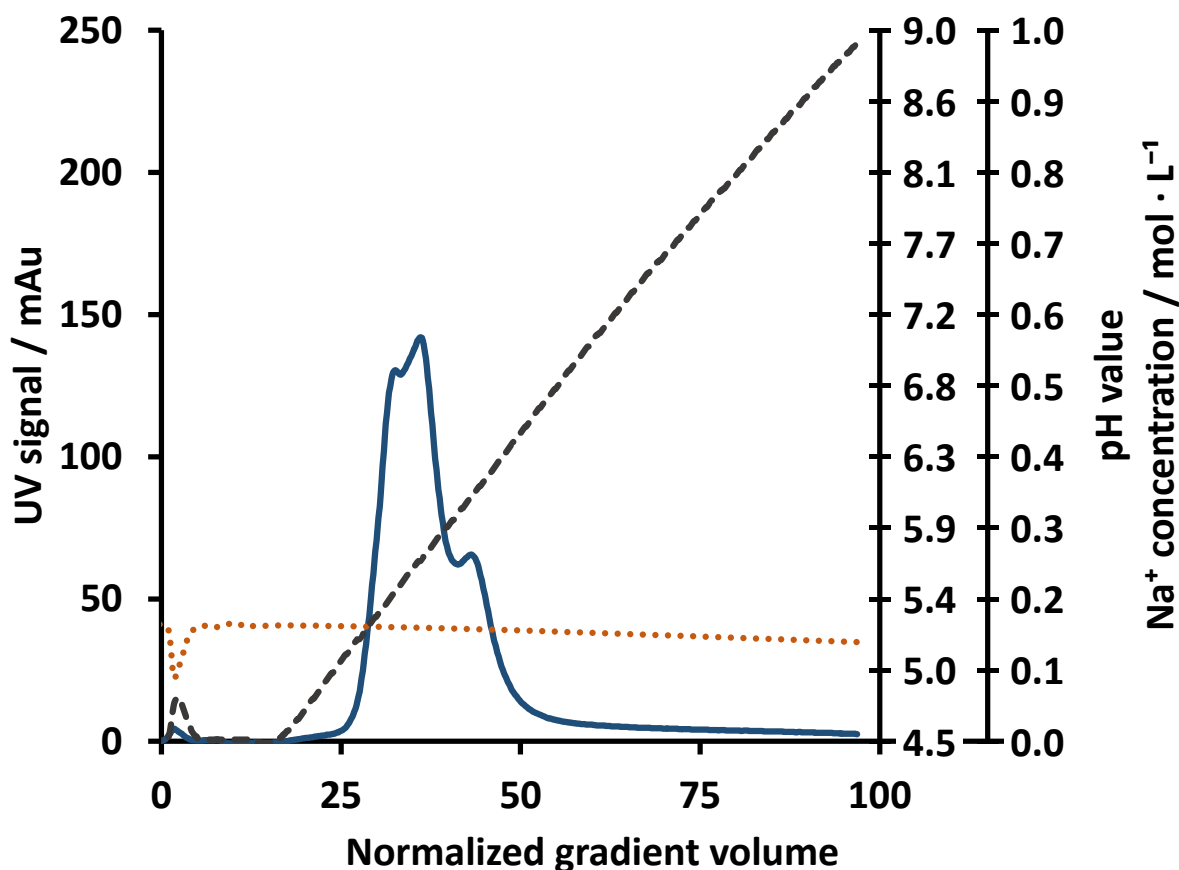


Figure 15: Chromatographic elution profiles of monoclonal antibodies (mAbs) on two membrane adsorbers under dual-gradient conditions. (A) Natrrix® CH: Elution profiles include UV signals (solid blue line), pH (black dotted line), and conductivity (orange dotted line), showing mAb elution (solid blue line) with starting separation of presumably a basic charge variant. (B) Cation-exchange membrane: Elution profiles under identical conditions, demonstrating earlier mAb elution. Gradients: pH 4.5 to pH 9 and sodium ion concentration  $0.1 \text{ mol L}^{-1}$  to  $0.08 \text{ mol L}^{-1}$ . Protein load was  $5 \text{ mg mL}^{-1}_{MV}$ . The enhanced retention in Natrrix® CH suggests the contribution of hydrophobic interactions, conferring greater tolerance to high salt concentrations.

The experimental setup featured a pH gradient ranging from pH 4.5 to 9 and a sodium chloride concentration of  $0.15 \text{ mol L}^{-1}$ , with a protein load maintained at  $5 \text{ mg mL}^{-1}_{MV}$ . To further examine whether this performance was unique to the Natrrix® CH membrane adsorber material, the same experimental conditions were applied to another commercially available pure ion-exchange adsorber membrane with similar characteristics.

The data of this comparative experiment are presented in Figure 16. When comparing these results with those obtained using the alternative ion-exchange membrane, it was observed that the Natrrix® CH membrane exhibited a delayed elution profile, indicating stronger overall retention of the monoclonal antibodies. As reflected in Figure 15, elution from the Natrrix® CH membrane occurred at intermediate pH values (ranging

from 5.2 to 6.3), whereas the comparative CEX membrane showed elution primarily in the pH region between 5 and 5.5 (see Figure 16).

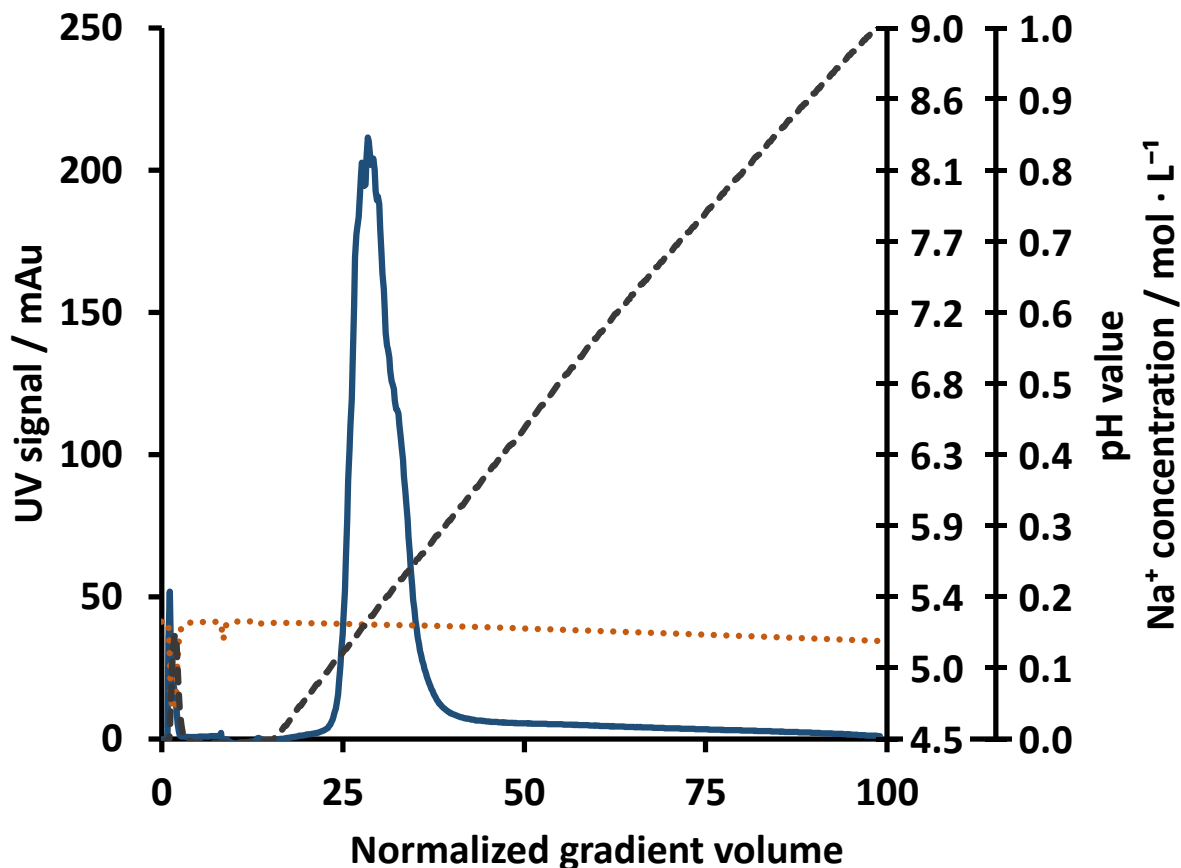


Figure 16: Chromatographic elution profiles of monoclonal antibodies (mAbs) on two membrane adsorbers under dual-gradient conditions. (A) Natrrix® CH: Elution profiles include UV signals (solid blue line), pH (black dotted line), and conductivity (orange dotted line), showing mAb elution (solid blue line) with starting separation of presumably a basic charge variant. (B) Cation-exchange membrane: Elution profiles under identical conditions, demonstrating earlier mAb elution. Gradients: pH 4.5 to pH 9 and sodium ion concentration 0.1 mol L<sup>-1</sup> to 0.08 mol L<sup>-1</sup>. Protein load was 5 mg mL<sup>-1</sup><sub>MV</sub>. The enhanced retention in Natrrix® CH suggests the contribution of hydrophobic interactions, conferring greater tolerance to high salt concentrations.

Notably, the Natrrix® CH membrane demonstrated distinctive elution behaviour, especially regarding the retention of the basic variant. While the acidic and neutral variants tended to elute under comparable conditions for both types of membranes, the basic variant displayed a noticeable delay in its elution when processed with the Natrrix® CH membrane.

Moreover, although the Natrrix® CH membrane seems capable of tolerating higher salt concentrations, it notably lacks the U-shaped retention pattern as has been observed with the mixed-mode Eshmuno® CMX material, which involve both ion exchange and

hydrophobic interactions. This absence of a U-shaped retention profile persisted even when sodium ion concentrations were increased beyond  $1 \text{ mol L}^{-1}$ .

### 3.2.2 Modelling of charge variant separation on Natrix® CH

A total of 96 linear gradient elution experiments were conducted as outlined in section 2.2.2.4.2. Experimental work was carried out by Alina Wulff.<sup>154</sup> The resulting chromatograms were processed and reduced to their primary characteristics, namely the normalized gradient slopes and corresponding elution conditions, i.e. either elution pH for pH gradients or elution salt concentration for salt gradients.

The experimental data were modelled, and model parameters were estimated by using a curve fitting procedure in MATLAB® as described before (chapter 2.2.2.5.2.1) using a stoichiometric ion-exchange model.

The final curve-fitting results are presented in Figure 17. The upper panel depicts the data of pH gradient conditions, and the lower panel of salt gradient conditions.

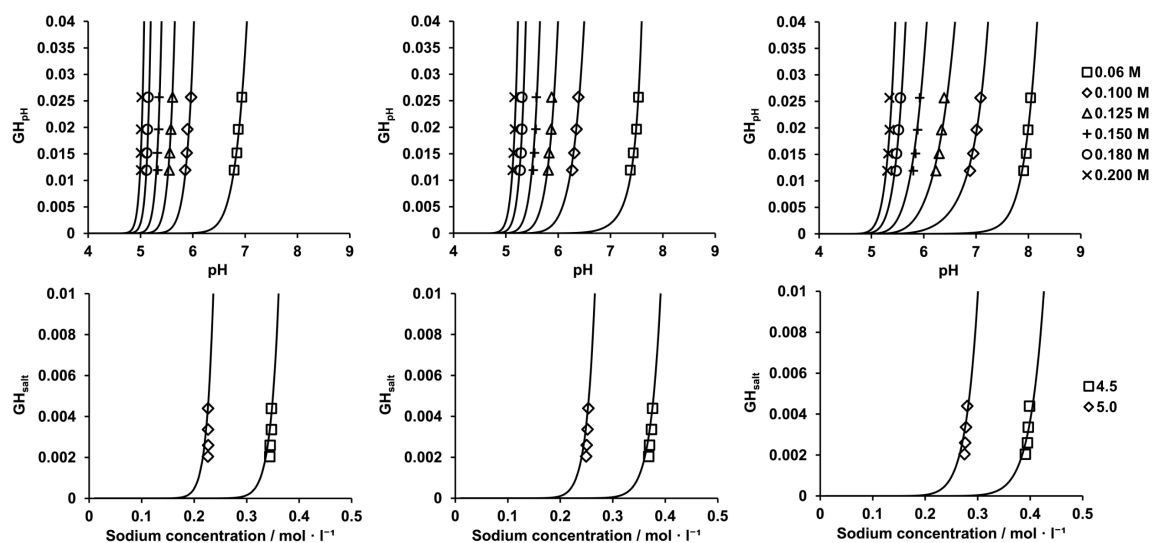


Figure 17: Curve fitting results of the standard SD model to experimental data from low-loading membrane chromatography. Results are presented for all three monoclonal antibody charge variants. From left to right are shown the acidic variant, neutral variant and basic variant respectively. The model demonstrates excellent agreement with the data for both pH gradients (top panels) and salt gradients (bottom panels).

Model accuracy was high across all variants and conditions, where the qualitative agreement between simulation and experiment was confirmed by the sum of squared

errors, with the best-fitting simulations exhibiting the lowest error values among all evaluated fits.

The fitted model parameters are provided in Table 11:

Table 11: Determined model parameters

mAb variant	$\frac{\Delta G_s^0}{RT}$	$\frac{\Delta G_i^0}{RT}$	$N_{Carb}$	$N_{Tyr}$	$N_{Amine}$	$N_{His}$	$N_{n-term}$
<b>Acidic</b>		29.13	16.12	97.96	23.57	1.11	2.02
<b>Neutral</b>	2.91	28.44	14.16	109.08	23.85	1.62	0
<b>Basic</b>		27.73	13.83	71.15	24.19	1.49	2.17

Most parameters show similar range of values, compared to the resin-based material. However, one exception was the estimated number of tyrosine side chains ( $N_{Tyr}$ ), which showed a notably high average value of 92.6. The counterion standard Gibbs free energy term ( $\frac{\Delta G_s^0}{RT}$ ) was fixed at 2.91 for all variants, as per model theory. The protein-specific Gibbs energy term ( $\frac{\Delta G_i^0}{RT}$ ) ranged between 27.57 and 29.13.

Despite the mixed-mode character of the Natrix® CH membrane, the model was successfully calibrated and applied to the dataset.

Figure 18 shows the calculated characteristic charge-pH profiles of the mAb charge variants, calculated from the fitted model parameters.

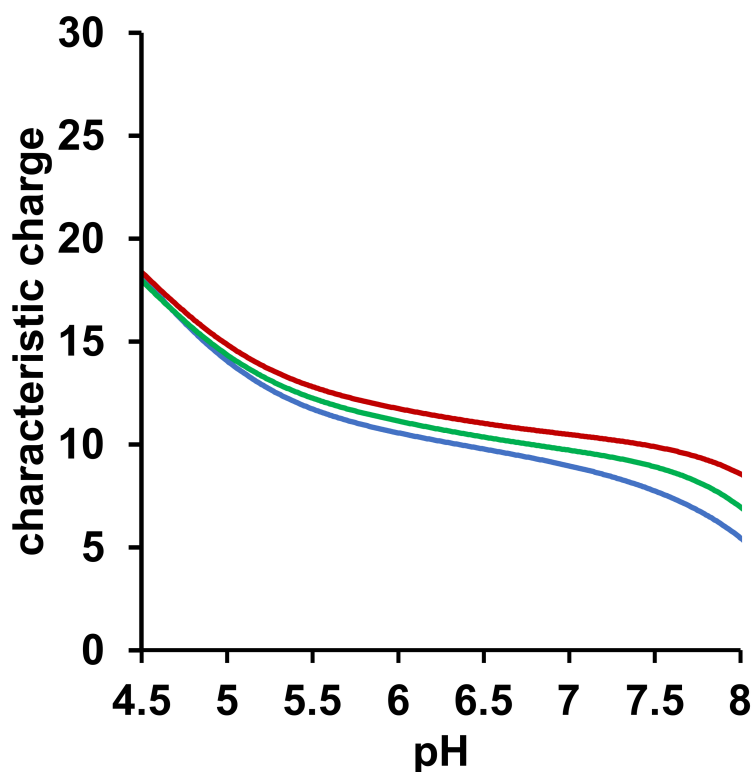


Figure 18: Characteristic charge profiles of mAb charge variants for acidic (red), neutral (green) and basic (red) variant.

The curves represent the predicted characteristic charge across a pH range from 4.5 to 8.0, corresponding to the calibrated range used during modelling. The acidic variant is depicted as a blue solid line, the neutral variant as a green solid line, and the basic variant as a red solid line.

At pH 4.5, all three variants exhibit similar charges, with characteristic charge values close to 18. As pH increases, each variant shows a progressive decrease in charge, following a titration-like profile. By pH 8, the net charge values span a range from approximately 5.5 to 8.6.

The extent of charge reduction differs among the variants: the acidic variant undergoes the largest decrease, the neutral variant shows an intermediate drop, and the basic variant retains the highest charge throughout the pH range. Additionally, the slope of the curves becomes slightly steeper at higher pH values, indicating more pronounced deprotonation near the upper limit of the range.

### 3.2.3 Validation of model calibration by optimization of separation

Since the experimental data could initially be described using a simplified ion-exchange model, the next objective was to explore how far this approach could be taken before reaching its limitations, while also gaining deeper insight into the contribution of the material's mixed-mode character, ultimately aiming to better understand its physicochemical behaviour in charge variant separation of mAbs.

To validate the estimated model parameters, an *in silico* optimization of charge variant separation was performed using Berkeley Madonna. Chromatograms were simulated using the models discussed in chapter 1.4.1 incorporating the previously calibrated model (chapter 3.2.2). Numerous combinations of gradient slopes and process conditions were simulated, systematically exploring a wide parameter space to identify optimal separation conditions.

The most effective strategy predicted by the model was an anti-parallel dual gradient elution, ranging from pH 5 to pH 8 and 0.1 mol L<sup>-1</sup> to 0.08 mol L<sup>-1</sup> sodium chloride, over a gradient volume of 235 membrane volumes (MV). The sample load was set to 1 mg mL<sup>-1</sup><sub>MV</sub>, and a flow rate of 10 mL min<sup>-1</sup> was used in both the simulation and subsequent experimental validation. Experimental work was carried out by Rita Steigmiller.<sup>149</sup>

As illustrated in Figure 19, the simulation (solid lines) predicted a clear separation between the acidic and neutral variants and nearly baseline resolution for the basic variant. Experimental validation of this optimized condition showed a strong agreement with the model. Visually comparing, the experimental elution profiles (dashed lines) closely matched the simulated curves across all major peaks.

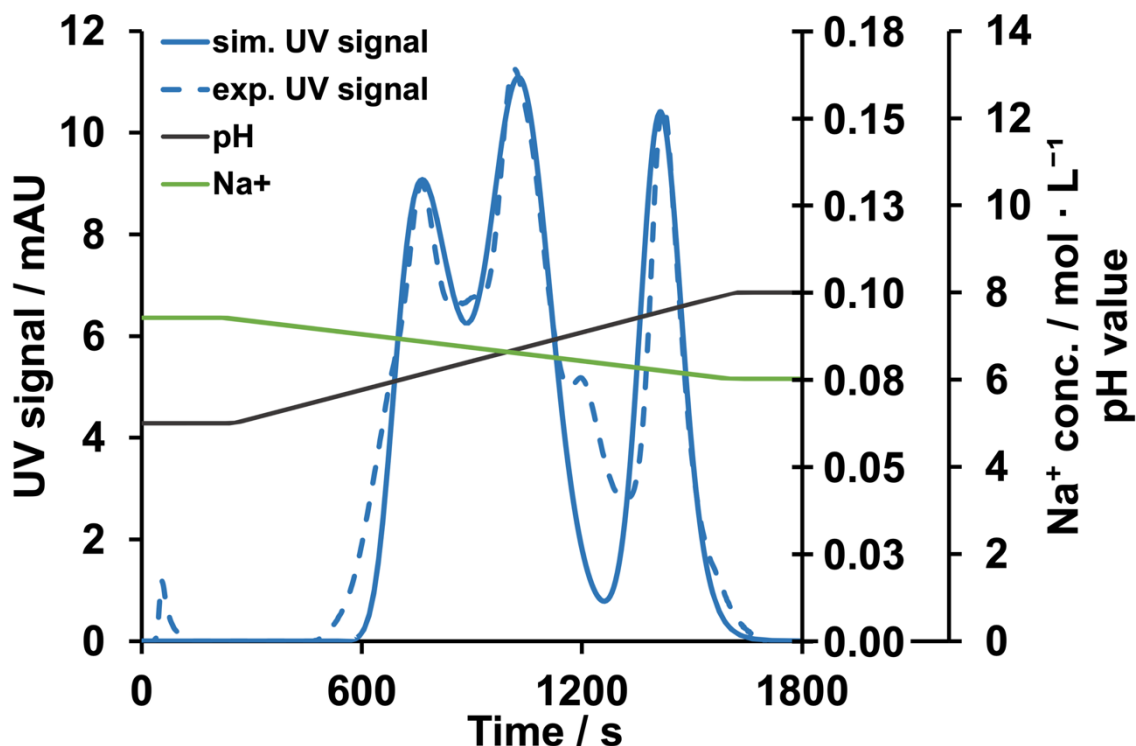


Figure 19: Validation of model parameters through *in silico* simulations for optimizing the separation of charge variants using an antiparallel dual pH and salt gradient. Gradient volume 235 MV, sodium ion concentration  $0.1 \text{ mol L}^{-1}$  to  $0.08 \text{ mol L}^{-1}$  and pH 5 to pH 8. Sample load:  $1 \text{ mg mL}^{-1}_{MV}$ . Flow rate:  $10 \text{ mL min}^{-1}$ . Experimental results (dashed lines) closely align with simulated elution profiles (solid lines), confirming the model's predictive accuracy.

One notable difference was the appearance of an additional, previously unmodeled variant between the neutral and basic peaks in the experimental data. This peak was not predicted by the simulation and leads to a discrepancy around 1200 s.

### 3.2.4 Scale up of mAb charge variant separation

Since the model performed good in a low loading environment, the aim further shifted towards its capability at higher loads. Therefore, the model was applied in a scale up study. The scale up was done from a 1.06 mL membrane device to an 8.8 mL membrane cassette. Before that, the upscaled membrane had to be assessed and the model had to be extended.

#### 3.2.4.1 Binding capacity

Dynamic binding capacity (DBC) measurements were conducted at pH 5 and  $0.03 \text{ mol L}^{-1}$  sodium chloride to assess the performance of the two membrane formats: a 1.06 mL membrane device and an 8.8 mL cassette. Experiments were performed at a flow rate of  $1 \text{ MV min}^{-1}$ , and DBC values were determined at 10 % breakthrough

(DBC<sub>10 %</sub>) and 95 % breakthrough (DBC<sub>95 %</sub>). Experiments were performed by Viktor Simaev (student research assistant).

The 1.06 mL membrane exhibited a DBC<sub>10 %</sub> of 124 mg mL<sup>-1</sup><sub>MV</sub> and a DBC<sub>95 %</sub> of 350 mg mL<sup>-1</sup><sub>MV</sub>. The 8.8 mL cassette showed an identical DBC<sub>10 %</sub> of 124 mg mL<sup>-1</sup><sub>MV</sub>, but a DBC<sub>95 %</sub> of 317 mg mL<sup>-1</sup><sub>MV</sub>. Although the early breakthrough capacities were equivalent, the smaller membrane showed a 10 % higher DBC<sub>95 %</sub>.

At a residence time of 2.1 minutes, corresponding to 1 MV min<sup>-1</sup>, both membrane formats demonstrated equivalent DBC<sub>10 %</sub> values.

The impact of flow rate on dynamic capacity was also evaluated for the 1.06 mL membrane at an increased flow rate of 10 MV min<sup>-1</sup> (residence time: 0.3 minutes). Under these conditions, DBC<sub>10 %</sub> decreased slightly to 116 mg mL<sup>-1</sup><sub>MV</sub>, and DBC<sub>95 %</sub> to 292 mg mL<sup>-1</sup><sub>MV</sub>, representing reductions of 7 % and 17 %, respectively. In comparison, resin-based adsorbers under similar high-flow conditions typically show capacity losses of up to 50 %. This performance stability under elevated flow conditions supports a substantial increase in process productivity. Calculated productivity rose from 285 g L<sup>-1</sup>h<sup>-1</sup> at 1 MV min<sup>-1</sup> to 2854 g L<sup>-1</sup>h<sup>-1</sup> at 10 MV min<sup>-1</sup>, representing a ten-fold increase in throughput with only minimal compromise in binding capacity.

#### 3.2.4.2 Estimation of shielding factors

The existing model (chapter 3.2.2) had previously been calibrated only within the linear range of the adsorption isotherm, limiting its use to low-concentration conditions. To extend the mechanistic model to high protein loading conditions, the Steric Mass Action (SMA) model was introduced. The SMA framework, widely used in ion-exchange chromatography, expands upon the conventional stoichiometric displacement model by incorporating a steric hindrance coefficient, or shielding factor, which accounts for the reduction in available binding sites as protein loading increases.

To enable accurate simulations under high loading, additional experiments were performed with elevated monoclonal antibody concentrations, involving sample binding at various pH values and subsequent salt gradient elution. Experimental work was carried out by Alina Wulff.<sup>154</sup>

The resulting high-load chromatograms were used for reverse parameter estimation (chapter 2.2.2.5.2.2), allowing the shielding factor to be extracted and incorporated into

the SMA model. This extension enabled the model to simulate and predict protein retention behaviour under non-linear, high-loading conditions.

Figure 20 presents the elution profiles of monoclonal antibody (mAb) charge variants under conditions of increasing sample load, using salt gradient elution at constant pH.

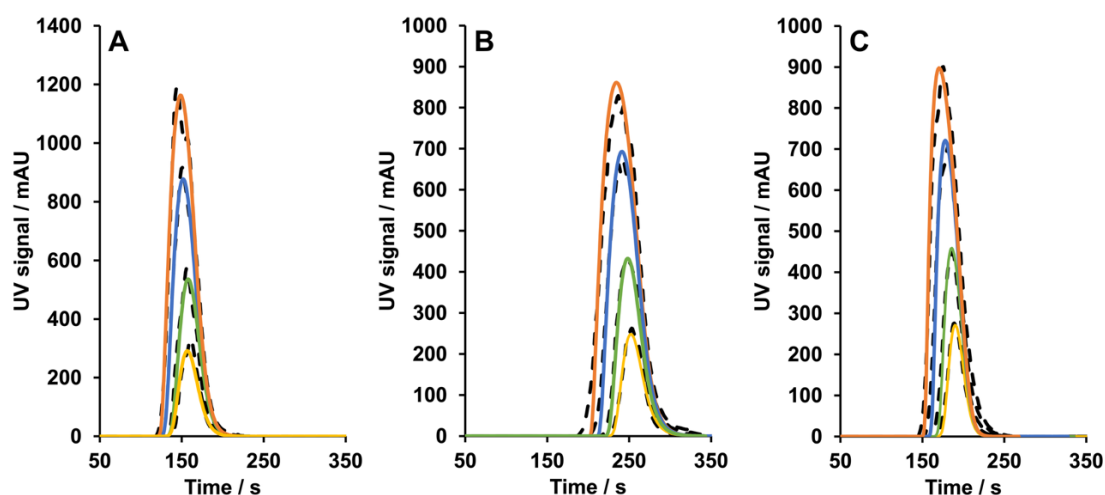


Figure 20: Reverse fitting chromatograms to estimate shielding factors for each monoclonal antibody variant under a specific condition. Each graph illustrates the experimental data (dashed lines) and simulated curves (solid lines) for sample load between  $5.75 \text{ mg mL}^{-1}_{MV}$  and  $35 \text{ mg mL}^{-1}_{MV}$ . Experimental data was acquired through salt gradient elution. Gradient volume  $85 \text{ MV}$ , sodium ion concentration  $0.03 \text{ mol L}^{-1}$  to  $0.8 \text{ mol L}^{-1}$  and pH 4.5, 5.0, 5.5. Flow rate:  $10 \text{ mL min}^{-1}$ .

Across all loading levels, the variants eluted at approximately the same salt concentration. However, a slight forward shift in peak positions was observed with increasing load, reflecting earlier elution. In addition, peak tailing became more pronounced for all charge variants as the sample load increased.

The high-loading experimental data were used to estimate shielding factors for each monoclonal antibody charge variant across the several pH values. These factors were obtained through in silico reverse fitting, using the extended Steric Mass Action (SMA) model. For each charge variant and pH condition, a single shielding factor was determined, which was used to describe all loading conditions for that combination. This approach ensured that the shielding factor captured the non-linear binding behaviour consistently across the full range of protein loads, up to  $35 \text{ mg mL}^{-1}$ .

The derived values are summarized in Table 12. The predicted chromatograms from the reverse gradients based on these shielding factors closely reproduced the experimental elution profiles, as shown in Figure 20, demonstrating a high level of

agreement. Although the overall match between simulations and experiments was strong, small deviations in the peak tops were noted.

Table 12: Shielding factors estimated from reverse fitting procedures.

pH value	Acidic variant	Neutral variant	Basic variant
4.5	85	65	41
5.0	108	66	44
5.5	118	69	44
6.0	123	71	43

The shielding factors exhibited a clear dependency on pH. At pH 4.5, values ranged from 85 for the acidic variant, to 65 for the neutral, and 41 for the basic variant. As pH increased, shielding factors also increased, particularly for the acidic variant. At pH 5.0 and 5.5, values rose to 108 and 118 for the acidic variant, while the neutral variant increased more modestly to 66 and 69, and the basic variant remained relatively unchanged at 44. This trend continued at pH 6.0, where the acidic variant reached 123, and only minor increases were seen for the neutral (71) and basic (43) variants.

These results show that shielding increases with pH, especially for the acidic variant. Additionally, at each pH, the shielding factor consistently decreased from the acidic to the basic variant.

To validate the extended SMA model under high protein loading conditions, *in silico* simulations were performed using the newly estimated shielding factors for a simple salt gradient at pH 5.5 and a protein load of 23 mg mL<sup>-1</sup><sub>MV</sub>. The simulated conditions matched the experimental setup, which used the full monoclonal antibody (mAb) sample and employed a gradient volume of 85 membrane volumes (MV), with sodium ion concentration ranging from 0.03 mol L<sup>-1</sup> to 0.8 mol L<sup>-1</sup>, and a flow rate of 10 mL min<sup>-1</sup>.

The experimental elution profile was compared with the simulation, and the distribution of charge variants was determined through analytical cation exchange chromatography (IEX-HPLC). As expected for a simple salt gradient, no baseline

separation of the variants was achieved. However, the comparison between simulated and experimental elution profiles, shown in Figure 21, revealed excellent alignment.

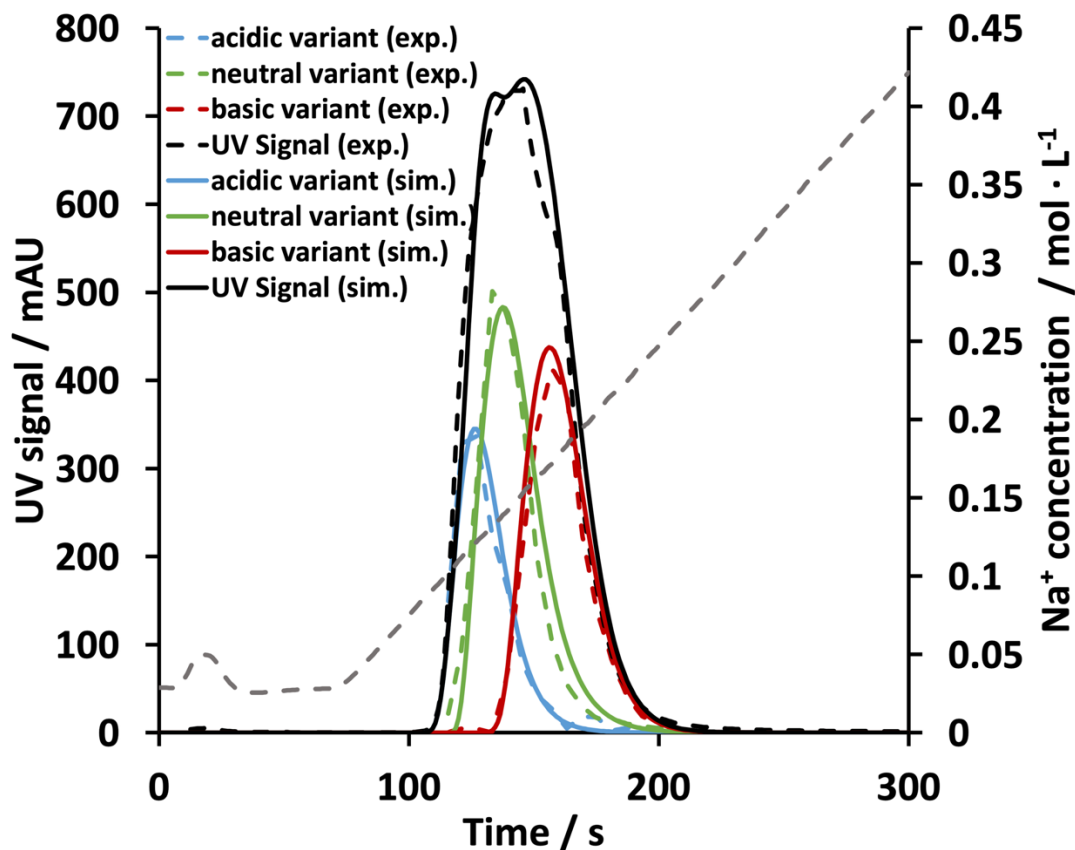


Figure 21: Validation of model parameters for high-loading chromatography runs, incorporating shielding factor data into *in silico* simulations. Gradient volume 85 MV, sodium ion concentration  $0.03 \text{ mol L}^{-1}$  to  $0.8 \text{ mol L}^{-1}$  and pH 5.5. Sample load:  $23 \text{ mg mL}^{-1}$ . Flow rate:  $10 \text{ mL min}^{-1}$ . The graph compares experimental elution profiles of the full monoclonal antibody (black dashed line) with simulated data (black solid line), showing excellent alignment. Individual variants, acidic (blue), neutral (green), and basic (red), were identified using analytical cation exchange chromatography and are accurately predicted by the simulation.

The experimental profile of the full mAb is represented by a black dashed line, while the simulation is shown as a black solid line. The simulation also resolved the individual charge variants: acidic (blue), neutral (green), and basic (red). All major features of the elution profile were well captured by the model, confirming its ability to accurately predict retention behaviour under high-loading conditions using a single shielding factor per variant and pH.

### 3.2.4.3 Scale up of charge variant separation using mechanistic modelling

To evaluate the scalability of the mechanistic model, a scale-up experiment was conducted using an 8.8 mL bench-scale membrane device packed with the same Matrix® CH material as used in the lab-scale device. The first goal was to verify consistency in separation performance under identical optimized conditions, previously determined through modelling, by using an anti-parallel dual gradient from pH 5 to pH 8 and 0.1 mol L<sup>-1</sup> to 0.08 mol L<sup>-1</sup> sodium chloride. Experiments were carried out by Rita Steigmiller.<sup>149</sup>

The resulting elution profiles, presented in Figure 22, showed a high degree of similarity between the bench-scale and the lab-scale device. Elution volumes were nearly identical when normalized to gradient volume, confirming consistency in separation behaviour. Minor deviations were observed in the peak maxima of the neutral and basic variant, which are shifted slightly between the different elution profiles.

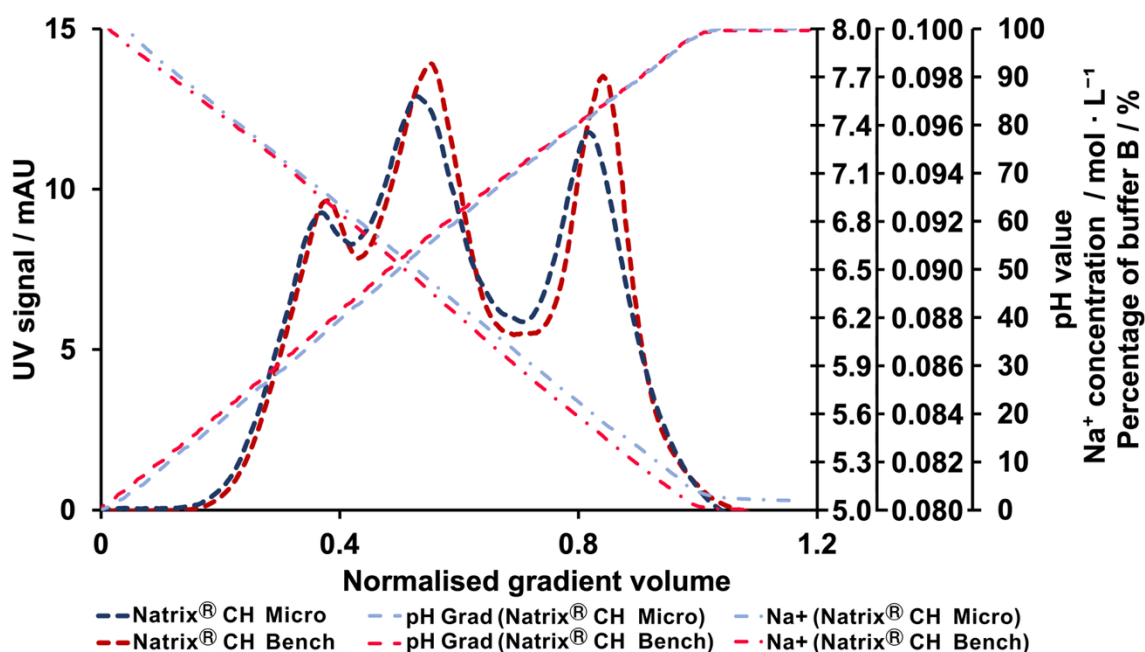


Figure 22: Comparison of elution profiles for monoclonal antibodies (mAbs) on 1.06 mL and 8.8 mL Matrix® CH membrane devices under dual-gradient conditions. Gradient volume 45 MV, sodium ion concentration 0.1 mol L<sup>-1</sup> to 0.08 mol L<sup>-1</sup> and pH 5 to pH 8. Sample load: 1 mg mL<sup>-1</sup><sub>MV</sub>. Flow rate: 15 mL min<sup>-1</sup>. The profiles demonstrate high similarity, with nearly identical elution volumes when normalized to gradient volume. Minor discrepancies are attributed to slight variations in pH, sodium ion concentration, or device geometries.

To further evaluate process scalability and throughput potential, the bench-scale membrane device was operated across a wide range of flow rates, from 30 mL min<sup>-1</sup>

up to  $240 \text{ mL min}^{-1}$ , which exceeds the manufacturer's recommendation by factor 2.7. The separation was performed under gradient elution with a gradient volume of 185 MV, sodium ion concentration from  $0.0375 \text{ mol L}^{-1}$  to  $0.5 \text{ mol L}^{-1}$ , and pH 6, with a sample load of  $1 \text{ mg mL}^{-1}\text{MV}$ . Experiments were performed by Rita Steigmiller.<sup>149</sup>

As shown in Figure 23A, the elution profiles remained highly consistent across all flow rates. Figure 23B presents the same data shown by process time consumption, highlighting the significant reduction in total separation time as flow rate increased.

This allows for significant time-saving advantages in process development and manufacturing.

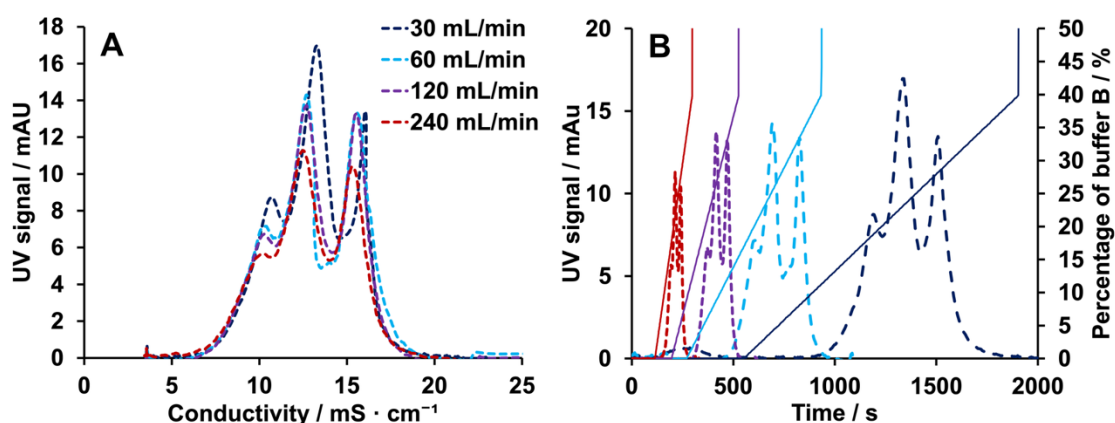


Figure 23: Elution profiles of monoclonal antibodies (mAbs) at varying flow rates ( $30 \text{ mL min}^{-1}$  to  $240 \text{ mL min}^{-1}$ ) displayed as UV absorbance versus conductivity (A) and as a function of process time (B) and. Gradient volume 185 MV, sodium ion concentration  $0.0375 \text{ mol L}^{-1}$  to  $0.5 \text{ mol L}^{-1}$  and pH 6. Sample load:  $1 \text{ mg mL}^{-1}\text{MV}$ . Flow rate:  $30 \text{ mL min}^{-1}$  to  $240 \text{ mL min}^{-1}$ . (A) highlights the substantial reduction in process time achievable with higher flow rates while maintaining consistent separation quality. The normalization in (B) diminishes discrepancies arising from gradient irregularities, particularly at lower flow rates. The profiles remain consistent across flow rates.

After confirming consistency between lab-scale and bench-scale Matrix® CH membrane devices, the calibrated model was applied to test its applicability in this up-scale environment and to validate its predictive capability under high-loading conditions. A salt gradient elution experiment was simulated using the 8.8 mL bench-scale membrane. The simulation was based on an 85 CV sodium chloride gradient ranging from  $0.015 \text{ mol L}^{-1}$  to  $0.3 \text{ mol L}^{-1}$  at a constant pH of 6, using a sample load of  $30 \text{ mg mL}^{-1}\text{MV}$  and a flow rate of  $10 \text{ mL min}^{-1}$ . The shielding factors used for the high-loading simulation were those previously estimated and summarized in Table 12.

The simulation predicted a partial resolution of the charge variants, particularly a slight separation of the basic variant from the others. This prediction was then experimentally validated under identical conditions.

As shown in Figure 24, the experimental elution profile (black dashed line) closely matches the simulated profile (black solid line), confirming the model's predictive accuracy. The charge variants were further identified using analytical cation exchange chromatography (IEX-HPLC), allowing the individual charge variants, acidic (blue), neutral (green), and basic (red), to be resolved and compared with the simulation.

As predicted, the variants eluted within the sodium chloride concentration range of  $0.075 \text{ mol L}^{-1}$  to  $0.18 \text{ mol L}^{-1}$ , with the acidic variant eluting first, followed by the neutral and then the basic variant.

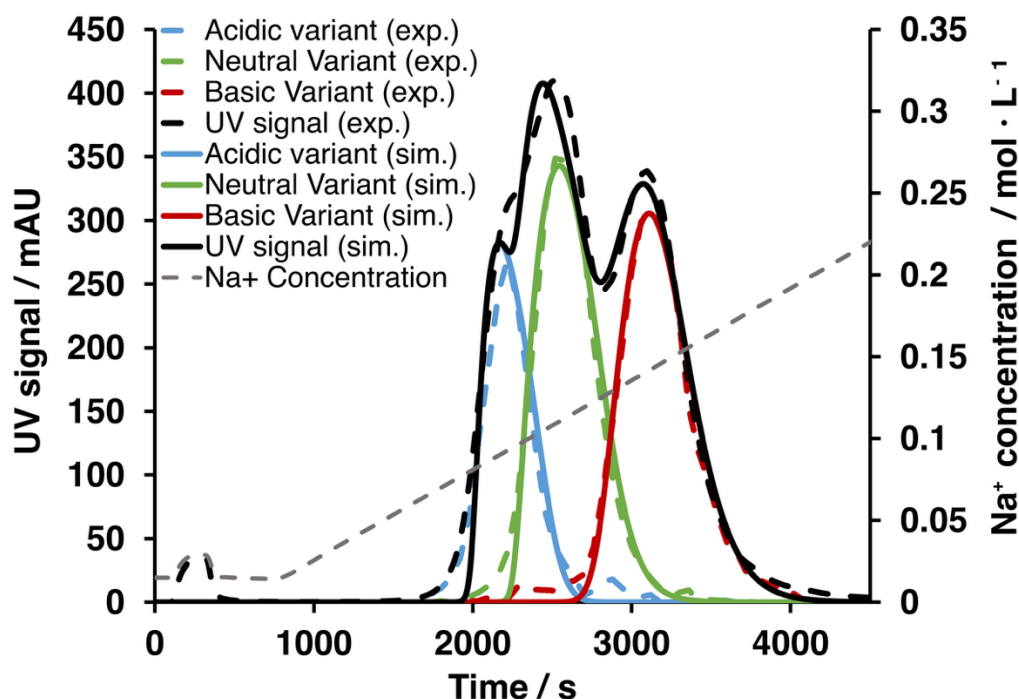


Figure 24: Validation of model parameters for high-loading chromatography runs using the 8.8 mL Natrix® CH membrane device. Gradient volume 85 MV, sodium ion concentration  $0.015 \text{ mol L}^{-1}$   $0.3 \text{ mol L}^{-1}$  and pH 6. Sample load:  $30 \text{ mg mL}^{-1}_{MV}$ . Flow rate:  $10 \text{ mL min}^{-1}$ . Experimental elution profiles of the full monoclonal antibody (black dashed line) are compared with simulated data (black solid line), showing excellent agreement. Individual charge variants, acidic (blue), neutral (green), and basic (red), were identified using analytical cation exchange chromatography and are accurately predicted by the simulation.

To further assess the predictive accuracy and scalability of the extended mechanistic model under high-loading conditions, an additional dual gradient experiment was

conducted using an elevated sample load of  $50 \text{ mg mL}^{-1}_{MV}$ . The applied gradient ranged from  $0.1 \text{ mol L}^{-1}$  to  $0.08 \text{ mol L}^{-1}$  sodium chloride and from pH 4.5 to pH 9. Experiments were performed by Viktor Simaev.<sup>155</sup> The resulting elution profiles are shown in Figure 25, where experimental data are represented by dashed lines and simulated data by solid lines. The total UV signal is plotted in black, while the acidic, neutral, and basic variants are shown in blue, green, and red, respectively.

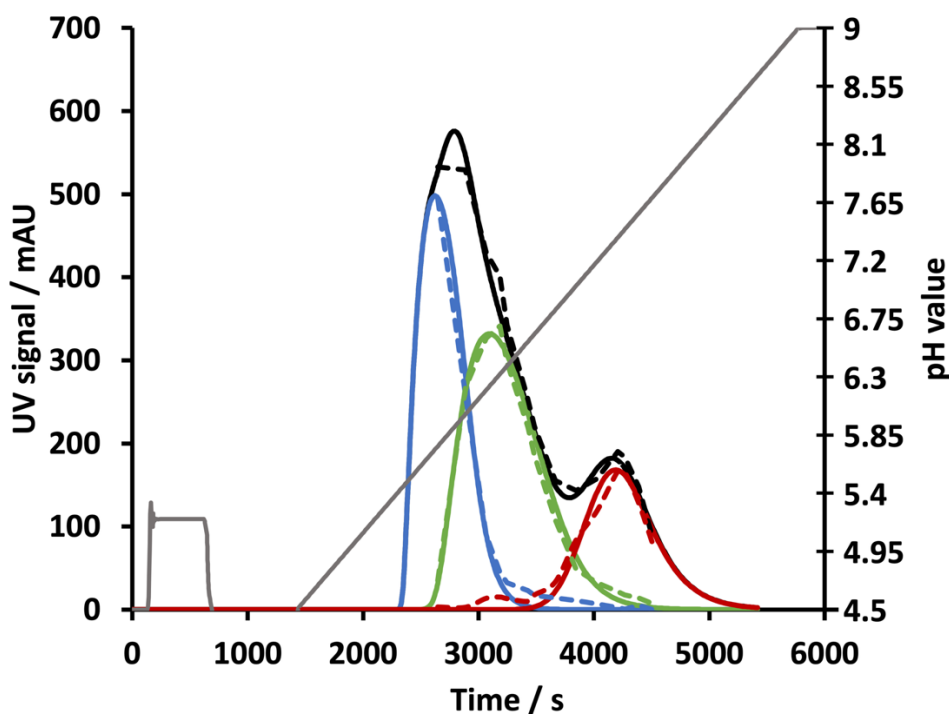


Figure 25: Validation of model parameters for high-loading chromatography runs using the 8.8 mL Natrix® CH membrane device. Gradient volume 85 MV, sodium ion concentration  $0.1 \text{ mol L}^{-1}$  to  $0.08 \text{ mol L}^{-1}$  and pH 4.5 to pH 9. Sample load:  $50 \text{ mg mL}^{-1}_{MV}$ . Flow rate:  $10 \text{ mL min}^{-1}$ . Experimental elution profiles of the full monoclonal antibody (black dashed line) are compared with simulated data (black solid line), showing excellent agreement. Individual charge variants, acidic (blue), neutral (green), and basic (red), were identified using analytical cation exchange chromatography and are accurately predicted by the simulation.

Under these conditions, elution occurred roughly in the middle of the gradient. The basic variant was well-resolved, while the acidic and neutral variants showed partial resolution, appearing as distinguishable but overlapping peaks. Compared to earlier results using an optimized dual gradient at low loading, the acidic and neutral variants appeared to elute at slightly earlier pH and salt concentrations. Further, the area of the basic variant seems reduced compared to experiments before.

## 4 DISCUSSION

### 4.1 Modelling and simulation of mAb charge variant separation on mixed-mode resin Eshmuno CMX®

#### 4.1.1 Comparison of mixed-mode to traditional ion exchanger

A delay has been shown for the mAb variants on the mixed-mode resin Eshmuno® CMX including an additional separation of the charge variants into sub-variants. The observed shift in elution behaviour of the monoclonal antibody charge variants on the Eshmuno® CMX resin, compared to the strong cation exchanger Eshmuno® CPX, highlights a fundamental difference in interaction mechanisms between the two stationary phases. While the elution order of the variants remained unchanged, all species eluted at later time points on the Eshmuno® CMX material under otherwise identical conditions. This consistent retention shift suggests a universally stronger interaction between the protein variants and the mixed-mode resin.

This increased retention can be directly linked to the introduction of hydrophobic interaction sites in the Eshmuno® CMX resin. Unlike conventional cation exchangers that rely solely on electrostatic interactions, the mixed-mode Eshmuno® CMX material incorporates additional non-ionic, hydrophobic moieties. These secondary interactions modulate protein binding by providing supplementary retention forces that oppositely sensitive to ionic strength. As a result, proteins remain bound at higher salt concentrations, leading to increased salt tolerance and delayed elution. Literature supports that mixed-mode resins leverage a combination of electrostatic, hydrophobic, and even hydrogen-bonding interactions to enhance selectivity and binding strength compared to single-mode systems.<sup>139, 156</sup>

#### 4.1.2 Additional separation on Eshmuno® CMX at medium high salt concentration

Importantly, beyond the general retention shift, the Eshmuno® CMX resin revealed enhanced resolving power, particularly for the acidic and neutral variants. Under intermediate salt concentrations, the chromatograms displayed additional peaks within the main elution zones, indicative of sub-species or isoforms with slightly differing physicochemical properties. These sub-peaks were most pronounced at elution

conditions near the inflection point of the “U-shaped” adsorption profiles, suggesting a fine balance between electrostatic and hydrophobic interactions, leading to a novel selectivity. Therefore, these additional peaks might appear due to additional separation of sub-charge variants or glycosylation variants. Mixed-mode chromatography is noted in the literature for its ability to resolve subtle protein isoforms, such as glycosylation variants, by fine tuning the hydrophobic interaction.<sup>157</sup>

The ability of Eshmuno® CMX to resolve such subtle differences implies that the hydrophobic component of the mixed-mode mechanism does not merely act as a general retention enhancer but introduces a new axis of selectivity. While electrostatic interactions dominate in traditional cation exchange media, they often lack the discriminatory power to separate closely related isoforms with comparable net charge. In contrast, the orthogonal contribution of hydrophobic interactions in Eshmuno® CMX allows discrimination based on localized surface properties, conformational differences, or varying degrees of hydrophobicity, which are characteristics that may not be distinguished by charge alone. This ability of mixed-mode resins has been often discussed in literature.<sup>158, 159</sup>

Alternatively, pre-enrichment of variants on Eshmuno® CPX may have as well contributed to the resolving power observed with Eshmuno® CMX. Eshmuno® CPX, a strong cation exchanger relying purely on ionic interactions, was used to isolate and concentrate the acidic, neutral, and basic variants prior to analysis on Eshmuno® CMX. By enriching these charge isoform pools, minor sub-species became more abundant and detectable. When these fractions were subsequently subjected to mixed-mode chromatography, the multidimensional selectivity of Eshmuno® CMX could act upon samples already biased towards variant sub-populations, leading to the observation of multiple distinct peaks under intermediate salt conditions. Such sequential chromatography, where ionic separation is followed by fine mixed-mode resolution, might have enriched specific sub forms, revealing heterogeneity that might be obscured otherwise.

#### 4.1.3 U-shaped retention behaviour

As mentioned before, a U-shaped retention behaviour has been observed for the elution of the mAb charge variants on the Eshmuno® CMX resin. A more systematic investigation of this retention behaviour was conducted through pH gradient

experiments at varying fixed salt concentrations as well as salt gradient experiments at different fixed pH. All three variants exhibited an initial decrease in retention with increasing salt levels, followed by a reversal to stronger retention at higher salt concentrations. When plotted as elution pH versus  $\text{Na}^+$  concentration, this behaviour formed distinct U-shaped curves, which are not to be confused with U-shaped retention curves, but can be seen analogous. Such profiles are characteristic of mixed-mode systems, where low salt conditions support electrostatic attraction between protein and ligand, while high salt conditions suppress these interactions but simultaneously enhance hydrophobic binding.<sup>51, 160, 161</sup> The shape and position of the curve minima reflect the relative contributions and interplay of these forces. Notably, the inflection points differed between variants, with the basic variant displaying the highest salt tolerance and strongest overall retention, suggesting it engages more strongly in both interaction modes. However, the overall difference is minor, likely due to the high structural similarities of the charge variants, which only differ in amino acid sequence exchanges or glycopatterns. These observations are in line with previous studies describing similar retention profiles for proteins on mixed-mode columns<sup>139, 162</sup>, further supporting the orthogonal nature of the interaction mechanisms.

#### 4.1.4 Mechanistic modelling of Eshmuno® CMX elution

##### 4.1.4.1 Mechanistic modelling using a standard stoichiometric displacement model

The curve fitting results using the stoichiometric displacement (SD) model without activity coefficient correction demonstrate good agreement with experimental elution data under limited conditions, particularly for pH gradient elution at low to moderate salt concentrations. Within these conditions, the model successfully captures the decreasing retention trends that reflect weakening electrostatic interactions as the protein's net charge diminishes with increasing pH value. This region aligns with the left side of the observed U-shaped retention curve for each variant, indicating that the SD model accurately represents the electrostatically dominated part of the separation process.

However, the model's predictive accuracy breaks down beyond the inflection point of the U-shaped curve, i.e., as ionic strength increases further. Within these high-salt conditions, retention no longer decreases with salt but instead increases, driven by hydrophobic interactions.<sup>161</sup> The inability of the SD model to account for this reversal

in retention suggests that it lacks the mechanistic flexibility to describe mixed-mode behaviour, which is in line with the retention model driving it. Since the SD model was developed for systems dominated by electrostatic interactions, it falls short in contexts where hydrophobic contributions become significant.<sup>51</sup> This is particularly relevant for the Eshmuno® CMX resin, where hydrophobic ligands are incorporated to provide orthogonal selectivity<sup>156</sup>. Thus, the model's failure to reproduce high-salt retention emphasizes the need for a mechanistic extension or alternative formulation that includes such non-ionic interactions.

A similar pattern is observed when fitting the salt gradient data. The SD model performs reasonably well at moderate salt concentrations under standard gradient elution conditions, especially at elevated pH, where proteins are less charged and rely more on weak electrostatic interactions. However, its performance deteriorates under reverse salt gradient conditions, where protein is bound at high salt concentrations which decrease over time. In this context, the desorption behaviour appears to be strongly influenced by hydrophobic protein-ligand interactions, which are not captured by the standard SD formalism.

In summary, the SD model provides a good first approximation of retention behaviour for low-loading, electrostatically governed systems. Its limitations become evident, however, when applied to mixed-mode materials or elution conditions that shift the dominant binding mechanism away from pure ion exchange. The observed discrepancies, especially at high salt and under reversed salt gradients, underscore the importance of incorporating additional physicochemical mechanisms such as hydrophobic interactions into the binding model. Future extensions of the model might include activity coefficient corrections or mixed-mode representations to better capture the full retention behaviour of complex stationary phases like Eshmuno® CMX.

#### 4.1.4.2 Mechanistic modelling using a mixed-mode model including different activity coefficients

This chapter delves into the modelling of charge variant elution on the mixed mode resin Eshmuno® CMX using advanced models. In contrast to the simpler SD model, the following model includes not only an additional term governing the additional hydrophobic forces, but also an activity coefficient for proteins in solution. Three different activity coefficient terms were examined, differing in their complexity.

#### 4.1.4.2.1 Mixed-mode model with simple activity coefficient

The application of the mixed-mode binding model, incorporating both electrostatic and hydrophobic interactions through an extended mechanistic framework, led to a significantly improved description of the experimental GH curves compared to classical models lacking hydrophobic terms (Figure 5). The model captures essential trends in retention behaviour across a wide range of salt and pH conditions, demonstrating its ability to reflect the aspects of mixed-mode interactions. However, while the basic variant is described with high accuracy, some limitations become evident for the acidic and neutral variants, particularly in regions of complex retention behaviour.

For the basic variant, the model shows excellent agreement across all tested conditions, supporting the validity of the mechanistic formulation in capturing the interplay of salt and pH effects on binding. This confirms that the stoichiometric representation of electrostatic interactions, combined with a hydrophobic term and an activity coefficient, is well suited to describe the pronounced mixed-mode behaviour of Eshmuno® CMX.

In contrast, the acidic variant exhibits pronounced deviations at high salt concentrations during pH gradient elution. Here, the calculated GH curves show an unusual behaviour, initially increasing sharply in an upward sigmoidal curvature before eventually returning to a typical exponential increase. This modelled artifact is not reflected in the experimental data and might stem from limitations in the model formulation. The simplified activity coefficient may fail to appropriately represent the hydrophobic interactions at high salt concentrations. The resulting misrepresentation suggests that, although the model improves over the SD formulation, it still lacks under certain boundary conditions where hydrophobic and electrostatic effects begin to compete more intricately. The used model with the simple activity coefficient has been shown to work for a variety of proteins and stationary phases in other works.<sup>145, 163</sup> Mollerup<sup>163</sup> showed, that the usage of this mixed-mode model led to improved results in modelling lysozyme, but mentions a dependency of the protein and media properties. Therefore, its likely, that with increasingly complex media and proteins, the model might run into limitations.

The neutral variant is overall well described by the model. Notably, the calculated GH curves align best with the experimental data at very low and very high salt concentrations. However, deviations arise around the inflection point of the U-shaped

retention behaviour, precisely where the transition from electrostatic to hydrophobic retention is expected. In this region, the model slightly over- or underestimates retention, suggesting again that the simplified activity coefficient may not fully capture the intricate balance between ionic and hydrophobic interactions. Since the applied activity coefficient increases exponentially with salt concentration, it may either overshoot or insufficiently account for the nuanced transition in binding strength in this intermediate range.

Further deviations emerge in the description of the reverse salt gradient experiments for the neutral and acidic variants. While the model generally captures the retention trends, noticeable misalignment between the simulated and experimental GH curves is observed. The calculated curves are shifted relative to the data, suggesting that the model's representation of salt-dependent retention is not fully accurate when starting from high salt concentrations. These discrepancies may also stem from the simplicity of the activity coefficient formulation, which might not account fully for the specific retention behaviour of proteins under descending salt conditions. Despite the mechanistic model including hydrophobic interactions, its predictive capability appears reduced in these boundary conditions, where elution is driven primarily by the gradual weakening of hydrophobic interactions rather than electrostatic displacement.

The evaluated model parameters fall within the range reported in the literature<sup>114, 163</sup>. For the activity coefficient, the  $K_s$  values lie between 8.45 and 9.42, consistent with observations from other studies. However, the literature also reports considerable variability. One study described a salt ion dependency with  $K_s$  values from approximately -2 to 4.<sup>164</sup> Another<sup>165</sup> reported a value of -34, while others calculated ranges between 0 and 14.<sup>166</sup> The reported values below zero should result in decreasing activity coefficients. In contrast to this study, hydrophobic interactions may be represented by a separate component of the model in these cases. The estimated  $K_s > 0$  indicates, that the proteins are more responsive for hydrophobic interactions.<sup>114</sup>

In summary, while the mechanistic mixed-mode model with a simplified activity coefficient formulation provides a noticeably improved description of protein retention compared to classical ion-exchange models, its performance shows inconsistency in regions where electrostatic and hydrophobic interactions contribute equally over a broader range of salt concentrations. The model reliably captures retention behaviour at the extremes of salt concentration, where either electrostatics or hydrophobicity

dominates, but shows deficits in intermediate regimes, such as the inflection zones of U-shaped GH profiles or under descending salt conditions. Similar studies shown by Altern et al.<sup>166</sup> also found, that a simple activity coefficient is sufficient for the description of mixed-mode binding. The shortcomings observed in this thesis likely arise from the limited adaptability of the activity coefficient, which, due to its exponential dependence on salt concentration, might not be able to fully reproduce the complex interplay between competing interaction types in mixed-mode systems. As further mentioned by Altern et al.<sup>166</sup>, the protein-salt activity coefficient is the main contributor to the description of the hydrophobic interaction. Therefore, if the Eshmuno® CMX resin exhibits advanced U-shaped retention behaviour, a simple exponential activity coefficient may not suffice.

#### 4.1.4.2.2 Observations regarding the isotherm parameters

The automated parameter estimation procedure, implemented via a MATLAB® script, produced hundreds of curve fits across the experimental dataset. Despite this large volume of fits, many converged to the same local minimum of the objective function, as defined by the sum of squared errors. Notably, most fitted parameters remained consistent across these solutions, except for  $\Delta\hat{G}_p^0$  (the standard-state Gibbs free energy of hydrophobic interaction) and  $n$  (the number of hydrophobic ligand interactions). While the values of these two parameters varied across runs, their product remained nearly constant, suggesting a compensatory relationship.

Graphical analysis of the correlation between  $\Delta\hat{G}_p^0$  and  $n$  revealed a strong linear relationship, reinforcing the hypothesis that the model, under current boundary conditions, does not sufficiently constrain these two terms independently. This situation leads to parameter identifiability issues, where multiple combinations of parameters yield equally good fits due to mathematical redundancy.

Upon examining the relevant mechanistic equation (Eq. 18), the dependency becomes clearer. If  $n$  is assumed constant, then the impact to  $\Delta\hat{G}_p^0$  is proportionally scaled. If the two parameters compensate for one another in the exponential, the model can absorb changes in one by inversely adjusting the other, thus explaining the observed evenness of the objective function along this parameter manifold.

Furthermore, theoretical simplifications are justifiable under specific assumptions. If the mobile phase is aqueous and exhibits no change in polarity across the experiment

(i.e., no organic modifiers or phase transitions), and if  $n$  does not depend on pH, then  $n$  can reasonably be set to zero or a fixed small value. For  $n=0$ , this implies that the hydrophobic term in the mixed-mode isotherm simplifies to 1, effectively removing it from the equation. In this case,  $\Delta\hat{G}_p^0$  becomes the sole lumped descriptor  $\Delta\hat{G}_p^{0*}$ . This may be a reasonable action, since Altern et al.<sup>166</sup> report that while hydrophobic interactions enhance salt tolerance compared to standard ion-exchange systems, the binding affinity in MMCEX shows a strictly monotonic relationship with salt concentration. This suggests explicit hydrophobic terms may be unnecessary in the model, as empirical data do not show the complex salt dependence linked to strong hydrophobic effects.<sup>166</sup>

This parameter reduction significantly improves the parsimony and numerical stability of the model. By removing  $n$  as a free parameter, the risk of overfitting and compensatory error propagation is reduced. The term  $\Delta\hat{G}_p^{0*}$  now includes all non-electrostatic contributions to retention that are constant with respect to pH and salt concentration.

#### 4.1.4.2.3 Mixed-mode modelling using activity coefficient with salt and pH dependency

The application of the mixed-mode binding model using a salt- and pH-dependent activity coefficient, as proposed by Lee et al.<sup>51</sup>, resulted in a substantial improvement in fitting accuracy across all charge variants (Figure 7). With a reduced total sum of squared errors ( $5.60 \times 10^{-4}$ ), the model clearly improved in comparison to the previous description that relied on a simple, salt-dependent activity correction. Notably, the fitting quality for the acidic and neutral variants has improved considerably, not only under standard gradient conditions but also during reverse salt gradient experiments, which previously exhibited noticeable misalignment between data and simulation. These results suggest an enhanced flexibility and descriptive power of the extended activity coefficient formulation.

The evaluated model parameters for  $\Delta G_s$ ,  $\Delta G_p$ , and the characteristic charge match those obtained with the simple model. Their values are in the same order of magnitude as reported in the literature<sup>51</sup>. However, the activity coefficient parameters  $\alpha$  and  $\beta$  deviate, where  $\alpha$  is approximately one order of magnitude lower, and  $\beta$  exhibits an opposite sign. Despite these differences, the resulting activity coefficients remain highly similar.

A reason for the improved performance may lie in the empirical formulation's ability to better reflect the complex, condition-dependent nature of protein-ligand interactions in mixed-mode systems. As it has been shown in literature, a protein's hydrophobicity<sup>167</sup> or its tendency to bind to hydrophobic materials<sup>168</sup> are dependent on the pH value, especially for high salt concentrations<sup>169</sup>. Therefore, it's reasonable to include a pH dependency to the model's activity coefficient responsible for describing the hydrophobic interaction. This could be particularly important in the transition region around the inflection point of U-shaped GH curves, where both pH dependent electrostatic and hydrophobic interactions contribute nearly equally. By incorporating both pH and salt concentration as variables, the activity coefficient might be able to modulate binding strength in a more nuanced and responsive manner as shown in previous work.<sup>51</sup>

The improved agreement in reverse gradient conditions further supports this interpretation. In these cases, the system transitions from high to low salt, altering the strength of hydrophobic interactions. A purely salt-based activity correction might lack the necessary sensitivity to account for such dynamic behaviour. In contrast, the salt- and pH-coupled formulation appears to offer sufficient empirical flexibility to match the experimental data.

Despite these clear advantages, it is important to recognize the limitations of this approach. The adopted activity coefficient remains empirical in nature and lacks a direct mechanistic interpretation. While it succeeds in reproducing observed retention trends, it does not provide insight into the underlying physicochemical processes. For mechanistic understanding and broader applicability, especially in the context of process optimization or extrapolation, a more physically grounded description would be preferable.

#### 4.1.4.2.4 Complex activity coefficient

The application of the mixed-mode model incorporating a complex activity coefficient, accounting for both salting-in and salting-out effects, resulted in the best overall agreement between simulation and experiment (Figure 8). The total sum of squared errors decreased further to  $5.33 \times 10^{-4}$ , showing a modest improvement over the previously used salt- and pH-dependent formulation ( $5.60 \times 10^{-4}$ ) and a clear enhancement relative to the basic model ( $9.65 \times 10^{-4}$ ). Although the numerical gain in accuracy is relatively small, the calculated GH curves align more closely with the

experimental profiles across all tested conditions, providing a visually more consistent and refined representation of the retention behaviour.

The fitted parameters yielded slightly lower  $\Delta G_p$  values compared to both previous models. Parameters related to the characteristic charge remained in the same order of magnitude as in the other models. For the activity coefficient, the parameters  $\tau$ ,  $\phi$ , and  $\eta$  were comparable across all three variants. Notably,  $\tau$  and  $\eta$  showed extreme values. However,  $\tau$  was about two orders of magnitude higher, and  $\eta$  two orders lower, than reported for lysozyme<sup>147</sup>. As these parameters are linked to dipole moment and protein size<sup>146</sup>, such deviations seem plausible for a larger protein like a monoclonal antibody.

The enhanced performance of this model can be attributed to its more nuanced description of how salts modulate protein-ligand interactions in mixed-mode systems. By incorporating both salting-in and salting-out contributions, the activity coefficient might respond to ionic strength in a bidirectional manner, thereby more closely reflecting the underlying thermodynamics. At low salt concentrations, salting-in effects promote protein solubility and weaken retention due to increased hydration and electrostatic screening. Conversely, at high salt concentrations, salting-out effects dominate, reducing solvation and favouring hydrophobic interactions, which in turn enhances retention.<sup>170</sup> This dual response mechanism may enable the model to better capture the retention characteristics across the full gradient range.

An interesting aspect of the complex activity coefficient is its potential to exhibit a shallow U-shaped response to increasing salt concentrations under certain conditions.<sup>147</sup> This behaviour may contribute to the model's improved ability to reproduce the U-shaped GH retention profiles observed in mixed-mode chromatography, particularly for the neutral and acidic variants. Here, electrostatic and hydrophobic contributions manifest concurrently, and a model capable of capturing this complex interplay with sufficient flexibility becomes essential. The observed high degree of correlation between experimental data and model predictions suggests that the U-shaped modulation of the activity coefficient might be important for accurately simulating the transition region where dominant interaction modes shift.

However, this improved accuracy is accompanied by an increase in model complexity. Each formulation of the activity coefficient introduces a different number of parameters: the simplest salt-dependent model includes one adjustable term, the empirical salt and

pH-dependent version adds a second, and the salting-in/salting-out formulation requires three parameters. Including additional parameters typically improves a model's ability to represent data but can also lead to overfitting and challenges with parameter identifiability, particularly in situations with limited or noisy data. In this case, the added complexity of the salting-in/salting-out model is based on physicochemical phenomena rather than empirical adjustments. This approach provides a description of the system that is more mechanistically interpretable and may support model extrapolation and broader applicability.

In conclusion, while the salting-in/salting-out-based activity coefficient provides only a slight improvement in fitting precision compared to the previous empirical formulation, it offers significant advantages in terms of interpretability and relevance to the underlying thermodynamics of mixed-mode retention. Notably, its ability to accurately reproduce subtle features in the experimental data, such as the inflection zones of U-shaped GH profiles and the behaviour under reverse gradients, makes it a valuable extension of the model. Consequently, this formulation represents a meaningful step towards a more mechanistically robust description of complex protein-ligand interactions in mixed-mode chromatographic systems.

#### 4.1.4.3 Calculated activity coefficients in detail

Activity coefficients (ACs) reflect the non-ideal behaviour of proteins in solution and are known to vary with salt concentration.<sup>171</sup> They must be included in mechanistic models for liquid chromatography, since protein solutions are known to behave highly non-ideally under certain conditions.<sup>165, 171</sup> Especially at very low and very high ionic strengths, protein behaviour in solution deviates markedly from Raoult's law, reflected by activity coefficients deviating from unity.<sup>171, 172</sup> Raoult's law states that in an ideal solution, the partial vapor pressure of each component is proportional to its mole fraction.<sup>64</sup> At high salt concentrations, stronger solute-solute and solvent-solvent interactions dominate, leading to a positive deviation from Raoult's law as protein solubility is reduced and HIC interactions are promoted.<sup>104, 162</sup> In contrast, at very low salt concentrations, strong solute-solvent interactions prevail, causing negative deviations from Raoult's law. In this case, the protein's escaping tendency decreases and HIC interactions are weakened. This dual behaviour is only captured in the complex activity coefficient formulation, which accounts for both salting-in and salting-out effects.

#### 4.1.4.3.1 Simple activity coefficient

The application of the simple activity coefficient provided a clear improvement over the baseline SD model without any activity correction. By introducing a salt-dependent adjustment, the model was able to reproduce the main retention trends across pH gradient and salt gradient experiments and thereby capture, at least in part, the mixed-mode behaviour of the Eshmuno® CMX resin. This highlights that even a basic representation of HIC behaviour can substantially enhance the predictive capability of mechanistic models in mixed-mode chromatography.

Nevertheless, important limitations became apparent. In particular, the model still struggled to describe reverse salt gradient experiments. While forward gradients at moderate ionic strength were reproduced reasonably well, the retention behaviour upon decreasing salt concentrations could not be aligned with experimental data. From the perspective of the activity coefficient, this shortcoming might be attributed to the lack of flexibility in the simple exponential formulation. Since the function enforces an exponentially increasing correction with salt concentration, it might not accommodate the more complex interplay of forces that governs desorption under descending gradients.

#### 4.1.4.3.2 pH and salt dependent activity coefficient

Extending the simple exponential formulation with an additional pH dependency led to a noticeable improvement in the model's ability to describe experimental retention data. Compared to the simple activity coefficient, the salt- and pH-dependent version captured not only the main retention trends across forward gradients but also achieved a reasonable description of reverse salt gradient experiments, which had previously been poorly represented. This improvement might be directly linked to the additional flexibility provided by the pH term, which allows the model to respond to changes in the protein charge state and to modulate the balance between electrostatic and hydrophobic interactions more dynamically.

A graphical examination of the activity coefficient surfaces (Figure 10) highlights these effects clearly. At lower salt concentrations, activity coefficient values for all variants are comparable and only slightly affected by pH, closely mirroring the behaviour described by the simple exponential model. As the ionic strength increases, however,

the impact of pH grows more pronounced, causing noticeable shifts between the activity coefficients for the acidic, neutral, and basic protein variants.

In particular, the acidic variant displays a markedly distinct trend, with its activity coefficient increasing sharply as the pH rises. This unique behaviour across variants may enable the model to better capture the nuanced transitions near the inflection points of U-shaped retention curves. In these regions, electrostatic and hydrophobic interactions are in close competition, and the model's enhanced flexibility allows it to more accurately reflect retention characteristics, even under inverse salt gradient conditions.

It is important to note, however, that the salt- and pH-dependent activity coefficient remains fundamentally empirical. Although this approach leads to better numerical agreement and more accurately reflects experimental observations than the simpler model, it does not directly enhance our understanding of the underlying physicochemical mechanisms of protein-ligand interactions. The observed improvements are primarily attributed to the increased mathematical flexibility of the model, rather than a truly more realistic depiction of system behaviour.

#### 4.1.4.3.3 Complex activity coefficient

Introducing the complex activity coefficient, which accounts for both salting-in and salting-out contributions, led to a further improvement in model performance. Compared to the purely salt-dependent exponential term and the empirical salt- and pH-dependent formulation, this description provided the most consistent agreement between simulation and experiment across the dataset. The model was able to capture both standard and reverse gradient elution profiles to a high degree of accuracy, indicating that the more nuanced handling of ionic strength effects addressed shortcomings observed in the previous approaches.

A key feature of the complex formulation is the delayed onset of increase. Activity coefficients remain at comparatively low values (below  $\sim 100$ ) up to around  $1.1 \text{ mol L}^{-1} \text{ Na}^+$ , after which they rise first gradually and then more steeply, approaching an exponential trajectory similar to the simple model. This two-phase behaviour can be attributed to the combined salting-in and salting-out effects: at intermediate ionic strength, hydration and electrostatic screening limit hydrophobic contributions, whereas at high ionic strength, reduced solvation favours stronger hydrophobic

association. The resulting progression provides a more realistic description across the full salt range and avoids the maybe unfavourable steep escalation observed with the simple exponential model.

Another notable aspect is that the curves of the acidic, neutral, and basic variants are nearly overlapping. This indicates that the complex model does not need to compensate for shortcomings by generating different activity coefficients for each variant, as seen in the simpler formulations. This outcome is reasonable, as the charge variants are isoforms of the same monoclonal antibody and thus expected to differ only slightly in their non-ideal behaviour.

All models showed very high activity coefficients ( $>10^3$ ), especially at higher salt concentrations. Similarly, literature reports that activity coefficients can be substantially elevated in highly non-ideal solutions with values up to  $10^5$ .<sup>173</sup> Sjöberg and Mortensen<sup>173</sup> found, that they can reach these high values already for low protein concentrations. Further, calculating the activity coefficient for Lee et al.<sup>51</sup> using their model, they reach above  $10^3$  for salt concentrations exceeding  $0.9 \text{ mol L}^{-1}$ . Using the  $K_s$  values from Hahn et al.<sup>114</sup> to calculate the activity coefficient for the simple model, they also evaluate to values above  $10^3$ . These studies prove, that it isn't uncommon for activity coefficient to reach high values for protein solutions.

Taken together, these findings suggest that all three formulations can reproduce aspects of the experimental data, but their suitability depends on the circumstances and on the desired balance between accuracy, interpretability, and complexity. The complex activity coefficient delivered the most precise fits overall and provided the most physically plausible description of high-salt behaviour, but at the cost of three additional parameters. The medium salt- and pH-dependent formulation incorporated two additional parameters, enhancing performance through increased empirical flexibility, whereas the simplified exponential model, which introduced just one extra parameter, provided a more streamlined extension, but demonstrated limitations when applied to reverse gradients and elevated salt concentrations.

#### 4.1.5 Model validation

The first validation test of the calibrated model involved simulating a pH gradient experiment that was also part of the original dataset used for model calibration. This approach served as a baseline to assess whether the parameterized model could

accurately reproduce the experimental retention behaviour under conditions it was explicitly fitted to.

The agreement between simulated and experimental elution profiles (Figure 9) is excellent. The main peak is predicted with high accuracy in terms of both retention volume and overall peak shape. This indicates that the combination of the mixed-mode isotherm and the lumped rate transport model reliably captures the essential retention mechanisms and mass transfer dynamics for the neutral variant under the specified conditions.

A minor deviation, however, is observed in the form of a small shoulder on the leading edge (lower pH side) of the experimental peak, which is not reproduced in the simulated profile. This discrepancy likely stems from a minor presence of residual charge variants in the purified sample. Specifically, it is challenging to achieve complete separation of variant 1 (acidic) from variant 2 (neutral) during preparative isolation. The resulting impurity, although present at low levels, may contribute to an early-eluting shoulder that is not captured by the model, as the simulation was performed assuming a single, pure species. This observation emphasizes the sensitivity of the experimental setup and highlights an inherent limitation in the calibration approach. While the model can accurately simulate the main component's behaviour, it will not predict the impact of unmodeled minor sub charge variants, unless they are explicitly included. Nonetheless, the discrepancy is minor and does not significantly detract from the overall predictive quality.

Importantly, the strong match between simulation and experiment under calibration conditions provides confidence in the validity of the estimated model parameters.

#### 4.1.6 Model validation with reverse salt gradient elution

In the second validation step, a reverse salt gradient experiment was simulated using the calibrated mixed-mode model. This setup, which transitions from high to low salt concentrations at constant pH, primarily leverages the hydrophobic interaction component of the mixed-mode material. At the initial high salt concentration (0.85 mol L<sup>-1</sup> sodium sulphate), proteins are retained through enhanced hydrophobic interactions and subsequently eluted as ionic strength decreases.

The comparison between simulation and experiment (Figure 10) again shows strong agreement, particularly in predicting the main elution peak. The simulated retention

time and peak shape align closely with experimental results, confirming the model's capability to capture hydrophobic binding behaviour under reverse gradient conditions, which might not have been adequately described by just a classical ion-exchange models alone.

Minor deviations were observed in the form of additional shoulders bordering the main peak in the experimental chromatogram, which were not reproduced by the simulation. Several potential explanations for these discrepancies exist. Most plausibly, they stem from sample impurities, where small fractions of other charge variants persist despite prior purification. These minor species were not included in the calibration or simulation and, therefore, are not predicted by the model.

Another explanation might be the novel selectivity due to the orthogonal interaction modes, leading to unique separations. A characteristic of mixed-mode interactions, which has already been reported in literature.<sup>160, 174, 175</sup> In this case, the reverse gradient may emphasize subtle differences in retention among closely related sub charge variants of the neutral species. Since the model was calibrated using only the main peak of each variant and assumes a single binding species per simulation, any secondary peaks or distributional heterogeneity are inherently excluded. This limits the model's ability to reproduce complex or emerging selectivity phenomena under non-standard conditions.

Despite these minor differences, the overall description of the elution profile is highly acceptable. The dominant retention mechanism is well captured, and the model accurately reproduces the principal behaviour of the solute. These findings support the model's applicability, especially in capturing non-electrostatic retention mechanisms like hydrophobic interaction under inverted gradients. To further enhance model accuracy in future applications, one strategy could involve explicitly incorporating additional eluting species through deconvolution.

#### 4.1.7 Validation using dual gradient elution

In the third validation, the model was tested against a dual anti-parallel gradient experiment, combining a salt gradient decreasing from 0.85 mol L<sup>-1</sup> to 0.035 mol L<sup>-1</sup> sodium sulphate with a simultaneous pH increase from 5 to 8. This elution strategy modulates two independent retention mechanisms simultaneously, where the increase

in pH lowers electrostatic interactions by reducing the net charge of the protein, while a decrease of the salt concentration lowers hydrophobic interactions.

Though both changes weaken overall retention, they target different interaction modes. Under certain conditions, especially around the inflection point of the U-shaped retention curve, the simultaneous weakening of hydrophobic and electrostatic interactions may result in a delicate balance, where both interaction types remain comparably strong throughout the elution. Rather than cancelling each other out, this fine interplay prevents one mechanism from dominating, thereby creating a highly selective elution environment. This may amplify small differences in physicochemical properties between species, which are otherwise unresolved under simpler gradient conditions.<sup>160, 174, 175</sup>

In general, the simulation of this complex dual-gradient scenario (Figure 11) shows accurate predictive performance, even though no dual-gradient experiments were included in the model calibration. The main elution peak is reproduced in both shape and general retention region, indicating that the model can predict outcomes under previously untested conditions.

A retention shift is observed, with the simulated peak eluting slightly earlier than the experimental one. This deviation may not simply reflect modelling inaccuracy, but rather the influence of a more selective elution environment created by the dual gradient as discussed before. Under these conditions, electrostatic and hydrophobic interactions remain simultaneously active and finely balanced throughout the elution. If applied correctly, this balance prevents either interaction mode from dominating, which may result in a highly sensitive retention environment. In such an environment, even minor structural or physicochemical differences between closely related charge variants can alter retention enough to cause subtle separation effects.

This interpretation may be supported by the shoulders observed on the experimental peak, which are absent in the simulation. While one explanation remains the presence of residual variant impurities in the sample, the observed shoulder patterns, particularly under these specific gradient conditions, may suggest an additional mechanism. The fine interplay of interaction forces in the dual gradient may enable partial resolution of subpopulations, which usually co-elute under simpler conditions. As a result, the experimental peak becomes slightly broadened or asymmetric, possibly shifting the apparent retention maximum and resulting in the fronting and tailing observed.

Because the model assumes a single homogeneous species, it is not equipped to capture these subtle distributions within a charge variant pool. Nonetheless, the discrepancy between simulation and experiment may reflect not a shortcoming of the model, but rather the increased resolving power of the dual gradient system itself.

#### 4.1.8 Concluding the modelling and simulation of charge variant separation on Eshmuno® CMX

The combination of experimental analysis and mechanistic modelling provided comprehensive insight into the complex retention behaviour of mAb charge variants on the mixed-mode resin Eshmuno® CMX. Initial studies confirmed the presence of U-shaped elution profiles and additional sub-variant separations, highlighting the dual contribution of electrostatic and hydrophobic interactions. While the standard stoichiometric displacement model offered a suitable baseline for purely ionic behaviour, it failed to capture high-salt retention trends and reverse gradient effects. Extensions to the model, incorporating increasingly complex activity coefficients, demonstrated that hydrophobic contributions and non-ideal solution effects are essential for accurately describing protein behaviour in mixed-mode chromatography. Notably, the final model incorporating salting-in and salting-out effects achieved the best balance between accuracy and mechanistic interpretability. Its successful validation under linear, reverse, and dual-gradient conditions underscores its applicability and potential utility in predictive process development.

#### 4.2 Modelling, simulation and scale up of Natrix® CH mixed-mode membrane adsorber

Sections of this chapter have been published in Hedrich et al.<sup>153</sup>

##### 4.2.1 Comparison of ion exchange membrane with mixed-mode Natrix® CH

The initial bind-and-elute experiments using the Natrix® CH membrane demonstrated its capability to effectively separate monoclonal antibody charge variants using a pH gradient under elevated salt concentrations. The retention and elution behaviour observed under these conditions provided early indications of novel separation mechanisms at play. To test whether this behaviour was unique to the Natrix® CH material, a direct comparison was made with a commercially available strong cation exchange (CEX) membrane of comparable ionic capacity and backbone porosity.

The results clearly showed that the Natrix® CH membrane retained the charge variants longer, particularly at moderate pH values ranging from 5.2 to 6.3, whereas the reference CEX membrane facilitated elution earlier, between pH 5.0 and 5.5. The shift in elution to later pH values on Natrix® CH suggests stronger overall interactions, which are unlikely to be explained by electrostatic forces alone, especially since both membranes nominally share similar ion-exchange functionalities. This delayed retention thus implies the presence of additional binding interactions, most plausibly introduced through hydrophobic moieties on the Natrix® CH membrane.

The orthogonal nature of these hydrophobic contributions becomes particularly evident in the case of the basic variant, which eluted much later on the Natrix® CH membrane than on the conventional CEX. Interestingly, the acidic and neutral variants did not show significant changes in elution behaviour between membranes, implying that hydrophobic interactions in Natrix® CH may preferentially affect certain conformations or surface properties, possibly related to surface hydrophobic patches. This enhanced selectivity for the basic variant supports the hypothesis that the additional hydrophobic groups not only increase salt tolerance but also modulate selectivity by interacting with specific physiochemical features of certain charge isoforms.

This behaviour aligns with established descriptions of mixed-mode chromatography, where a dual mechanism of electrostatic binding and hydrophobic interaction governs retention. A hallmark of such systems, as for example seen with the resin-based material Eshmuno® CMX (3.1.1.3), is the U-shaped retention curve when elution is performed under increasing salt concentrations: at low salt, electrostatic binding dominates, while increasing salt screens ionic interactions but simultaneously promotes hydrophobic retention. However, in this study, the Natrix® CH membrane did not exhibit increased binding at very high Na<sup>+</sup> concentrations ( $\geq 1 \text{ mol L}^{-1}$ ). This absence of enhanced hydrophobic retention suggests that while Natrix® CH is different in retention compared to a traditional IEX membrane, its behaviour does not fully align with a mixed-mode system as seen with the resin-based Eshmuno® CMX. It may instead act as a hydrophobically modified ion-exchange membrane, where the hydrophobic component enhances retention and selectivity at moderate ionic strength, but does not function as a standalone hydrophobic interaction mechanism under high-salt conditions.

#### 4.2.2 Modelling with SD model

The final fits, illustrated in Figure 17, show strong agreement between model predictions and experimental observations for both pH and salt gradient elution experiments. The elution order, acidic, neutral, and then basic variant, is preserved across both types of gradients, consistent with expectations based on the relative charge and binding strength of the variants. This further confirms the dominance of electrostatic interactions in the binding process, with limited or consistent contributions from hydrophobic retention. Interestingly, although prior experiments suggested that hydrophobic interactions seem to influence retention, particularly in the case of the basic variant, the ion-exchange model was still sufficient to capture the observed elution behaviour to an exceptional degree. This further deepens the hypotheses, that the contribution of hydrophobic interactions is either relatively minor or approximately constant across conditions. However, it could also be effectively absorbed into the fitted electrostatic interaction parameters.

This is consistent with observations of modelling in other fields, where tightly coupled or compensatory mechanisms can lead to non-identifiability. In such cases, simplified models may still reproduce observed behaviour and remain fit-for-purpose, even if the individual mechanisms cannot be separated.<sup>176</sup> In other words, in systems where two mechanisms act in parallel but are tightly coupled, a single-mechanism model may still perform well because its parameters adapt to compensate for the missing mechanism. While this limits the model's interpretability with respect to physical mechanisms, it does not diminish its predictive utility within the studied parameter range.

The estimated model parameters might support this interpretation partly. The fitted values for the protein-specific change of Gibbs free energy of adsorption,  $\frac{\Delta G_L^0}{RT}$ , ranged narrowly between 27.57 and 29.13 across all three variants, reflecting subtle differences in binding affinity that are consistent and explainable due to their minor structural and charge differences. In contrast, the value for  $\frac{\Delta G_S^0}{RT}$  was held constant at 2.91, as it represents the change in Gibbs free energy of counterion association and is expected to remain constant across variants and experimental conditions within the SD model framework. The values are in the same order of magnitude as reported in literature.<sup>50, 141</sup> The close similarity of fitted parameters across all charge variants

underscores the structural and physicochemical proximity of the variants, all of which are derived from the same parent monoclonal antibody.

These results reinforce the notion that the primary distinguishing factor between the variants is charge-based, and that their retention behaviour is governed predominantly by differences in electrostatic interaction strength, rather than by substantial structural divergence or hydrophobicity. However, this interpretation cannot be fully upheld when considering the additional separation observed on the Eshmuno® CMX resin, another mixed-mode material. The emergence of further-resolved sub-variants on Eshmuno® CMX, which likely arises from increased hydrophobic interactions, indicates that the retention behaviour in combination with the mAb02 charge variants is not governed by electrostatics alone. Consequently, the assumption that hydrophobicity plays no role in distinguishing the variants must be considered carefully. It shows that the difference in the ligands of both materials might be the leading cause of the nuanced selectivity observed. Such findings underscore the complexity inherent in chromatographic separations, where subtle alterations in ligand chemistry or surface modification can translate to significant differences in variant resolution, particularly under the coupled influence of pH and ionic strength.

#### 4.2.3 Charge profile

Figure 18 presents the charge profiles of the three monoclonal antibody charge variants, showing how their characteristic charge  $\nu(pH)$  evolves with increasing pH. These profiles were not experimentally measured directly but were calculated from the fitted model parameters obtained during the mechanistic modelling of the linear gradient elution data. As such, the absolute charge values may not precisely reflect the true characteristic charges of the proteins. Nevertheless, the trends derived from these parameter-based profiles provide meaningful insight into the relative electrostatic behaviour of the variants under varying pH conditions.

At low pH (around 4.5), all three variants exhibit similarly high characteristic charges, approximately 18, which reflects the most protonated state modelled within the calibrated range. As pH increases, the characteristic charge decreases in a titration-like manner, as would be expected from deprotonation of charged amino acid residues. By pH 8, the modelled charge values decline into a range between approximately 5.5 and 8.6, depending on the variant. While these values may not correspond exactly to

the real characteristic charges, they capture the expected trend in charge reduction across the gradient. The values themselves are in the same range as seen in other literature for monoclonal antibodies.<sup>112, 113, 177</sup>

The relative differences between the variants are particularly informative. The acidic variant shows the largest overall decrease in charge, the neutral variant a moderate decline, and the basic variant retains the highest charge across the pH range. This pattern is consistent with the charge variant nomenclature and directly correlates with the experimentally observed elution order: the acidic variant elutes first due to reduced electrostatic interaction at higher pH, followed by the neutral, and finally the basic variant, which retains the strongest interaction and elutes last.

Moreover, the shape of the modelled curves reveals that the rate of charge decline increases slightly at higher pH values, especially beyond pH 6.5. This behaviour may indicate simultaneous deprotonation of clustered amino acids, suggesting that the acidic variant contains more such residues than the neutral or basic variants. Such information is valuable in understanding the gradient sensitivity of each variant, particularly in mixed-mode systems where pH and salt jointly influence retention.

#### 4.2.4 Model validation

To validate the predictive quality of the estimated model parameters, *in silico* simulations were conducted with the goal of identifying optimal conditions for separating the pre-purified monoclonal antibody charge variants. These simulations served as application of the previously calibrated model, offering a means of testing whether the parameter set, derived from linear gradient elution experiments, could be transferred to more complex gradient conditions and still accurately predict chromatographic behaviour.

The optimization routine identified an antiparallel dual gradient, combining a pH increase from 5.0 to 8.0 with a simultaneous salt decrease from 0.1 mol L<sup>-1</sup> to 0.08 mol L<sup>-1</sup> NaCl, as the most effective strategy. This type of dual gradient is particularly advantageous in mixed-mode systems, where electrostatic interactions and protein charge evolve continuously with pH, while salt concentrations modulate both electrostatic screening and potential hydrophobic contributions.

As illustrated in Figure 19, the simulation predicted clear separation between the acidic and neutral variants and nearly baseline resolution of the basic variant. These

predictions were then experimentally validated using the optimized conditions. The close agreement between simulated (solid lines) and experimental (dashed lines) elution profiles confirms that the model was not only well-fitted to the data but also sufficiently generalizable to predict retention behaviour under new, more complex gradient conditions. This strongly supports the validity of the parameter set and the physical assumptions embedded in the model.

However, a notable discrepancy was observed during the experimental run: an additional variant appeared between the neutral and basic species that had not been predicted by the simulation. Upon closer examination, this variant is likely attributable to a change in the supplied monoclonal antibody (mAb) supernatant batch. The experiments were performed using a new production lot, and it appears that the supplier may have modified upstream processing conditions, leading to the emergence of a previously absent charge variant. As a result, when new charge variant pools were created for validation, this additional species became visible for the first time. While its absence from the original modelling dataset meant it could not be predicted, the fact that the model remained highly accurate for the original three variants even in the new batch is a strong indication for its flexibility. The results suggest that the key physicochemical mechanisms captured by the model are consistent across batches, and that the system is able to accommodate moderate product variability without significant loss of predictive power.

#### 4.2.5 DBC measurements

Dynamic binding capacity (DBC) measurements were performed to evaluate the performance of the Natrix® membrane adsorber across different device formats and flow rates. Experiments were conducted at pH 5 and 0.03 mol L<sup>-1</sup> NaCl to simulate conditions relevant for bind-and-elute purification of monoclonal antibodies. Both a 1.06 mL small-scale device and a larger 8.8 mL cassette format were tested under identical operational settings to assess scale-dependent effects.

At a flow rate of 1 MV min<sup>-1</sup> (corresponding to a residence time of 2.1 min), the DBC<sub>10%</sub>, a key industry benchmark for comparing adsorber performance, was found to be 124 mg mL<sup>-1</sup><sub>MV</sub> for both membrane formats, confirming equivalent binding performance at the early breakthrough point. However, a difference emerged in the DBC<sub>95%</sub>, where the smaller device achieved 350 mg mL<sup>-1</sup><sub>MV</sub>, compared to 317 mg

$\text{mL}^{-1}\text{MV}$  for the cassette. As the same membrane material was used for both modules, the influence of ligand density can be excluded. This difference could be due to the different flow distribution influenced by the housing design and the resulting different dispersion effects.

Standard methodology focuses on comparing  $\text{DBC}_{10\%}$  values, where both membranes exhibit similar binding capacities at comparable residence times of 2.1 minutes. These findings indicate that Natrix® membranes provide over a two-fold increase in DBC compared to other mixed-mode membrane adsorbers, with all tested under their respective optimal binding conditions.<sup>164</sup> Lemma et al. reported binding capacities up to  $200 \text{ mg mL}^{-1}$  for hIgG using UV-grafted polybutylene terephthalate (PBT) ion exchange nonwoven membranes, which featured double the ligand density.<sup>77</sup>

Additionally, it should be noted that  $\text{DBC}_{95\%}$  measurements inherently exhibit greater variability and uncertainty, as they rely on accurate detection of the late-stage breakthrough tail, where protein concentration changes are gradual and harder to distinguish from noise. Factors such as sensor resolution, integration method, and baseline drift may influence the precision of  $\text{DBC}_{95\%}$  values more strongly than for  $\text{DBC}_{10\%}$ , which is detected at the steepest and most clearly defined part of the breakthrough curve. Therefore, part of the observed discrepancy may reflect experimental limitations, rather than true performance differences between membrane formats.

The DBC of the 1.06 mL membrane was further evaluated at an increased flow rate of  $10 \text{ MV min}^{-1}$ , reducing the residence time to just 0.3 min. Under these intensified conditions, the  $\text{DBC}_{10\%}$  remained relatively high at  $116 \text{ mg mL}^{-1}\text{MV}$ , while the  $\text{DBC}_{95\%}$  measured  $292 \text{ mg mL}^{-1}\text{MV}$ . This demonstrates that even with a tenfold increase in flow rate, the  $\text{DBC}_{10\%}$  dropped by only 7 %, and the  $\text{DBC}_{95\%}$  by 17 %. By comparison, conventional resin-based materials can experience up to a 50 % reduction in DBC under equivalent flow conditions.<sup>69</sup> The superior convective mass transfer properties of the Natrix® membrane likely contribute to this performance, minimizing diffusional limitations and allowing high binding even at reduced contact times.

The process implications of this are substantial. The tenfold increase in flow rate translates to a tenfold gain in productivity, increasing from  $285 \text{ g L}^{-1} \text{ h}^{-1}$  at  $1 \text{ MV min}^{-1}$  to  $2854 \text{ g L}^{-1} \text{ h}^{-1}$  at  $10 \text{ MV min}^{-1}$ , without a proportionate loss in binding capacity. This level of flow-rate-independent productivity makes the membrane highly suitable for

continuous or high-throughput purification platforms, where space-time yield and processing speed are critical.

#### 4.2.6 High load experiments

Following the characterization of membrane capacity under low-loading conditions, the model's applicability was extended to higher protein loads, reflecting more realistic process scenarios. To this end, experiments were conducted using progressively increasing monoclonal antibody concentrations, where binding was performed at fixed pH levels followed by salt gradient elution. While the initial model was based on the stoichiometric displacement (SD) framework, it proved insufficient under high-load conditions where non-linear adsorption effects become relevant. Therefore, the steric mass action (SMA) model was introduced as a more suitable model, incorporating a steric shielding factor to account for steric hindrance and capacity limitations observed at elevated protein concentrations.

Figure 20 illustrates the resulting elution profiles under increasing loading conditions, providing clear evidence of nonlinear binding behaviour. Although the major charge variants continue to elute at approximately the same salt concentration regardless of load, a subtle forward shift in peak positions is observed the higher the sample concentrations, suggesting slightly earlier elution. This trend might indicate that as binding sites become saturated, fewer proteins can be retained, and desorption begins earlier along the salt gradient.

These observations confirm that under high-loading conditions, retention no longer follows simple linear partitioning, but instead reflects a complex interplay between protein concentration, available ligand density, steric crowding, and salt-mediated desorption. Incorporating the SMA model into the mechanistic framework allows for quantitative representation of these effects and extends the model's utility from analytical-scale characterizations to preparative and process-relevant scenarios.

#### 4.2.7 Shielding fits

Using high-loading data, reverse fitting was conducted to estimate shielding factors for each charge variant under different pH and salt gradient conditions. Table 12 and Figure 20 highlight the alignment between simulated and experimental elution profiles, confirming the model's accuracy. Minor deviations between model and data, however,

may reflect the inherent complexity of the system, particularly the presence of unresolved subvariants within the main charge variant pools.

The shielding factors were derived from data obtained at protein loads up to 35 mg mL<sup>-1</sup>, with the focus on salt gradient elution. Within this range, the shielding values appeared independent of total load, suggesting that the SMA model remains stable and predictive across a range of process-relevant concentrations, at least under the tested conditions.

A clear pH-dependent trend in shielding behaviour was observed. At pH 4.5, shielding factors ranged from 85 (acidic) to 65 (neutral) and 45 (basic). As pH increased to 5.0, 5.5, and 6.0, shielding values progressively rose for the acidic variant (up to 123), while the neutral and basic variants showed more moderate increases or remained nearly constant. This trend aligns closely with the characteristic charge profiles discussed earlier: as pH increases, the net positive charge on each variant decreases due to progressive deprotonation of surface residues. The weaker electrostatic interaction between protein and ligand at higher pH levels leads to reduced binding site engagement and therefore a larger steric footprint per bound molecule, effectively increasing shielding. In other words, the lower the protein charge, the less tightly it interacts with the membrane, and the more it sterically excludes nearby ligands from further binding. This effect is most pronounced in the acidic variant, whose charge decreases steeply with pH, and least pronounced in the basic variant, which maintains higher net charge across the pH range.

In addition to the pH trend, shielding factors consistently decreased from the acidic to the basic variant at every pH level. This may as well be attributed to the higher net charge of the neutral and basic variants, which promotes stronger electrostatic interactions with the membrane ligands, thereby limiting the effective steric exclusion of neighbouring binding sites. In contrast, the acidic variant, with lower net charge at higher pH, exhibits weaker ligand interactions and correspondingly greater steric hindrance, reflected in its elevated shielding factor.

#### 4.2.8 Simulation validation

To evaluate the applicability of the calibrated model under high-loading conditions, the previously determined parameters, including the pH-dependent shielding factors, were incorporated into *in silico* simulations mimicking preparative-scale operation. A

simplified salt gradient experiment at pH 5.5 and a load of  $23 \text{ mg mL}^{-1}_{\text{MV}}$  was selected as a test case. The simulation was then experimentally validated using the original monoclonal antibody sample containing the full charge variant mixture. Variant distribution in the eluate was confirmed via IEX-HPLC.

As shown in Figure 21, both the simulation and experiment indicate no distinct separation of the individual variants under the applied salt gradient, unlike the dual-gradient strategy previously optimized (Figure 19). Nevertheless, the close agreement between experimental and simulated elution profiles confirms that the model can reliably predict retention behaviour at elevated protein concentrations, even when variant resolution is not achieved. This suggests that the model's treatment of non-linear effects such as shielding, and site saturation has been correctly included and calibrated.

The result also reinforces an important principle in model-based process design: while the model accurately predicts bulk elution behaviour and loading effects, gradient design remains critical for achieving selectivity. In this case, the simplified gradient lacks the orthogonal pH component required to differentially modulate the charge states of the variants and improve separation.

#### 4.2.9 Scale up

As illustrated in Figure 23A, the quality of separation achieved with the Natrix® CH membrane was largely maintained even at significantly elevated flow rates, exceeding twice the manufacturer's recommended value. Despite the increase in throughput, only minimal impact on resolution was observed, confirming the membrane's robustness under intensified process conditions. This performance stands in contrast to traditional resin-based chromatographic materials, which often suffer from resolution loss and binding capacity reduction under high-flow regimes. The corresponding process time improvements are evident in Figure 23B, where the reduction in separation time across various flow rates is visualized. The substantial time savings offered by the membrane highlight its suitability for high-throughput and time-critical processing environments.

Building on the confirmed performance consistency between lab- and bench-scale devices, the next step was to assess whether the lab-scale-calibrated mechanistic model could be transferred to simulate and predict outcomes at bench scale. To test this, a salt gradient experiment was designed to evaluate variant separation at elevated

load conditions. The simulation was performed at pH 6, with a NaCl gradient from 0.015 to 0.3 mol L<sup>-1</sup>, a flow rate of 10 mL min<sup>-1</sup>, and a sample load of 30 mg mL<sup>-1</sup><sub>MV</sub>. The shielding factors applied were those previously estimated under high-loading conditions (Table 12). The simulation predicted partial resolution of the three charge variants, with the basic variant eluting last. As shown in Figure 24, the experimental validation closely mirrored the *in silico* prediction, both in elution range and elution order: the acidic variant eluted first, followed by the neutral and basic variants, within a salt concentration window of 0.075 to 0.18 mol L<sup>-1</sup>. This strong agreement confirms that the model, even though calibrated on a smaller-scale device, is sufficiently robust and transferable to describe the behaviour of larger membrane modules under realistic process conditions. The accuracy in predicting retention under high load further supports the model's applicability for scale-up and process design in preparative membrane chromatography.

In another experiment, to further evaluate the predictive accuracy and scalability of the extended mechanistic model under high-loading conditions, a dual gradient experiment was performed. When simulating a basic monoclonal antibody variant under high pH and high load conditions on a Natrix® CH cation-exchange membrane, a noticeable adjustment in the steric shielding factor (e.g. from 40 down to 30) may be required to fit experimental data. Several mechanistic factors could explain why the effective shielding per antibody decreases under these conditions. A reduced steric shielding factor observed might be the direct result of a more densely packed protein layer on the membrane surface effectively shrinking the individual proteins footprint. This might arise from changes in the orientation of the mAb in different pH environments. For example, Dimer et al.<sup>178</sup> found that lysozyme has two distinct binding orientations on a cation exchanger: at low pH it binds via one region, whereas at high pH it re-orientates to bind via a different site. This re-orientation at high pH likely uses a smaller positively charged patch of the protein, meaning the protein makes less multi-point contact and occupies less surface area. More generally, proteins at elevated pH (closer to or above their isoelectric point) carry lower net charge, so they rely on more localized charge patches to bind. This can lead to a "head-on" or compact binding orientation that minimizes steric footprint, as opposed to the protein sprawling across the surface with multiple contacts at lower pH. Such restricted orientation at high pH or high loading might reduce steric hindrance and allow more proteins to fit on the membrane.

Nonetheless, the reduced shielding factor observed for the basic variant may indicate a limitation of the current model, which only accounts for ion-exchange interactions. Given the mixed-mode characteristics of the membrane, hydrophobic interactions are likely to play a role in retention, thereby influencing the apparent shielding behaviour. This may account for the observed pH dependence of the shielding factors. Additionally, these deviations could arise from the intrinsic complexity of the protein mixture, as each main variant consists of multiple sub-variants with subtle differences in charge states. Within a pH gradient, these sub-charge variants may exhibit distinct behaviours, especially in regions where fitted parameters are unavailable.

### 4.3 Conclusion

This thesis investigated how mixed-mode chromatography can be mechanistically understood and applied to the challenging task of monoclonal antibody (mAb) charge variant separation, with the goals of better understanding the retention mechanisms of multimodal ligands, establishing predictive mechanistic models to describe them, and lastly demonstrating their scalability from lab-scale to process-relevant membrane devices.

To achieve this, two stationary phases were examined: the resin-based Eshmuno® CMX and the membrane-based Natrrix® CH. Both combine cation-exchange functionality with hydrophobic contributions, enabling complex and orthogonal retention mechanisms beyond conventional ion exchange.

Mechanistic insights on Eshmuno® CMX through systematic pH and salt gradient studies using a kosmotropic salt revealed a distinctive U-shaped retention behaviour. This is a common characteristic of competing electrostatic and hydrophobic forces within one environment. Classical ion-exchange models proved insufficient, demanding the extension of the SMA framework with advanced activity coefficients to capture mixed-mode contributions. These advanced models were implemented in MATLAB® and Berkeley Madonna, reproducing experimental data in simulations under various gradient conditions, such as reverse salt gradients and dual anti-parallel gradients, supporting their predictive capacity. Further, Eshmuno® CMX demonstrated the ability to resolve not only major charge variants but also sub-variants not visible in pure ion-exchange chromatography, underlining the selectivity advantage of multimodal ligands.

The Natrix® CH membrane was evaluated as a high-throughput alternative to resin systems. At low loading, retention behaviour could be fully described using a pure ion-exchange model, affirming the usability of classical mechanistic frameworks even in multimodal systems. Under high-loading and scale-up conditions, the membrane achieved  $DBC_{10\%}$  values  $>100 \text{ mg mL}^{-1}$ , opposing the conventional view of membranes as low-capacity devices. Shielding factor estimation and *in silico* optimization allowed predictive simulations of challenging conditions, including dual gradients and elevated protein loads. An eight-fold scale-up from 1.06 mL to 8.8 mL devices confirmed both process robustness and model transferability, with only minor parameter adjustments required. High-flow studies further demonstrated that resolution could be largely maintained at process-intensified flow rates, reducing cycle times significantly compared to traditional resins.

The goals defined at the outset of this work have thus been met. The interplay of electrostatics and hydrophobicity in multimodal ligands was systematically elucidated, with experimental confirmation of U-shaped retention and orthogonal force contributions. Extended SMA-based models with activity coefficients were successfully implemented and validated, providing predictive capability across novel gradients and loading regimes. Furthermore, the calibrated models were transferred from lab-scale experiments to bench-scale membrane devices, confirming predictive scalability and practical process relevance.

## 5 SUMMARY

This thesis investigates the influence of the physicochemical properties of novel multimodal ligands on the chromatographic separation of protein charge variants, with a particular focus on monoclonal antibodies. In response to the growing need for advanced purification strategies in biopharmaceutical manufacturing, the study explores how mixed-mode chromatographic materials can be leveraged to improve resolution and scalability in the separation of closely related isoforms.

Two multimodal systems were examined: the resin-based Eshmuno® CMX and the membrane-based Natrinx® CH. Both materials combine cation exchange functionalities with hydrophobic interaction potential, enabling complex retention mechanisms beyond conventional ion exchange. The model monoclonal antibody (mAb02) served as the test system, with its acidic, main, and basic charge variants separated under various salt and pH gradient conditions.

Mechanistic modelling was employed to describe the observed separation behaviour. Using the steric mass action model as a foundation, the models were extended to account for mixed-mode interactions and incorporated customized activity coefficients. These models were implemented in MATLAB® and Berkeley Madonna and calibrated using experimental data.

The Eshmuno® CMX resin demonstrated high-resolution separation of monoclonal antibody charge variants, including partial resolution of sub-variant species not detected in initial analytics. This enhanced separation performance is attributed to the ligand's multimodal nature, which enables selective interactions sensitive to subtle structural differences, such as glycosylation or local charge distribution. A distinctive U-shaped retention profile emerged across varying salt concentrations, highlighting the dynamic interplay between the orthogonal electrostatic and hydrophobic forces. To mechanistically capture this behaviour, the modelling approach extended the classical steric mass action framework by incorporating mixed-mode isotherms that explicitly account for both ionic and hydrophobic contributions. This was achieved by implementing activity coefficients, ranging from simple salt-dependent to complex pH- and Kirkwood-based formulations, that reflect the shifting interaction dominance along the conditions. The resulting model successfully reproduced key experimental features, including U-shaped retention trends of multimodal systems.

The Natrix® CH membrane adsorber was evaluated for its potential in high-throughput and scalable separation of monoclonal antibody charge variants. At low loading conditions, the system was successfully calibrated using a classical cation exchange model based on the steric mass action framework. Despite the membrane's multimodal character, the pure ion exchange description proved sufficient to capture retention behaviour under these conditions, enabling accurate prediction of elution profiles. This highlights the robustness of the steric mass action model for initial process characterization, even in systems where additional interactions may be present. At higher loads and under scaled-up conditions, the membrane achieved dynamic binding capacities exceeding  $100 \text{ mg mL}^{-1}$  ( $\text{DBC}_{10\%}$ ) for the model monoclonal antibody, challenging the general assumption of limited membrane capacity. The same steric mass action-based model, once calibrated, was applied to simulate these demanding scenarios. While the predictions aligned closely with experimental results, minor parameter adjustments were necessary, likely due to the unmodelled hydrophobic contributions becoming more pronounced at higher loads. Nevertheless, the accomplishment of an eightfold scale-up confirmed the model's scalability and its effectiveness in characterising the chromatographic process, even under conditions where solely electrostatic assumptions approach their limitations.

Overall, the integration of experimental chromatography with mechanistic modelling provides valuable insights into the behaviour of multimodal ligands and supports the development of predictive, scalable purification strategies for biopharmaceutical applications.

## 6 REFERENCES

1. Walsh, G: *Biopharmaceuticals: Biochemistry and Biotechnology, 2nd Edition*, Wiley, 2013.
2. Leader, B, Baca, QJ, Golan, DE: Protein therapeutics: a summary and pharmacological classification. *Nature Reviews Drug Discovery*, 7: 21-39, 2008. <https://doi.org/10.1038/nrd2399>
3. Walsh, G: Biopharmaceutical benchmarks 2018. *Nature Biotechnology*, 36: 1136-1145, 2018. <https://doi.org/10.1038/nbt.4305>
4. El-Fakharany, EM, El-Gendi, H, Saleh, AK, El-Sayed, MH, Alalawy, AI, Jame, R, Abdelaziz, MA, Alshareef, SA, El-Maradny, YA: The use of proteins and peptides-based therapy in managing and preventing pathogenic viruses. *International Journal of Biological Macromolecules*, 270: 132254, 2024. <https://doi.org/10.1016/j.ijbiomac.2024.132254>
5. Gronemeyer, P, Ditz, R, Strube, J: Trends in Upstream and Downstream Process Development for Antibody Manufacturing. *Bioengineering*, 1: 188-212, 2014. <https://doi.org/10.3390/bioengineering1040188>
6. Kluters, S, Wittkopp, F, Johnck, M, Frech, C: Application of linear pH gradients for the modeling of ion exchange chromatography: Separation of monoclonal antibody monomer from aggregates. *J Sep Sci*, 39: 663-675, 2016. <https://doi.org/10.1002/jssc.201500994>
7. Baeshen, MN, Al-Hejin, AM, Bora, RS, Ahmed, MMM, Ramadan, HAI, Saini, KS, Baeshen, NA, Redwan, EM: Production of Biopharmaceuticals in E. coli: Current Scenario and Future Perspectives. *Journal of Microbiology and Biotechnology*, 25: 953-962, 2015. <https://doi.org/10.4014/jmb.1412.12079>
8. Johnson, IS: Human Insulin from Recombinant DNA Technology. *Science*, 219: 632-637, 1983. <https://doi.org/10.1126/science.6337396>
9. Group, TNIoNDaSr-PSS: Tissue Plasminogen Activator for Acute Ischemic Stroke. *New England Journal of Medicine*, 333: 1581-1588, 1995. <https://doi.org/10.1056/nejm199512143332401>

10. Teo, EC-Y, Chew, Y, Phipps, C: A review of monoclonal antibody therapies in lymphoma. *Critical Reviews in Oncology/Hematology*, 97: 72-84, 2016. <https://doi.org/10.1016/j.critrevonc.2015.08.014>
11. Swain, SM, Shastry, M, Hamilton, E: Targeting HER2-positive breast cancer: advances and future directions. *Nature Reviews Drug Discovery*, 22: 101-126, 2023. <https://doi.org/10.1038/s41573-022-00579-0>
12. Jin, J, Chang, Y, Wei, W: Clinical application and evaluation of anti-TNF-alpha agents for the treatment of rheumatoid arthritis. *Acta Pharmacologica Sinica*, 31: 1133-1140, 2010. <https://doi.org/10.1038/aps.2010.134>
13. Mullard, A: 2021 FDA approvals. *Nature Reviews Drug Discovery*, 21: 83-88, 2022. <https://doi.org/10.1038/d41573-022-00001-9>
14. Kaplon, H, Chenoweth, A, Crescioli, S, Reichert, JM: Antibodies to watch in 2022. *mAbs*, 14, 2022. <https://doi.org/10.1080/19420862.2021.2014296>
15. Shepard, HM, Phillips, GL, Thanos, CD, Feldmann, M: Developments in therapy with monoclonal antibodies and related proteins. *Clinical Medicine*, 17: 220-232, 2017. <https://doi.org/10.7861/clinmedicine.17-3-220>
16. Otsubo, R, Yasui, T: Monoclonal antibody therapeutics for infectious diseases: Beyond normal human immunoglobulin. *Pharmacology & Therapeutics*, 240: 108233, 2022. <https://doi.org/10.1016/j.pharmthera.2022.108233>
17. Khatib, SE, Salla, M: The mosaic puzzle of the therapeutic monoclonal antibodies and antibody fragments - A modular transition from full-length immunoglobulins to antibody mimetics. *Leukemia Research Reports*, 18: 100335, 2022. <https://doi.org/10.1016/j.lrr.2022.100335>
18. Fryklund, L: Human growth hormone and insulin, from tissue extracts to recombinant DNA technology, their biosimilars and analogues in treatment of Endocrine Disorders. *Medical Research Archives*, 11, 2023. <https://doi.org/10.18103/mra.v11i3.3681>
19. Kemp, S, Frindik, JP: Emerging options in growth hormone therapy: an update. *Drug Design, Development and Therapy*: 411, 2011. <https://doi.org/10.2147/dddt.s23140>

20. Macdougall, IC: Development of Recombinant Erythropoietin and Erythropoietin Analogs. In, Elsevier, 2009, pp 35-48.
21. Silva, AC, Lobo, JMS: Cytokines and Growth Factors. In, Springer International Publishing, 2019, pp 87-113.
22. Chen, H-A, Hsu, R-H, Fang, C-Y, Desai, AK, Lee, N-C, Hwu, W-L, Tsai, F-J, Kishnani, PS, Chien, Y-H: Optimizing treatment outcomes: immune tolerance induction in Pompe disease patients undergoing enzyme replacement therapy. *Frontiers in Immunology*, 15, 2024. <https://doi.org/10.3389/fimmu.2024.1336599>
23. Fiege, L, Duran, I, Marquardt, T: Improved Enzyme Replacement Therapy with Cipaglucosidase Alfa/Miglustat in Infantile Pompe Disease. *Pharmaceuticals*, 16: 1199, 2023. <https://doi.org/10.3390/ph16091199>
24. Khalifa, AS, Tantawy, AA, Shawky, RM, Monir, E, Elsayed, SM, Fateen, E, Cooper, A: Outcome of enzyme replacement therapy in children with Gaucher disease: The Egyptian experience. *Egyptian Journal of Medical Human Genetics*, 12: 9-14, 2011. <https://doi.org/10.1016/j.ejmhg.2011.02.008>
25. Verbeke, R, Hogan, MJ, Loré, K, Pardi, N: Innate immune mechanisms of mRNA vaccines. *Immunity*, 55: 1993-2005, 2022. <https://doi.org/10.1016/j.immuni.2022.10.014>
26. Teo, SP: Review of COVID-19 mRNA Vaccines: BNT162b2 and mRNA-1273. *Journal of Pharmacy Practice*, 35: 947-951, 2022. <https://doi.org/10.1177/08971900211009650>
27. Nagayama, A, Ellisen, LW, Chabner, B, Bardia, A: Antibody–Drug Conjugates for the Treatment of Solid Tumors: Clinical Experience and Latest Developments. *Targeted Oncology*, 12: 719-739, 2017. <https://doi.org/10.1007/s11523-017-0535-0>
28. Lamanna, WC, Holzmann, J, Cohen, HP, Guo, X, Schweigler, M, Stangler, T, Seidl, A, Schiestl, M: Maintaining consistent quality and clinical performance of biopharmaceuticals. *Expert Opinion on Biological Therapy*, 18: 369-379, 2018. <https://doi.org/10.1080/14712598.2018.1421169>

29. Szkodny, AC, Lee, KH: Biopharmaceutical Manufacturing: Historical Perspectives and Future Directions. *Annual Review of Chemical and Biomolecular Engineering*, 13: 141-165, 2022. <https://doi.org/10.1146/annurev-chembioeng-092220-125832>
30. Barnes, LM, Dickson, AJ: Mammalian cell factories for efficient and stable protein expression. *Current Opinion in Biotechnology*, 17: 381-386, 2006. <https://doi.org/10.1016/j.copbio.2006.06.005>
31. Hermeling, S, Crommelin, DJA, Schellekens, H, Jiskoot, W: Structure-Immunogenicity Relationships of Therapeutic Proteins. *Pharmaceutical Research*, 21: 897-903, 2004. <https://doi.org/10.1023/b:pham.0000029275.41323.a6>
32. Harris, RJ, Kabakoff, B, Macchi, FD, Shen, FJ, Kwong, M, Andya, JD, Shire, SJ, Bjork, N, Totpal, K, Chen, AB: Identification of multiple sources of charge heterogeneity in a recombinant antibody. *Journal of Chromatography B: Biomedical Sciences and Applications*, 752: 233-245, 2001. [https://doi.org/10.1016/s0378-4347\(00\)00548-x](https://doi.org/10.1016/s0378-4347(00)00548-x)
33. McDonnell, S, Floyd Principe, R, Soares Zamprognio, M, Whelan, J: Challenges and Emerging Technologies in Biomanufacturing of Monoclonal Antibodies (mAbs). In, IntechOpen, 2023.
34. Le Basle, Y, Chennell, P, Tokhadze, N, Astier, A, Sautou, V: Physicochemical Stability of Monoclonal Antibodies: A Review. *Journal of Pharmaceutical Sciences*, 109: 169-190, 2020. <https://doi.org/10.1016/j.xphs.2019.08.009>
35. Mehta, KK, Vedantham, G: Next-Generation Process Design for Monoclonal Antibody Purification. In, Elsevier, 2018, pp 793-811.
36. Zhou, Y, Zhou, Z: Pharmacology and therapeutic applications of monoclonal antibodies. In, CRC Press, 2024, pp 364-369.
37. Liu, H, Gaza-Bulseco, G, Faldu, D, Chumsae, C, Sun, J: Heterogeneity of Monoclonal Antibodies. *Journal of Pharmaceutical Sciences*, 97: 2426-2447, 2008. <https://doi.org/10.1002/jps.21180>
38. Gupta, S, Jiskoot, W, Schöneich, C, Rathore, AS: Oxidation and Deamidation of Monoclonal Antibody Products: Potential Impact on Stability, Biological Activity,

- and Efficacy. *Journal of Pharmaceutical Sciences*, 111: 903-918, 2022. <https://doi.org/10.1016/j.xphs.2021.11.024>
39. Boll, B, Bessa, J, Folzer, E, Ríos Quiroz, A, Schmidt, R, Bulau, P, Finkler, C, Mahler, H-C, Huwylar, J, Iglesias, A, Koulov, AV: Extensive Chemical Modifications in the Primary Protein Structure of IgG1 Subvisible Particles Are Necessary for Breaking Immune Tolerance. *Molecular Pharmaceutics*, 14: 1292-1299, 2017. <https://doi.org/10.1021/acs.molpharmaceut.6b00816>
40. Jefferis, R: Posttranslational Modifications and the Immunogenicity of Biotherapeutics. *Journal of Immunology Research*, 2016: 1-15, 2016. <https://doi.org/10.1155/2016/5358272>
41. Shapiro, MA: Regulatory considerations in the design, development and quality of monoclonal antibodies and related products for the diagnosis and treatment of cancer. *Frontiers in Oncology*, 14, 2024. <https://doi.org/10.3389/fonc.2024.1379738>
42. Guélat, B, Delegrange, L, Valax, P, Morbidelli, M: Model-based prediction of monoclonal antibody retention in ion-exchange chromatography. *Journal of Chromatography A*, 1298: 17-25, 2013. <https://doi.org/10.1016/j.chroma.2013.04.048>
43. Kumar, V, Rathore, AS: Mechanistic Modeling Based PAT Implementation for Ion - Exchange Process Chromatography of Charge Variants of Monoclonal Antibody Products. *Biotechnology journal*, 12: 1700286, 2017. <https://doi.org/10.1002/biot.201700286>
44. Khanal, O, Kumar, V, Westerberg, K, Schlegel, F, Lenhoff, AM: Multi-column displacement chromatography for separation of charge variants of monoclonal antibodies. *Journal of Chromatography A*, 1586: 40-51, 2019. <https://doi.org/10.1016/j.chroma.2018.11.074>
45. Maria, S, Joucla, G, Garbay, B, Dieryck, W, Lomenech, A-M, Santarelli, X, Cabanne, C: Purification process of recombinant monoclonal antibodies with mixed mode chromatography. *Journal of Chromatography A*, 1393: 57-64, 2015. <https://doi.org/10.1016/j.chroma.2015.03.018>

46. Joucla, G, Le Sénéchal, C, Bégorre, M, Garbay, B, Santarelli, X, Cabanne, C: Cation exchange versus multimodal cation exchange resins for antibody capture from CHO supernatants: Identification of contaminating Host Cell Proteins by mass spectrometry. *Journal of Chromatography B*, 942-943: 126-133, 2013. <https://doi.org/10.1016/j.jchromb.2013.10.033>
47. Pezzini, J, Joucla, G, Gantier, R, Toueille, M, Lomenech, A-M, Le Sénéchal, C, Garbay, B, Santarelli, X, Cabanne, C: Antibody capture by mixed-mode chromatography: A comprehensive study from determination of optimal purification conditions to identification of contaminating host cell proteins. *Journal of Chromatography A*, 1218: 8197-8208, 2011. <https://doi.org/10.1016/j.chroma.2011.09.036>
48. Chmielowski, RA, Meissner, S, Roush, D, Linden, TO, Glowacki, E, Konietzko, J, Nti-Gyabaah, J: Resolution of heterogeneous charged antibody aggregates via multimodal chromatography: A comparison to conventional approaches. *Biotechnology Progress*, 30: 636-645, 2014. <https://doi.org/10.1002/btpr.1908>
49. McKechnie, WS, Thom, V, Kupracz, L, Pollard, J, Kandula, S, Welsh, J: A high - throughput approach to developing and optimizing mixed - mode membrane chromatography for protein purification. *Biotechnology Progress*, 39, 2023. <https://doi.org/10.1002/btpr.3308>
50. Wittkopp, F, Peeck, L, Hafner, M, Frech, C: Modeling and simulation of protein elution in linear pH and salt gradients on weak, strong and mixed cation exchange resins applying an extended Donnan ion exchange model. *J Chromatogr A*, 1545: 32-47, 2018. <https://doi.org/10.1016/j.chroma.2018.02.020>
51. Lee, YF, Kluters, S, Hillmann, M, Hirschheydt, T, Frech, C: Modeling of bispecific antibody elution in mixed - mode cation - exchange chromatography. *Journal of Separation Science*, 2017. <https://doi.org/10.1002/jssc.201700313>
52. Lee, YF, Graalfs, H, Frech, C: Thermodynamic modeling of protein retention in mixed-mode chromatography: An extended model for isocratic and dual gradient elution chromatography. *J Chromatogr A*, 1464: 87-101, 2016. <https://doi.org/10.1016/j.chroma.2016.08.026>

- 
53. Sandra, K, Vandenneede, I, Sandra, P: Modern chromatographic and mass spectrometric techniques for protein biopharmaceutical characterization. *Journal of Chromatography A*, 1335: 81-103, 2014. <https://doi.org/10.1016/j.chroma.2013.11.057>
54. Marichal-Gallardo, PA, Álvarez, MM: State-of-the-art in downstream processing of monoclonal antibodies: Process trends in design and validation. *Biotechnology Progress*, 28: 899-916, 2012. <https://doi.org/10.1002/btpr.1567>
55. Riley, CML, W. J.; Wainer, Irving W.: *Pharmaceutical and Biomedical Applications of Liquid Chromatography*, Pergamon PR, 1994.
56. Guiochon, G: Preparative liquid chromatography. *Journal of Chromatography A*, 965: 129-161, 2002. [https://doi.org/10.1016/s0021-9673\(01\)01471-6](https://doi.org/10.1016/s0021-9673(01)01471-6)
57. Debnath, S, Das, M, Mondal, S, Sarkar, BK, Babu, G: Advances in chromatography: contemporary techniques and applications. *Essential Chem*, 2: 1-27, 2025. <https://doi.org/10.1080/28378083.2025.2466624>
58. Fekete, S, Guillarme, D, Sandra, P, Sandra, K: Chromatographic, Electrophoretic, and Mass Spectrometric Methods for the Analytical Characterization of Protein Biopharmaceuticals. *Analytical Chemistry*, 88: 480-507, 2016. <https://doi.org/10.1021/acs.analchem.5b04561>
59. Rathore, AS, Kumar, D, Kateja, N: Recent developments in chromatographic purification of biopharmaceuticals. *Biotechnology Letters*, 40: 895-905, 2018. <https://doi.org/10.1007/s10529-018-2552-1>
60. Guiochon, G, Shirazi, DG, Felinger, A, Katti, AM: *Fundamentals of preparative and nonlinear chromatography*, Boston, Academic Press, 2006.
61. H. Schmidt-Traub, MS, Andreas Seidel-Morgenstern: *Preparative chromatography*, Weinheim, Wiley-VCH, 2012.
62. Urmann, M, Hafner, M, Frech, C: Influence of protein and stationary phase properties on protein–matrix-interaction in cation exchange chromatography. *Journal of Chromatography A*, 1218: 5136-5145, 2011. <https://doi.org/10.1016/j.chroma.2011.05.085>

63. Ayano, E, Nambu, K, Sakamoto, C, Kanazawa, H, Kikuchi, A, Okano, T: Aqueous chromatography system using pH- and temperature-responsive stationary phase with ion-exchange groups. *Journal of Chromatography A*, 1119: 58-65, 2006. <https://doi.org/10.1016/j.chroma.2006.01.068>
64. Robards, K, Ryan, D: *Principles and Practice of Modern Chromatographic Methods*, Elsevier, 2022.
65. Giorgio Carta, AJ: *Protein Chromatography: Process Development and Scale-Up*, Wiley-VCH, 2010.
66. Nicoud, R-M: *Chromatographic Processes*. 2015. <https://doi.org/10.1017/cbo9781139998284>
67. Teepakorn, C, Fiaty, K, Charcosset, C: Comparison of Membrane Chromatography and Monolith Chromatography for Lactoferrin and Bovine Serum Albumin Separation. *Processes*, 4: 31, 2016. <https://doi.org/10.3390/pr4030031>
68. Ghosh, R, Chen, G, Roshankhah, R, Umatheva, U, Gatt, P: A z2 laterally-fed membrane chromatography device for fast high-resolution purification of biopharmaceuticals. *Journal of Chromatography A*, 1629: 461453, 2020. <https://doi.org/10.1016/j.chroma.2020.461453>
69. Qu, Y, Bekard, I, Hunt, B, Black, J, Fabri, L, Gras, SL, Kentish, SE: The Transition from Resin Chromatography to Membrane Adsorbers for Protein Separations at Industrial Scale. *Separation & Purification Reviews*, 53: 351-371, 2024. <https://doi.org/10.1080/15422119.2023.2226128>
70. Zhou, JX, Tressel, T: Basic Concepts in Q Membrane Chromatography for Large-Scale Antibody Production. *Biotechnology Progress*, 22: 341-349, 2006. <https://doi.org/10.1021/bp050425v>
71. Zydney, AL: New developments in membranes for bioprocessing – A review. *Journal of Membrane Science*, 620: 118804, 2021. <https://doi.org/10.1016/j.memsci.2020.118804>
72. Chen, S-T, Wickramasinghe, SR, Qian, X: Electrospun Weak Anion-Exchange Fibrous Membranes for Protein Purification. *Membranes*, 10: 39, 2020. <https://doi.org/10.3390/membranes10030039>

73. Ghosh, R: Protein separation using membrane chromatography: opportunities and challenges. *Journal of Chromatography A*, 952: 13-27, 2002. [https://doi.org/10.1016/s0021-9673\(02\)00057-2](https://doi.org/10.1016/s0021-9673(02)00057-2)
74. Weaver, J, Husson, SM, Murphy, L, Wickramasinghe, SR: Anion exchange membrane adsorbers for flow-through polishing steps: Part I. clearance of minute virus of mice. *Biotechnology and Bioengineering*, 110: 491-499, 2013. <https://doi.org/10.1002/bit.24720>
75. Orr, V, Zhong, L, Moo-Young, M, Chou, CP: Recent advances in bioprocessing application of membrane chromatography. *Biotechnology Advances*, 31: 450-465, 2013. <https://doi.org/10.1016/j.biotechadv.2013.01.007>
76. Lavoie, J, Fan, J, Pourdeyhimi, B, Boi, C, Carbonell, RG: Advances in high - throughput, high - capacity nonwoven membranes for chromatography in downstream processing: A review. *Biotechnology and Bioengineering*, 121: 2300-2317, 2024. <https://doi.org/10.1002/bit.28457>
77. Lemma, SM, Boi, C, Carbonell, RG: Nonwoven Ion-Exchange Membranes with High Protein Binding Capacity for Bioseparations. *Membranes*, 11: 181, 2021. <https://doi.org/10.3390/membranes11030181>
78. Chambers, SD, Glenn, KM, Lucy, CA: Developments in ion chromatography using monolithic columns. *Journal of Separation Science*, 30: 1628-1645, 2007. <https://doi.org/10.1002/jssc.200700090>
79. Podgornik, A, Jančar, J, Mihelič, I, Barut, M, Strancar, A: Large volume monolithic stationary phases: preparation, properties, and applications. *Acta Chim Slov*, 57: 1-8, 2010.
80. Lynch, KB, Ren, J, Beckner, MA, He, C, Liu, S: Monolith columns for liquid chromatographic separations of intact proteins: A review of recent advances and applications. *Analytica Chimica Acta*, 1046: 48-68, 2019. <https://doi.org/10.1016/j.aca.2018.09.021>
81. Podgornik, A, Yamamoto, S, Peterka, M, Krajnc, NL: Fast separation of large biomolecules using short monolithic columns. *Journal of chromatography B, Analytical technologies in the biomedical and life sciences*, 927: 80-89, 2013. <https://doi.org/10.1016/j.jchromb.2013.02.004>

- 
82. Wisniewski, R, Boschetti, E, Jungbauer, A: Process Design Considerations for Large-Scale Chromatography of Biomolecules. In, CRC Press, 2020, pp 61-198.
83. Fekete, S, Guillarme, D: Ultra-high-performance liquid chromatography for the characterization of therapeutic proteins. *TrAC Trends in Analytical Chemistry*, 63: 76-84, 2014. <https://doi.org/10.1016/j.trac.2014.05.012>
84. Diedrich, J, Heymann, W, Leweke, S, Hunt, S, Todd, R, Kunert, C, Johnson, W, von Lieres, E: Multi-state steric mass action model and case study on complex high loading behavior of mAb on ion exchange tentacle resin. *Journal of Chromatography A*, 1525: 60-70, 2017. <https://doi.org/10.1016/j.chroma.2017.09.039>
85. Hanke, AT, Ottens, M: Purifying biopharmaceuticals: knowledge-based chromatographic process development. *Trends in Biotechnology*, 32: 210-220, 2014. <https://doi.org/10.1016/j.tibtech.2014.02.001>
86. Dapremont, O: 9.08 Use of Industrial Scale Chromatography in Pharmaceutical Manufacturing. In, Elsevier, 2014, pp 181-206.
87. Schweiger, S, Jungbauer, A: Scalability of pre-packed preparative chromatography columns with different diameters and lengths taking into account extra column effects. *Journal of Chromatography A*, 1537: 66-74, 2018. <https://doi.org/10.1016/j.chroma.2018.01.022>
88. Van Beijeren, P, Kreis, P, Zeiner, T: Development of a generic process model for membrane adsorption. *Computers & Chemical Engineering*, 53: 86-101, 2013. <https://doi.org/10.1016/j.compchemeng.2013.03.005>
89. Jungbauer, A: Preparative chromatography of biomolecules. *Journal of Chromatography A*, 639: 3-16, 1993. [https://doi.org/10.1016/0021-9673\(93\)83082-4](https://doi.org/10.1016/0021-9673(93)83082-4)
90. Shukla, AA, Yigzaw, Y: Modes of Preparative Chromatography. In, CRC Press, 2006, pp 201-248.
91. Jungbauer, A: Continuous downstream processing of biopharmaceuticals. *Trends in Biotechnology*, 31: 479-492, 2013. <https://doi.org/10.1016/j.tibtech.2013.05.011>

- 
92. Liu, HF, Ma, J, Winter, C, Bayer, R: Recovery and purification process development for monoclonal antibody production. *mAbs*, 2: 480-499, 2010. <https://doi.org/10.4161/mabs.2.5.12645>
93. Ghose, S, Hubbard, B, Cramer, SM: Evaluation and comparison of alternatives to Protein A chromatography. *Journal of Chromatography A*, 1122: 144-152, 2006. <https://doi.org/10.1016/j.chroma.2006.04.083>
94. Osuofa, J, Husson, SM: Comparative Evaluation of Commercial Protein A Membranes for the Rapid Purification of Antibodies. *Membranes*, 13: 511, 2023. <https://doi.org/10.3390/membranes13050511>
95. Ghose, S, Zhang, J, Conley, L, Caple, R, Williams, KP, Cecchini, D: Maximizing binding capacity for protein A chromatography. *Biotechnology Progress*, 30: 1335-1340, 2014. <https://doi.org/10.1002/btpr.1980>
96. Arora, S, Saxena, V, Ayyar, BV: Affinity chromatography: A versatile technique for antibody purification. *Methods*, 116: 84-94, 2017. <https://doi.org/10.1016/j.ymeth.2016.12.010>
97. Fahrner, RL, Knudsen, HL, Basey, CD, Galan, W, Feuerhelm, D, Vanderlaan, M, Blank, GS: Industrial Purification of Pharmaceutical Antibodies: Development, Operation, and Validation of Chromatography Processes. *Biotechnology and Genetic Engineering Reviews*, 18: 301-327, 2001. <https://doi.org/10.1080/02648725.2001.10648017>
98. Feng, LY, Matthias, J, Christian, F: Evaluation of differences between dual salt - pH gradient elution and mono gradient elution using a thermodynamic model: Simultaneous separation of six monoclonal antibody charge and size variants on preparative - scale ion exchange chromatographic resin. *Biotechnology Progress*, 0, 2017. <https://doi.org/doi:10.1002/btpr.2626>
99. Tsonev, LI, Hirsh, AG: Theory and applications of a novel ion exchange chromatographic technology using controlled pH gradients for separating proteins on anionic and cationic stationary phases. *Journal of Chromatography A*, 1200: 166-182, 2008. <https://doi.org/10.1016/j.chroma.2008.05.076>
100. Ahamed, T, Ottens, M, Nfor, BK, Van Dedem, GWK, Van Der Wielen, LAM: A generalized approach to thermodynamic properties of biomolecules for use in

- bioseparation process design. *Fluid Phase Equilib*, 241: 268-282, 2006. <https://doi.org/10.1016/j.fluid.2005.12.011>
101. Schmidt, M, Hafner, M, Frech, C: Modeling of salt and pH gradient elution in ion-exchange chromatography. *Journal of Separation Science*, 37: 5-13, 2014. <https://doi.org/10.1002/jssc.201301007>
102. Zhou, JX, Dermawan, S, Solamo, F, Flynn, G, Stenson, R, Tressel, T, Guhan, S: pH-conductivity hybrid gradient cation-exchange chromatography for process-scale monoclonal antibody purification. *Journal of Chromatography A*, 1175: 69-80, 2007. <https://doi.org/10.1016/j.chroma.2007.10.028>
103. Hjertén, S, Rosengren, J, P»hlman, S: Hydrophobic interaction chromatography. *Journal of Chromatography A*, 101: 281-288, 1974. [https://doi.org/10.1016/s0021-9673\(00\)82845-9](https://doi.org/10.1016/s0021-9673(00)82845-9)
104. Melander, W, Horváth, C: Salt effects on hydrophobic interactions in precipitation and chromatography of proteins: An interpretation of the lyotropic series. *Archives of Biochemistry and Biophysics*, 183: 200-215, 1977. [https://doi.org/10.1016/0003-9861\(77\)90434-9](https://doi.org/10.1016/0003-9861(77)90434-9)
105. Melander, WR, Corradini, D, Horváth, C: Salt-mediated retention of proteins in hydrophobic-interaction chromatography. *Journal of Chromatography A*, 317: 67-85, 1984. [https://doi.org/10.1016/s0021-9673\(01\)91648-6](https://doi.org/10.1016/s0021-9673(01)91648-6)
106. Barth, HG, Boyes, BE, Jackson, C: Size exclusion chromatography. *Anal Chem*, 66: 595R-620R, 1994. <https://doi.org/10.1021/ac00084a022>
107. Zhang, K, Liu, X: Mixed-mode chromatography in pharmaceutical and biopharmaceutical applications. *J Pharm Biomed Anal*, 128: 73-88, 2016. <https://doi.org/10.1016/j.jpba.2016.05.007>
108. Sykora, D, Rezanka, P, Zaruba, K, Kral, V: Recent advances in mixed-mode chromatographic stationary phases. *J Sep Sci*, 42: 89-129, 2019. <https://doi.org/10.1002/jssc.201801048>
109. Matte, A: Recent Advances and Future Directions in Downstream Processing of Therapeutic Antibodies. *International Journal of Molecular Sciences*, 23: 8663, 2022. <https://doi.org/10.3390/ijms23158663>

- 
110. Schmidt, A, Helgers, H, Vetter, FL, Zobel-Roos, S, Hengelbrock, A, Strube, J: Process Automation and Control Strategy by Quality-by-Design in Total Continuous mRNA Manufacturing Platforms. *Processes*, 10: 1783, 2022. <https://doi.org/10.3390/pr10091783>
111. Eslami, T, Jungbauer, A: Control strategy for biopharmaceutical production by model predictive control. *Biotechnology Progress*, 40, 2024. <https://doi.org/10.1002/btpr.3426>
112. Rischawy, F, Saleh, D, Hahn, T, Oelmeier, S, Spitz, J, Kluters, S: Good modeling practice for industrial chromatography: Mechanistic modeling of ion exchange chromatography of a bispecific antibody. *Computers & Chemical Engineering*, 130: 106532, 2019. <https://doi.org/10.1016/j.compchemeng.2019.106532>
113. Seelinger, F, Wittkopp, F, Von Hirschheydt, T, Frech, C: Anti-Langmuir elution behavior of a bispecific monoclonal antibody in cation exchange chromatography: Mechanistic modeling using a pH-dependent Self-Association Steric Mass Action isotherm. *Journal of Chromatography A*, 1689: 463730, 2023. <https://doi.org/10.1016/j.chroma.2022.463730>
114. Hahn, T, Geng, N, Petrushevskaja - Seebach, K, Dolan, ME, Scheindel, M, Graf, P, Takenaka, K, Izumida, K, Li, L, Ma, Z, Schuelke, N: Mechanistic modeling, simulation, and optimization of mixed - mode chromatography for an antibody polishing step. *Biotechnology Progress*, 39, 2023. <https://doi.org/10.1002/btpr.3316>
115. Kumar, V, Leweke, S, Heymann, W, Von Lieres, E, Schlegel, F, Westerberg, K, Lenhoff, AM: Robust mechanistic modeling of protein ion-exchange chromatography. *Journal of Chromatography A*: 462669, 2021. <https://doi.org/10.1016/j.chroma.2021.462669>
116. Wittkopp, F, Seelinger, F, Skudas, R, Schulte, M, Frech, CD: Mechanistic modeling of multi-modal chromatography: Separation of antibody variants using mixed-mode weak cation exchange resins. *Abstr Pap Am Chem S*, 255, 2018.
117. Hibbert, DB: Experimental design in chromatography: A tutorial review. *Journal of Chromatography B*, 910: 2-13, 2012. <https://doi.org/10.1016/j.jchromb.2012.01.020>

118. Shekhawat, LK, Rathore, AS: An overview of mechanistic modeling of liquid chromatography. *Prep Biochem Biotechnol*, 49: 623-638, 2019. <https://doi.org/10.1080/10826068.2019.1615504>
119. Mollerup, JM, Hansen, TB, Kidal, S, Staby, A: Quality by design - Thermodynamic modelling of chromatographic separation of proteins. *Journal of Chromatography A*, 1177: 200-206, 2008. <https://doi.org/10.1016/j.chroma.2007.08.059>
120. Mollerup, JM, Hansen, TB, Kidal, S, Sejergaard, L, Staby, A: Development, modelling, optimisation and scale-up of chromatographic purification of a therapeutic protein. *Fluid Phase Equilib*, 261: 133-139, 2007. <https://doi.org/10.1016/j.fluid.2007.07.047>
121. Sanchez - Reyes, G, Graalfs, H, Hafner, M, Frech, C: Mechanistic modeling of ligand density variations on anion exchange chromatography. *Journal of Separation Science*, 44: 805-821, 2021. <https://doi.org/10.1002/jssc.202001077>
122. Beck, J, Von Lieres, E, Zaghi, N, Leweke, S, Carta, G, Hahn, R: Patterns of protein adsorption in ion-exchange particles and columns: Evolution of protein concentration profiles during load, hold, and wash steps predicted for pore and solid diffusion mechanisms. *Journal of Chromatography A*, 1653: 462412, 2021. <https://doi.org/10.1016/j.chroma.2021.462412>
123. Creasy, A, Barker, G, Carta, G: Systematic interpolation method predicts protein chromatographic elution with salt gradients, pH gradients and combined salt/pH gradients. *Biotechnology journal*, 12: 1600636-n/a, 2017. <https://doi.org/10.1002/biot.201600636>
124. Kumar, V, Leweke, S, von Lieres, E, Rathore, AS: Mechanistic modeling of ion-exchange process chromatography of charge variants of monoclonal antibody products. *J Chromatogr A*, 1426: 140-153, 2015. <https://doi.org/10.1016/j.chroma.2015.11.062>
125. Teeters, MA, Root, TW, Lightfoot, EN: Performance and scale-up of adsorptive membrane chromatography. *J Chromatogr A*, 944: 129-139, 2002. [https://doi.org/10.1016/s0021-9673\(01\)01409-1](https://doi.org/10.1016/s0021-9673(01)01409-1)

- 
126. Ishihara, T, Kadoya, T, Yamamoto, S: Application of a chromatography model with linear gradient elution experimental data to the rapid scale-up in ion-exchange process chromatography of proteins. *Journal of Chromatography A*, 1162: 34-40, 2007. <https://doi.org/10.1016/j.chroma.2007.03.016>
127. Forssén, P, Arnell, R, Fornstedt, T: An improved algorithm for solving inverse problems in liquid chromatography. *Computers & Chemical Engineering*, 30: 1381-1391, 2006. <https://doi.org/10.1016/j.compchemeng.2006.03.004>
128. Persson, P, Nilsson, B: Parameter Estimation of Protein Chromatographic Processes Based on Breakthrough Curves. *IFAC Proceedings Volumes*, 34: 113-118, 2001. [https://doi.org/10.1016/s1474-6670\(17\)34205-2](https://doi.org/10.1016/s1474-6670(17)34205-2)
129. Zhang, Y, Lin, G-L, Forssén, P, Gulliksson, M, Fornstedt, T, Cheng, X-L: A regularization method for the reconstruction of adsorption isotherms in liquid chromatography. *Inverse Problems*, 32: 105005, 2016. <https://doi.org/10.1088/0266-5611/32/10/105005>
130. van der Heijden, F, Duin, RP, de Ridder, D, Tax, DMJ: *Classification, Parameter Estimation and State Estimation: An Engineering Approach Using MATLAB*, Wiley, 2005.
131. Leweke, S, Von Lieres, E: Chromatography Analysis and Design Toolkit (CADET). *Computers & Chemical Engineering*, 113: 274-294, 2018. <https://doi.org/10.1016/j.compchemeng.2018.02.025>
132. Leweke, S, Breuer, J, Schmölder, J, Jäpel, R, Lanzrath, H, Rao, J, Hassan, J, Zhang, W, Berger, A, Heymann, W, Eric: CADET-Core 5.0: High-Performance Solver for Advanced Biotechnology Process Modeling. *Journal of Open Source Software*, 10: 7881, 2025. <https://doi.org/10.21105/joss.07881>
133. Marcoline, FV, Furth, J, Nayak, S, Grabe, M, Macey, RI: Berkeley Madonna Version 10—A simulation package for solving mathematical models. *CPT: Pharmacometrics & Systems Pharmacology*, 11: 290-301, 2022. <https://doi.org/10.1002/psp4.12757>
134. Dorsey, JG: Editorial on "Mass transfer kinetics, band broadening and column efficiency" by F. Gritti and G. Guiochon. *J Chromatogr A*, 1221: 1, 2012. <https://doi.org/10.1016/j.chroma.2011.11.004>

- 
135. Von Lieres, E, Andersson, J: A fast and accurate solver for the general rate model of column liquid chromatography. *Computers & Chemical Engineering*, 34: 1180-1191, 2010. <https://doi.org/10.1016/j.compchemeng.2010.03.008>
136. Glueckauf, E, Coates, JI: Theory of Chromatography .4. The Influence of Incomplete Equilibrium on the Front Boundary of Chromatograms and on the Effectiveness of Separation. *J Chem Soc*: 1315-1321, 1947. <https://doi.org/DOI.10.1039/jr9470001315>
137. Mollerup, JM, Hansen, TB, Frederiksen, SS, Staby, A: Thermodynamic Modeling of Chromatographic Separation. *Adv Chromatogr*, 48: 57-97, 2010. <https://doi.org/10.1201/9781420084542>
138. Mollerup, JM: A Review of the Thermodynamics of Protein Association to Ligands, Protein Adsorption, and Adsorption Isotherms. *Chemical Engineering & Technology*, 31: 864-874, 2008. <https://doi.org/10.1002/ceat.200800082>
139. Nfor, BK, Noverraz, M, Chilamkurthi, S, Verhaert, PDEM, van der Wielen, LAM, Ottens, M: High-throughput isotherm determination and thermodynamic modeling of protein adsorption on mixed mode adsorbents. *Journal of Chromatography A*, 1217: 6829-6850, 2010. <https://doi.org/10.1016/j.chroma.2010.07.069>
140. Gerstner, JA, Bell, JA, Cramer, SM: Gibbs free energy of adsorption for biomolecules in ion-exchange systems. *Biophysical Chemistry*, 52: 97-106, 1994. [https://doi.org/10.1016/0301-4622\(94\)00006-9](https://doi.org/10.1016/0301-4622(94)00006-9)
141. Seelinger, F, Wittkopp, F, Von Hirschheydt, T, Hafner, M, Frech, C: Application of the Steric Mass Action formalism for modeling under high loading conditions: Part 1. Investigation of the influence of pH on the steric shielding factor. *Journal of Chromatography A*, 1676: 463265, 2022. <https://doi.org/10.1016/j.chroma.2022.463265>
142. Brooks, CA, Cramer, SM: Steric mass-action ion exchange: Displacement profiles and induced salt gradients. *AIChE Journal*, 38: 1969-1978, 1992. <https://doi.org/10.1002/aic.690381212>
143. Pedersen, L, Mollerup, J, Hansen, E, Jungbauer, A: Whey proteins as a model system for chromatographic separation of proteins. *Journal of chromatography*

- B, Analytical technologies in the biomedical and life sciences*, 790: 161-173, 2003.
144. Kluters, S, Hafner, M, von Hirschheydt, T, Frech, C: Solvent modulated linear pH gradient elution for the purification of conventional and bispecific antibodies: Modeling and application. *J Chromatogr A*, 1418: 119-129, 2015. <https://doi.org/10.1016/j.chroma.2015.09.053>
145. Deitcher, RW, Rome, JE, Gildea, PA, O'Connell, JP, Fernandez, EJ: A new thermodynamic model describes the effects of ligand density and type, salt concentration and protein species in hydrophobic interaction chromatography. *Journal of Chromatography A*, 1217: 199-208, 2010. <https://doi.org/10.1016/j.chroma.2009.07.068>
146. Arkell, K, Breil, MP, Frederiksen, SS, Nilsson, B: Mechanistic Modeling of Reversed-Phase Chromatography of Insulins with Potassium Chloride and Ethanol as Mobile-Phase Modulators. *ACS Omega*, 2: 136-146, 2017. <https://doi.org/10.1021/acsomega.6b00248>
147. Mollerup, JM, Breil, MP, Vogelpohl, C, Sadowski, G: Simultaneous correlation of hydrophobic interactions in HIC and protein solubility in aqueous salt solutions and mixed solvents. *Fluid Phase Equilib*, 301: 163-170, 2011. <https://doi.org/10.1016/j.fluid.2010.11.028>
148. Shuichi Yamamoto, KN, Ryuichi Matsuno: Ion-exchange chromatography of proteins. *CRC Press*, 1988. <https://doi.org/10.1201/b15751>
149. Steigmiller, R: *Characterization of the Elution Behavior of mAb02 and Scale-up of Membrane Chromatography*. Master Thesis, University of Applied Sciences Mannheim, Institute of Biochemistry, 2021.
150. Urbansky, ET, Schock, MR: Understanding, Deriving, and Computing Buffer Capacity. *Journal of Chemical Education*, 77: 1640, 2000. <https://doi.org/10.1021/ed077p1640>
151. Kern, N: *Monoclonal Antibody Variant Separation in Mixed-Mode Chromatography and Modelling of Basic Variant*. Master Thesis, University of Applied Sciences Mannheim, Institute of Biochemistry, 2018.

152. Braun, P: *Modeling of monoclonal antibody charge variant separation using mixed-mode chromatography*. Master Thesis, University of Applied Sciences Mannheim, Institute of Biochemistry, 2019.
153. Hedrich, J, Steigmiller, R, Simaev, V, Skudas, R, Schulte, M, Hafner, M, Frech, C: Mixed-mode membrane chromatography: mechanistic-modeling-based optimization and scale-up of antibody charge variant separation using a novel membrane adsorber. *Journal of Chemical Technology & Biotechnology*, n/a, 2025. <https://doi.org/https://doi.org/10.1002/jctb.70043>
154. Wulff, A: *Optimierung der Auftrennung eines monoklonalen Antikörpers mittels Mixed-Mode-Chromatographie- Membranprototypen und anschließende Modellierung*. Bachelor Thesis, University of Applied Sciences Mannheim, Institute of Biochemistry, 2020.
155. Simaev, V: *Scaling Up Membrane Chromatography for Efficient Separation of Monoclonal Antibody Charge Variants using Mechanistic Modeling*. Master Thesis, University of Applied Sciences Mannheim, Institute of Biochemistry, 2024.
156. Koehnlein, W, Holzgreve, A, Schwendner, K, Skudas, R, Schelter, F: Purification of hydrophobic complex antibody formats using a moderately hydrophobic mixed mode cation exchange resin. *Journal of Chromatography A*, 1687: 463696, 2023. <https://doi.org/10.1016/j.chroma.2022.463696>
157. Kallberg, K, Becker, K, Bülow, L: Application of a pH responsive multimodal hydrophobic interaction chromatography medium for the analysis of glycosylated proteins. *Journal of Chromatography A*, 1218: 678-683, 2011. <https://doi.org/10.1016/j.chroma.2010.11.080>
158. Arakawa, T, Ponce, S, Young, G: Isoform separation of proteins by mixed-mode chromatography. *Protein Expression and Purification*, 116: 144-151, 2015. <https://doi.org/10.1016/j.pep.2015.08.013>
159. Halan, V, Maity, S, Bhambure, R, Rathore, AS: Multimodal Chromatography for Purification of Biotherapeutics - A Review. *Curr Protein Pept Sci*, 20: 4-13, 2019. <https://doi.org/10.2174/1389203718666171020103559>

160. Kallberg, K, Johansson, H-O, Bulow, L: Multimodal chromatography: An efficient tool in downstream processing of proteins. *Biotechnology journal*, 7: 1485-1495, 2012. <https://doi.org/10.1002/biot.201200074>
161. Nfor, BK, Ripić, J, van der Padt, A, Jacobs, M, Ottens, M: Model-based high-throughput process development for chromatographic whey proteins separation. *Biotechnology journal*, 7: 1221-1232, 2012. <https://doi.org/10.1002/biot.201200191>
162. Melander, WR, El Rassi, Z, Horváth, C: Interplay of hydrophobic and electrostatic interactions in biopolymer chromatography. *Journal of Chromatography A*, 469: 3-27, 1989. [https://doi.org/10.1016/s0021-9673\(01\)96437-4](https://doi.org/10.1016/s0021-9673(01)96437-4)
163. Mollerup, JM: Applied thermodynamics: A new frontier for biotechnology. *Fluid Phase Equilib*, 241: 205-215, 2006. <https://doi.org/10.1016/j.fluid.2005.12.037>
164. Wang, J, Jenkins, EW, Robinson, JR, Wilson, A, Husson, SM: A new multimodal membrane adsorber for monoclonal antibody purifications. *Journal of Membrane Science*, 492: 137-146, 2015. <https://doi.org/10.1016/j.memsci.2015.05.013>
165. Huuk, TC, Hahn, T, Doninger, K, Griesbach, J, Hepbildikler, S, Hubbuch, J: Modeling of complex antibody elution behavior under high protein load densities in ion exchange chromatography using an asymmetric activity coefficient. *Biotechnology journal*, 12, 2017. <https://doi.org/10.1002/biot.201600336>
166. Altern, SH, Welsh, JP, Lyall, JY, Kocot, AJ, Burgess, S, Kumar, V, Williams, C, Lenhoff, AM, Cramer, SM: Isotherm model discrimination for multimodal chromatography using mechanistic models derived from high-throughput batch isotherm data. *Journal of Chromatography A*, 1693: 463878, 2023. <https://doi.org/10.1016/j.chroma.2023.463878>
167. Baumann, P, Baumgartner, K, Hubbuch, J: Influence of binding pH and protein solubility on the dynamic binding capacity in hydrophobic interaction chromatography. *Journal of Chromatography A*, 1396: 77-85, 2015. <https://doi.org/10.1016/j.chroma.2015.04.001>
168. Lee, SH, Ruckenstein, E: Adsorption of proteins onto polymeric surfaces of different hydrophilicities—a case study with bovine serum albumin. *Journal of*

- Colloid and Interface Science*, 125: 365-379, 1988.  
[https://doi.org/10.1016/0021-9797\(88\)90001-x](https://doi.org/10.1016/0021-9797(88)90001-x)
169. Coen, CJ, Blanch, HW, Prausnitz, JM: Salting out of aqueous proteins: Phase equilibria and intermolecular potentials. *AIChE Journal*, 41: 996-1004, 1995.  
<https://doi.org/10.1002/aic.690410430>
170. Arakawa, T, Timasheff, SN: Mechanism of protein salting in and salting out by divalent cation salts: balance between hydration and salt binding. *Biochemistry*, 23: 5912-5923, 1984. <https://doi.org/10.1021/bi00320a004>
171. Agena, SM, Bogle, IDL, Pessoa, FLP: An activity coefficient model for proteins. *Biotechnology and Bioengineering*, 55: 65-71, 1997.  
[https://doi.org/10.1002/\(sici\)1097-0290\(19970705\)55:1<65::aid-bit8>3.0.co;2-v](https://doi.org/10.1002/(sici)1097-0290(19970705)55:1<65::aid-bit8>3.0.co;2-v)
172. Kleinheins, J, Marcolli, C, Dutcher, CS, Shardt, N: A unified surface tension model for multi-component salt, organic, and surfactant solutions. *Physical Chemistry Chemical Physics*, 26: 17521-17538, 2024. <https://doi.org/10.1039/d4cp00678j>
173. Sjöberg, B, Mortensen, K: Structure and thermodynamics of nonideal solutions of colloidal particles: Investigation of salt-free solutions of human serum albumin by using small-angle neutron scattering and Monte Carlo simulation. *Biophysical Chemistry*, 65: 75-83, 1997. [https://doi.org/10.1016/s0301-4622\(96\)02251-x](https://doi.org/10.1016/s0301-4622(96)02251-x)
174. Wolfe, LS, Barringer, CP, Mostafa, SS, Shukla, AA: Multimodal chromatography: Characterization of protein binding and selectivity enhancement through mobile phase modulators. *Journal of Chromatography A*, 1340: 151-156, 2014.  
<https://doi.org/10.1016/j.chroma.2014.02.086>
175. Voitl, A, Muller-Spath, T, Morbidelli, M: Application of mixed mode resins for the purification of antibodies. *J Chromatogr A*, 1217: 5753-5760, 2010.  
<https://doi.org/10.1016/j.chroma.2010.06.047>
176. Sher, A, Niederer, SA, Mirams, GR, Kirpichnikova, A, Allen, R, Pathmanathan, P, Gavaghan, DJ, Van Der Graaf, PH, Noble, D: A Quantitative Systems Pharmacology Perspective on the Importance of Parameter Identifiability. *Bulletin of Mathematical Biology*, 84, 2022. <https://doi.org/10.1007/s11538-021-00982-5>

177. Ishihara, T, Yamamoto, S: Optimization of monoclonal antibody purification by ion-exchange chromatography. Application of simple methods with linear gradient elution experimental data. *J Chromatogr A*, 1069: 99-106, 2005.  
<https://doi.org/10.1016/j.chroma.2004.10.040>
178. Dimer, F, Petzold, M, Hubbuch, J: Effects of ionic strength and mobile phase pH on the binding orientation of lysozyme on different ion-exchange adsorbents. *Journal of Chromatography A*, 1194: 11-21, 2008.  
<https://doi.org/10.1016/j.chroma.2007.12.085>

## 7 CURRICULUM VITAE

### PERSONAL DATA

Name: Jan Anselm Hedrich  
Date of birth: 08.03.1991  
Place of birth: Heilbronn

### SCHOOL CAREER

09/07 – 06/10 **University Entrance Qualification** | Christiane-Herzog-Schule, Heilbronn, Germany

- Final Grade: 2.6 (satisfactory)

### ACADEMIC CAREER

03/19 – present **Doctoral Student** | Ruprecht-Karls-Universität Heidelberg, Germany

- Conducted doctoral studies focused on modelling and simulation of liquid chromatography
- Aiming at the degree Doctor scientiarum humanarum (Dr. sc. hum.)

03/16 – 02/18 **Master of Science** | Hochschule Mannheim – University of Applied Sciences, Germany

- Biotechnology – Bioprocess Development
- Final Grade: 1.4 (very good)

03/11 – 08/15 **Bachelor of Science** | Hochschule Mannheim – University of Applied Sciences, Germany

- Focus Biotechnology
- Final Grade: 2.0 (good)

## WORK EXPERIENCE

- 11/21 – present     **Lab Assistant** | Hochschule Mannheim – University of Applied Sciences, Germany
- Supervision of practical courses
  - Supervision of theses
  - Lab hardware maintenance (HPLC, IT)
- 03/18 – 06/24     **Research Assistant** | Steinbeis Transferzentrum an der Hochschule Mannheim
- Laboratory work and research
- 10/15 – 02/16     **Research Assistant** | Karlsruher Institute of Technology at the Institute for Microstructure Technology
- Research on electrically conductive polymers
- 03/14 – 08/14     **Apprenticeship** | Karlsruher Institute of Technology at the Institute for Microstructure Technology
- Biochemical surface functionalization of surface acoustic wave components
  - Coating of surface acoustic wave components with polymers

## PUBLICATIONS

**Hedrich, J.**, Steigmiller, R., Simaev, V., Skudas, R., Schulte, M., Hafner, M., Frech, C. (2025). *Mixed-mode membrane chromatography: mechanistic-modeling-based optimization and scale-up of antibody charge variant separation using a novel membrane adsorber*. J. Chem. Technol. Biotechnol.

**Hedrich, J.**, Braun, P., Skudas, R., Schulte, M., Frech, C. (2025). *Multimodal weak ion-exchange Chromatography: Modeling and Simulation of Antibody Charge Variant Separation Behavior (DRAFT)*

**Hedrich, J.**, Wittkopp, F., Frech, C. (2025). *Determining mass transfer coefficients from linear gradient experiments (DRAFT)*.

Wittkopp, F., **Hedrich, J.**, Peeck, L., Frech, C. (2017). *Calculation of linear pH gradient buffer compositions for elevated salt concentrations using a discontinuous buffer system (DRAFT)*

## SCIENTIFIC TALKS

**ACS Spring 2022** | San Diego, CA, USA

*PEG-modulated mixed-mode chromatography: A new tool for simultaneous fragment/aggregate separation in Fc-protein purification*

**ACS Fall 2021 Virtual Meeting & Expo** | Online Conference

*Mechanistic-modelling based optimization and scale-up of ion-exchange membrane chromatography*

**Usergroup Meeting 2019** | Burlington, MA, USA

*Modeling of Monoclonal Antibody Charge Variant Elution in Mixed-mode Cation Exchange Chromatography*

**PREP Symposium 2019** | Baltimore, MD, USA

*Modeling of monoclonal antibody charge variants elution in mixed-mode cation exchange chromatography*

## POSTER PRESENTATIONS

**ACS Spring 2019** | Orlando, FL, USA

*Prediction of mass transfer coefficients in linear pH and salt gradient elution*

**PREP Symposium 2019** | Baltimore, MD, USA

*Prediction of mass transfer coefficients in linear pH and salt gradient elution*

**PREP Symposium 2018** | Baltimore, MD, USA

*Predicting mass transfer coefficients in linear gradient elution in cation exchange chromatography*

## 8 ACKNOLEGEMENT

First and foremost, I would like to sincerely thank Prof. Dr. Mathias Hafner for his supervision and for the organizational support he provided throughout the development of my doctoral thesis.

I am deeply grateful to Prof. Dr. Christian Frech for granting me this extraordinary opportunity. His steady support, thoughtful advice, and fruitful discussions, which all contributed to my work have been invaluable and are very much appreciated.

My sincere thanks also go to Dr. Michael Schulte and Dr. Romas Skudas from Merck KGaA (Darmstadt), whose scientific discussions, expertise, and support I greatly valued and thoroughly enjoyed.

I would also like to warmly thank Christiane Koch and Elke Gebauer for their dedicated support in the laboratory, as well as Andrea Bentz for her exceptional organizational assistance.

I am equally grateful to my colleagues whom I had the pleasure of meeting during this time. In particular, I would like to mention Felix Wittkopp, Felix Seelinger, Gabriela Sanchez, and Carolin Stange, as well as my current colleagues Jonas Arnecke and Eric Volk. I would also like to thank all of my students whose theses I had the privilege to supervise. A special place is held by Nadine Kern, Pierre Braun, Alina Wulff, Manuel Diaz, Rita Steigmiller, Viktor Simaev, and many others whose dedication and enthusiasm have been a constant source of inspiration.

My heartfelt thanks go to my best friends Andreas and Patricia Müller, who always welcomed me with open arms. I am also deeply thankful to my nieces Leoni and Emeli, who never fail to put a smile on my face.

Above all, I owe my greatest gratitude to my parents Hans and Carola, as well as to my entire family, for their unwavering support, their trust, and for countless reasons beyond words. Without them, this work would not have been possible.

*“Happiness is to be found along the way, not at the end of the road...”*

- Robert Updegraff